Institut für Physik und Astronomie
H.E.S.S. Gruppe

Search for Gamma-Ray Emission from Bow Shocks of Runaway Stars

Dissertation

zur Erlangung des akademischen Grades
"doctor rerum naturalium"
(Dr. rer. nat.)
in der Wissenschaftsdisziplin "Astroteilchenphysik"

eingereicht an der
Mathematisch-Naturwissenschaftlichen Fakultät
der Universität Potsdam

von

Anneli Schulz

Potsdam, den 01. September 2014

Zusammenfassung

Das Rätsel des Ursprungs der kosmischen Strahlung wird seit über 100 Jahren angegangen und ist noch immer nicht gelöst. Kosmische Strahlung wird mit Energien die zehn Größenordnungen überspannen gemessen und erreicht Energien bis zu $\sim 10^{21}\,\mathrm{eV}$, weit höher als irgendein menschengemachter Beschleuniger erzeugen kann. Verschiedene Theorien über die astrophysikalischen Objekte und Prozesse, die solch hochenergetische Teilchen erzeugen können, wurden vorgeschlagen.

Eine prominente Erklärung für einen Prozess, der hochenergetische Teilchen erzeugt ist Schockbeschleunigung. Die Detektion von hochenergetischer Gammastrahlung von Supernovaüberresten, von denen einige schalenförmige Strukturen offenbarten, ist ein klarer Beweis für die Beschleunigung von Teilchen zu ultrarelativistischen Energien in den Schocks dieser Objekte. Die Umgebung von Supernovaüberresten ist komplex und das detaillierte Modellieren der Prozesse die zu hochenergetischer Gammastrahlung führen herausfordernd.

Die Untersuchung von Schockbeschleunigung an Bugwellen, die durch individuelle Sterne erzeugt werden, die sich mit Überschallgeschwindigkeit durch das interstellare Medium bewegen, bietet die einmalige Gelegenheit die physikalischen Eigenschaften von Schocks in einer weniger komplexen Umgebung zu bestimmen. Das komprimierte ("geschockte") Medium wird durch die Strahlung des Sterns und die durch den Schock angeregte Strahlung erhitzt und sendet infolgedessen thermische Infrarot-Strahlung aus. Nichtthermische Strahlung, die auf die Existenz von relativistischen Teilchen hinweist, wurde von zwei Bugwellen in Radio- und Röntgen-Wellenlängen gemessen. Theoretische Modelle der Strahlungsprozesse sagen hochenergetische und sehr hochenergetische Strahlung auf einem Niveau, welches mit aktuellen Instrumenten gemessen werden kann, voraus. Diese Arbeit präsentiert die Suche nach hochenergetischer Gammastrahung von Bugwellen von Schnellläufersternen in einem Energiebereich von $100\,\mathrm{MeV}$ bis $\sim 100\,\mathrm{TeV}$.

Diese Suche wird mit dem "large area telescope"(LAT) an Bord des *Fermi* Satelliten und den H.E.S.S. Teleskopen, die im Khomas Hochland in Namibia in Betrieb sind, durchgeführt. Der *Fermi* Satellit wurde 2008 gestartet und das *Fermi*-LAT durchmustert seitdem kontinuierlich den Himmel. Es detektiert Photonen im Energiebereich von $20\,\mathrm{MeV}$ bis über $300\,\mathrm{GeV}$ und hat eine noch nie dagewesene Sensitivität. Die Abdeckung des gesamten Himmels erlaubt es alle 28 Bugwellen von Schnellläufersternen, die im E-BOSS Katalog aufgelistet sind, zu untersuchen. Von keiner der Bugwellen der Schnellläufersterne konnte signifikante Strahlung nachgewiesen werden, obwohl diese von theoretischen Modellen, die die nichtthermische Emission von Bugwellen von Schnellläufersternen beschreiben, vorausgesagt wurde.

Das H.E.S.S. Experiment ist das sensitivste System von abbildenden Cherenkovteleskopen. Es kann Photonen mit Energien von einigen zehn GeV bis zu $\sim$100 TeV nachweisen. Sieben der Bugwellen von Schnellläufersternen wurden mit H.E.S.S. beobachtet und die Analyse der Daten wird in dieser Arbeit präsentiert. Auch die Analysen der sehr hochenergetischen Strahlung enthüllten keine signifikante Strahlung aus den Bugwellen der Schnellläufersterne.

Diese Arbeit stellt die erste systematische Suche nach Gammastrahlung aus Bugwellen von Schnellläufersternen vor. Zum ersten Mal wurden *Fermi*-LAT Daten speziell zur Suche nach Emission von diesen Objekten analysiert. Im TeV-Energiebereich wurden bisher noch keine Suchen nach Gammastrahlung von Schnellläufersternen publiziert, die hier vorgestellte Studie ist also die erste in diesem Energiebereich. Das Niveau des Gammastrahlungflusses von Schnellläufersternen wird über einen sechs Größenordnungen überspannenden Energiebereich eingeschränkt.

Die oberen Grenzen des Gammastrahlungsflusses aus Bugwellen von Schnellläufersternen schränken verschiedene Modelle ein. Für den besten Kandidaten, ζ Ophiuchi, liegen die berechneten oberen Grenzen im *Fermi*-LAT Energiebereich einen Faktor $\sim$5 unter den Vorhersagen. Dies fordert die Annahmen des Modells heraus und liefert wertvolle Bedingungen für weitere Modellierungsansätze.

Die präsentierten Analysen wurden mit den Softwarepakten, die von den *Fermi* und H.E.S.S. Kollaborationen zur Verfügung gestellt werden, durchgeführt. Die Entwicklung einer gemeinsamen Analyseumgebung namens *GammaLib/ctools* wird im Rahmen des CTA Konsortiums umgesetzt. Neue Implementierungen und Gegenproben zu den momentanen Analyseumgebungen werden im Anhang präsentiert.

Abstract

The mystery of the origin of cosmic rays has been tackled for more than hundred years and is still not solved. Cosmic rays are detected with energies spanning more than 10 orders of magnitude and reaching energies up to $\sim 10^{21}$ eV, far higher than any man-made accelerator can reach. Different theories on the astrophysical objects and processes creating such highly energetic particles have been proposed.

A very prominent explanation for a process producing highly energetic particles is shock acceleration. The observation of high-energy gamma rays from supernova remnants, some of them revealing a shell like structure, is clear evidence that particles are accelerated to ultrarelativistic energies in the shocks of these objects. The environments of supernova remnants are complex and challenge detailed modelling of the processes leading to high-energy gamma-ray emission.

The study of shock acceleration at bow shocks, created by the supersonic movement of individual stars through the interstellar medium, offers a unique possibility to determine the physical properties of shocks in a less complex environment. The shocked medium is heated by the stellar and the shock excited radiation, leading to thermal infrared emission. 28 bow shocks have been discovered through their infrared emission. Non-thermal radiation in radio and X-ray wavelengths has been detected from two bow shocks, pointing to the existence of relativistic particles in these systems. Theoretical models of the emission processes predict high-energy and very high-energy emission at a flux level in reach of current instruments. This work presents the search for gamma-ray emission from bow shocks of runaway stars in the energy regime from 100 MeV to ~ 100 TeV.

The search is performed with the large area telescope (LAT) on-board the *Fermi* satellite and the H.E.S.S. telescopes located in the Khomas Highland in Namibia. The *Fermi*-LAT was launched in 2008 and is continuously scanning the sky since then. It detects photons with energies from 20 MeV to over 300 GeV and has an unprecedented sensitivity. The all-sky coverage allows us to study all 28 bow shocks of runaway stars listed in the E-BOSS catalogue of infrared bow shocks. No significant emission was detected from any of the objects, although predicted by several theoretical models describing the non-thermal emission of bow shocks of runaway stars.

The H.E.S.S. experiment is the most sensitive system of imaging atmospheric Cherenkov telescopes. It detects photons from several tens of GeV to ~ 100 TeV. Seven of the bow shocks have been observed with H.E.S.S. and the data analysis is presented in this thesis. The analyses of the very-high energy data did not reveal significant emission from any of the sources either.

This work presents the first systematic search for gamma-ray emission from bow shocks of runaway stars. For the first time *Fermi*-LAT data was specifically analysed to reveal emission from bow shocks of runaway stars. In the TeV regime no searches for emission

from theses objects have been published so far, the study presented here is the first in this energy regime. The level of the gamma-ray emission from bow shocks of runaway stars is constrained by the calculated upper limits over six orders in magnitude in energy.

The upper limits calculated for the bow shocks of runaway stars in the course of this work, constrain several models. For the best candidate, ζ Ophiuchi, the upper limits in the *Fermi*-LAT energy range are lower than the predictions by a factor ~ 5. This challenges the assumptions made in this model and gives valuable input for further modelling approaches.

The analyses were performed with the software packages provided by the H.E.S.S. and *Fermi* collaborations. The development of a unified analysis framework for gamma-ray data, namely *GammaLib/ctools*, is rapidly progressing within the CTA consortium. Recent implementations and cross-checks with current software frameworks are presented in the Appendix.

Contents

1. Introduction

A view into the night sky, filled with thousands of stars, is fascinating for everybody; but for an astrophysicist the phenomena invisible to the eyes are even more astonishing. The discovery of a high-energy particle radiation coming from space, later named cosmic rays (CRs), by Victor Hess in 1912 was unexpected. The questions of the particle acceleration mechanism and astrophysical sources are still not unambiguously answered. Today we know from many experiments that the energy spectrum of cosmic rays, shown in Fig. 1.1(b), extends up to energies of at least 10^{21} eV. The energy spectrum follows a power law with an index of -2.7 from above a few GeV up until the so-called "knee" at $\sim 4 \cdot 10^{15}$ eV, then steepening with an index of -3.3 up to $\sim 5 \cdot 10^{18}$ eV, the so-called "ankle".

(a) Victor Hess during one of his balloon flights in 1911 or 1912. Image credit: VF Hess Society.
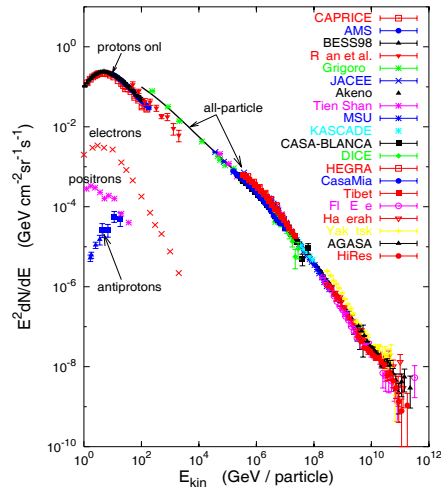
(b) Spectrum of cosmic rays as a function of energy. Figure from Hillas (2006).

Figure 1.1.: Victor Hess during one of his balloon flights and the cosmic ray spectrum.

Spectral breaks in the energy spectrum of cosmic rays are most commonly associated with changes in the composition and the sources. The spectral steepening at the knee is most commonly interpreted as the onset of the transition from galactic to extragalactic sources. In this theory the position of the knee corresponds to the maximum energy that protons from Galactic accelerators can reach. At energies around the ankle, the CRs then dominantly originate from extragalactic cosmic-ray accelerators.

The composition of CRs is dominated by protons and helium (99%), followed by heavier nuclei (1%). All components are charged and thus deflected by interstellar and intergalactic magnetic fields. To trace the origin of cosmic rays, neutral messengers like photons or neutrinos, produced as secondary products of the accelerated particles, are needed. The detection of neutrinos is challenging due to the small interaction cross-section, the one of high-energy gamma rays due to their absorption in the Earth's atmosphere.

The first neutrinos of astrophysical origin have recently been observed by IceCube (IceCube Collaboration 2013). Gamma rays have been detected from a variety of sources in the last decades. In 1967 high-energy gamma-ray emission from the galactic plane with a broad maximum towards the galactic centre was detected by the OSO-3 satellite (Kraushaar et al. 1972). Ground-based gamma-ray telescopes measure Cherenkov light produced by secondary particles which are created due to the interaction of the photon in the atmosphere. This technique was pioneered by the Whipple collaboration and lead to the discovery of very-high-energy gamma-ray emission from the Crab Nebula (Weekes et al. 1989). The discovery by IceCube, together with the detections of diverse sources in high- and very-high-energy gamma rays has proven, that these are the key techniques to tackle the mystery of the origin of cosmic rays.

Different mechanisms to produce CRs have been proposed. Enrico Fermi pioneered a theory of charged particles, which are repeatedly reflected by "wandering magnetic clouds" and thereby gain huge amounts of energy (Fermi 1949). Details of the so-called Fermi acceleration are outlined in Chapter 2. The astrophysical sources capable to produce fast enough clouds need to be extreme environments, good candidates are supernova explosions or regions close to black holes. Supernova remnants (SNRs) are the prime candidates for the sources of galactic cosmic rays, relativistic particles have been observed via the detection of non-thermal radiation of radio, X-rays and gamma rays.

At very-high energies (E> 100 GeV) H.E.S.S. is the leading instrument to detect gamma rays. With the observation of emission from the shell of the supernova remnant RX J1713-3946, (Aharonian et al. 2004), it demonstrated the acceleration of very-high-energy particles in shock waves to beyond 100 TeV. The morphology of the very-high-energy emission, shown in Fig. 1.2(a), is similar to the non-thermal X-ray emission shown in the same figure as black contours. Later observations revealed more shell-type SNRs, established them as a source class and as sources of cosmic rays, but did not unambiguously answer the question of the leptonic of hadronic nature of the accelerated particles. High-
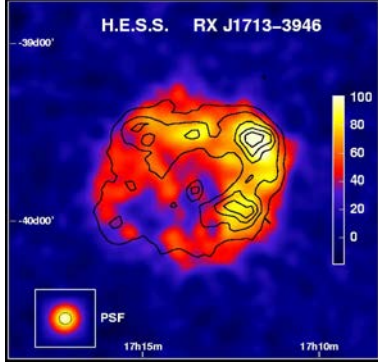
(a) Image of very-high-energy gamma-ray emission of the supernova remnant RX J1713-3946. The colour scale depicts excess counts and the PSF of the experiment is shown in the bottom left corner. The black contours depict radio emission detected by ATCA (Uchiyama et al. 2002). Image credit: H.E.S.S. collaboration.
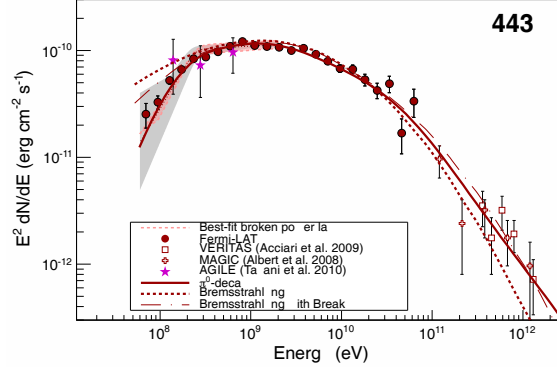
(b) Gamma-ray spectrum of the SNR IC 443, with the best fit broken power law as dashed line inside the colour-shaded area. The grey shaded area show the systematic error below 2 GeV. TeV spectral points from MAGIC and Veritas are also shown. Best fit models for pion decay and Bremsstrahlung are depicted with solid and dashed lines, respectively. Image from: Ackermann et al. (2013b).

Figure 1.2.: High-energy and very-high-energy observations of SNRs, namely RX J1713-3946 by H.E.S.S. and IC 443 by *Fermi*-LAT.

energy photons can be produced via inverse Compton up-scattering of relativistic electrons or as a product of hadronic interactions leading to neutral pions, which decay into photons. Further details on acceleration and emission processes are outlined in Section 2.4.

The first unequivocal evidence for the acceleration of protons in two SNRs was published recently by Ackermann et al. (2013b). The *Fermi*-LAT measurement of the spectrum of the SNR IC 443, reaching from 60 MeV to 100 GeV, is shown in Fig. 1.2(b). The photon spectrum from pion decay features a unique signature, the so-called pion-decay bump, since both photons retrieve an energy of $m_{\pi_0}c^2/2 = 67.5\,\text{MeV}$ in the rest frame of the photon. The best fit model for pion decay is depicted with a solid line, nicely matching the data. Models for leptonic emission are not able to describe the data properly, inverse Compton emission is not possible due to energetic constraints and the Bremsstrahlung model, depicted with a dashed line, does not fit the data. The Bremsstrahlung model fits the data, if an ad hoc break is introduced. This adds complexity to the model and is thus not preferred.

(a) The supernova remnant Puppis A seen as a red cloud in this WISE image.

(b) The bow shock of the runaway star HIP 22783, also called Alpha Camelopardalis.

Figure 1.3.: WISE images from two different systems where shock acceleration takes place, namely a supernova remnant and a bow shock of a runaway star. The colours represent different wavelengths: blue=3.4 microns; cyan=4.6 microns; green=12 microns; red=22 microns. Image credit: NASA/JPL-Caltech/WISE Team, `http://wise.ssl.berkeley.edu`.

Although the first steps towards solving the puzzle of the sources of cosmic rays are done, many details are not completely understood. The physical processes in shocks are complex and many aspects, like, e.g., the injection of particles, remain unclear. The surroundings of SNRs are non-trivial, the stellar wind of the progenitor star may have blown a bubble into the interstellar medium before exploding and ejecting parts of his mass. The simplifying assumption of spherical symmetry is not true for most cases. An example for an SNR, namely Puppis A, as seen in infrared is shown in Fig. 1.3(a). The expanding shock waves from the supernova heat the surrounding gas and dust, leading to the complicated shape of the cloud.

The study of shocks which accelerate particles in a less complex surrounding is therefore of great interest. The same type of shocks as present in SNRs is created by runaway stars. Runaway stars travel at large speeds through the interstellar medium. If they exhibit strong winds, they push the interstellar medium ahead of themselves, similar to a snowplough or a ship creating a bow wave. The interstellar medium is heated and glows in infrared; the same process as in an SNR. An example for a bow shock of a runaway star is shown in Fig. 1.3(b). The star responsible for the bow shock is indicated with an arrow, the bow shock develops ahead of the star since the stellar wind is pushing

outwards. Non-thermal emission from bow shocks of runaway stars has been detected in two cases, one in radio and one in X-rays. This is a clear evidence that relativistic particles are accelerated at these shocks.

The topic of this dissertation is the search for gamma-ray emission from bow shocks of runaway stars. In Chapter 2 runaway stars and their bow shocks are introduced. Surveys of stellar bow shocks are outlined and several highlights concerning the detection of non-thermal emission are presented. A theoretical model of the emission processes and particle populations is introduced together with its predicted spectral energy distributions. The observational techniques in high-energy and very-high-energy gamma-ray astronomy are explained together with the instruments *Fermi*-LAT and H.E.S.S. in Chapter 3. The gamma-ray analyses of the 28 bow shock candidates from the E-BOSS catalogue are presented in Chapter 4; neither the analysis of *Fermi*-LAT data, nor of H.E.S.S. data revealed significant emission from any of the candidates. Upper limits on the energy flux are calculated and compared to model predictions in Chapter 5. The thesis concludes with a brief summary and an outlook in Chapter 6.

2. Bow Shocks of Runaway Stars

This chapter summarises the current knowledge of bow shocks of runaway stars. Runaway stars are a subclass of stars, originally discovered more than 50 years ago. Their characteristics and possible origins are discussed in the first section. A fraction of these runaway stars features observable bow shocks, that are described in the second part. Surveys of stellar bow shocks, described in Sect. 2.3, lead to the development of theoretical models describing the geometrical shape of the bow shocks and the processes leading to thermal and non-thermal photon emission that are outlined in the subsequent section. The chapter concludes with studies of individual bow shocks of runaway stars in different energy ranges.

2.1. Runaway Stars

The term "runaway star" was invented by Blaauw (1956) for a group of high-velocity stars, when studying the characteristics of early-type stars, like the luminosity, age and kinematics, to deduce more information about the star forming process and the evolution of stars in the galaxy. The velocity distribution of the stars in the above mentioned publication revealed a group of "high-velocity young stars" ($v_* > 30\,\mathrm{km/s}$). Contrary to ordinary stars, nearly all high-velocity stars are single stars; i.e. are not bound in systems of two or more stars. The name "runaway" was chosen since the direction of the space velocity for most stars of this group points back to a known OB association, that is very likely the origin of the star. Nowadays all high-velocity stars are called runaways, independent on whether they can be traced back to a system or not. An example of the velocity distribution of young stars is shown in Fig. 2.1, the distribution can be explained by two different velocity groups, depicted with dashed lines. The fitted curves for the low and high velocity groups intersect at $\sim 30\,\mathrm{km/s}$, defining the border between the two groups. A similar distribution was published by Stone (1979), who studied the kinematics of O stars and came to the conclusion that a second population with high velocities is needed to describe the distribution. He concluded that most stars with velocities $v_* > 25\,\mathrm{km/s}$ are members of the high-velocity group.
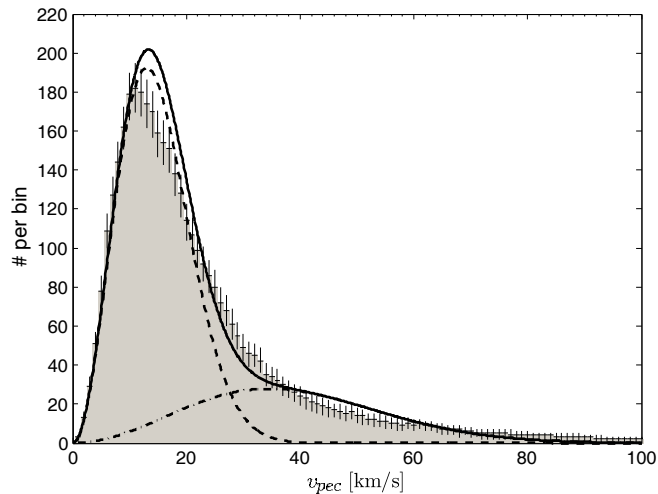
Figure 2.1.: Distribution of the space velocities for all stars in the sample of Tetzlaff et al. (2011). The fit to the low velocity group is depicted by the dashed curve, the one for the high velocity group by the dashed-dotted line. The sum of the two fits is shown as the full line. Figure from Tetzlaff et al. (2011).

A survey of runaway stars was performed by Blaauw (1961) and resulted in 19 candidates. In addition, they presented a theory of the origin of runaway stars, which was already proposed by Zwicky (1957): The runaway stars are assumed to emanate from binary systems, where one star loses most of its mass in a violent process, e.g., a supernova explosion type II, and the remaining star is released at a high spatial velocity due to the lack of gravitational attraction. An alternative is the dynamical ejection scenario proposed by Poveda et al. (1967). They argued that during the collapse of a small cluster dynamical interactions of the stars lead to runaway stars. They performed simulations of a small cluster with 5 or 6 stars and found the close encounters of the stars during the collapse lead to strong dynamical interactions, which resulted in high velocities. A high-velocity star with a large distance from the center of mass of the system will undisturbedly move outwards.

By retracing the trajectories of several nearby runaway stars, Hoogerwerf et al. (2000) conclude that both proposed mechanisms take place in nature: an example for the supernova scenario is ζ Ophiuchi; the orbits of AE Aurigae and μ Col together with ι Ori hint to the dynamical ejection scenario. The evidence in the first case is striking: ζ Ophiuchi is a single runaway star with two possible origins: the Upper Centaurus Lupus region, inferring a time where the star left its birth association of $\approx 3\,\mathrm{Myr}$, or the Upper Scorpius region pointing to a time of $\approx 1\,\mathrm{Myr}$. The pulsar PSR J1932+1059 passed the Upper Scorpius region about 1 Myr ago. The recalculated orbits of the sources are shown
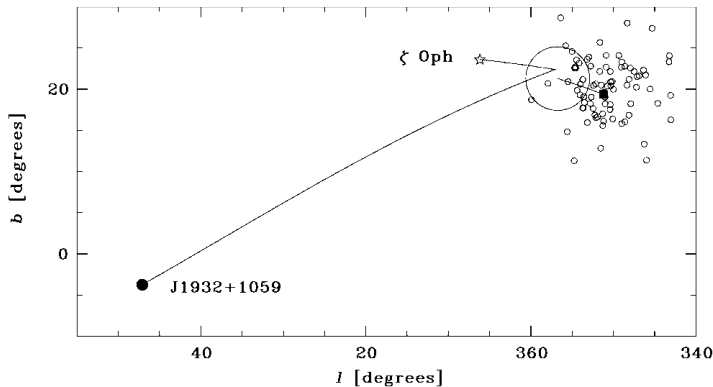
Figure 2.2.: Orbits of ζ Ophiuchi (position denoted with a star), PSR J1932+1059 (filled circle), and the center of the association (filled square). The large circle depicts the position of the association at the time of the supernova. The small circles denote positions of member stars of the Upper Scorpius. Figure from Hoogerwerf et al. (2000).

in Fig. 2.2. The observation of a HI shell around Upper Scorpius suggests a supernova explosion 1–2 Myr ago, possibly the precursor of PSR J1932+1059. These are exactly the ingredients needed for the binary-supernova scenario.

The best evidence for the dynamical ejection scenario would be two or more runaway stars originating in the same region. The runaways AE Aurigae and μ Col are both leaving the Orion association at 100 km/s, but in opposite directions. Gies & Bolton (1986) suggested the two to originate from the same event, a binary-binary encounter also including ι Ori. The backward calculations by Hoogerwerf et al. (2000) show that the stars were at the same position in the sky 2.5 ± 0.2 Myr ago, see Fig. 2.3. The authors investigated the orbits of 20 runaway stars and found two-thirds of them to originate in binary supernova events. Since the sample is rather small, it is not possible to deduce a solid statement. More sensitive observations have to be performed to get a clear answer.

The most recent study on runaway stars was performed by Tetzlaff et al. (2011) who study a sample of 7663 young stars from the Hipparcos catalogue, selected to be closer than 3 kpc. They chose stars younger than ∼50 Myr and find 2547 candidates for runaway stars. The fraction of runaway stars in the total sample is about one-quarter when assuming a contamination of normal stars by 20%.
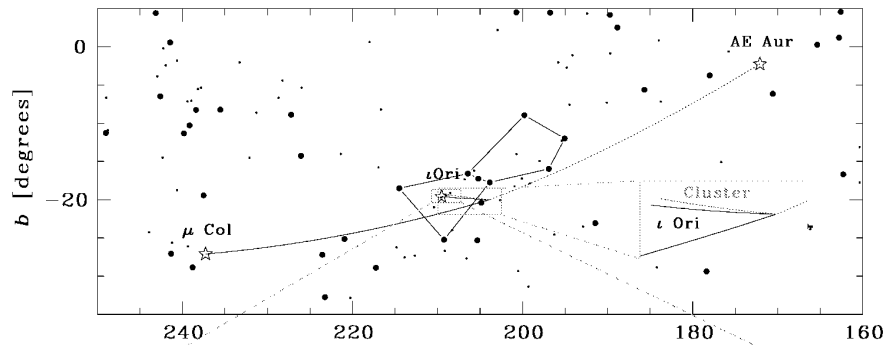
Figure 2.3.: Orbits of AE Aurigae (dotted line), μ Col (Solid line), and the binary ι Ori. The Orion constellation is shown for reference. The filled circles denote al stars from the Hipparcos Catalogue brighter than V=3.5 mag. Figure from Hoogerwerf et al. (2000).

2.2. Runaway Stars Creating Bow Shocks

Runaway stars move with high spatial velocities ($v_* \approx 30\,$km/s, in some cases well above $100\,$km/s) through the Interstellar Medium (ISM). If they move faster than the speed of sound ($v_{\mathrm{sound,ISM}} \approx 10\,$km/s) and have strong stellar winds, they can produce bow shocks. These arc-shaped structures develop in the direction of motion of the star, when inter-stellar material is swept up. The dust in the bow shock is heated by stellar and shock-excited radiation and produces thermal radiation in mid-to-far infrared. In an examination of all-sky images from IRAS (*Infrared Astronomical Satellite*), van Buren & McCray (1988) discovered, among other objects, stellar bow shocks. Their $60\,\mu$m IRAS image of the bow shock produced by ζ Ophiuchi is shown in Fig. 2.4(a) together with a recent picture of the same object as seen by Spitzer Fig. 2.4(b).

A prominent example for the interaction of a stellar wind with the interstellar medium is our Sun. It was assumed that there are three boundaries of the solar wind: the termination shock where the solar wind becomes subsonical, the heliopause as the boundary between the bubble created by the solar wind and the interstellar medium, and the bow shock created when the sun moves supersonically through the interstellar medium (Baranov et al. 1971).

In 2013 NASA announced[1] that Voyager 1 had crossed the heliopause on August 25, 2012. The Voyager 1 spacecraft was launched 1977 and is the first man-made object to reach the interstellar medium. Their data show a dramatic increase in density and the rate of solar wind ions dropped from $\approx 25\,$particles/second to $\approx 3\,$particles/second. It

---

[1]http://www.nasa.gov/mission_pages/voyager/voyager20130912.html
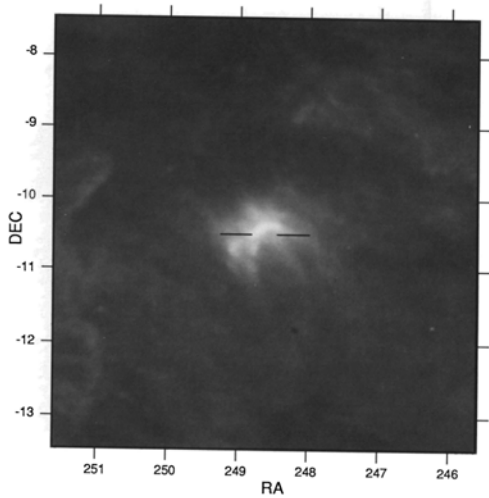
(a) ζ Ophiuchi in the $60\,\mu$m band of IRAS in the first publication by van Buren & McCray (1988).

(b) ζ Ophiuchi as seen by Spitzer, image credit: NASA/JPL-Caltech, Spitzer Space Telescope, source: http://photoshd.wordpress.com.

Figure 2.4.: ζ Ophiuchi as seen in infrared by IRAS (left-hand) and Spitzer (right-hand). The images are not to scale but nicely show the improvement concerning the resolution of the instruments.

was commonly expected that the sun creates a bow shock until McComas et al. (2012) showed, that no bow shock is observed. The velocity of the sun is smaller than previously assumed and the combination of the magnetic field and matter density do not allow the creation of a bow shock.

Other objects creating bow shocks are pulsars, colliding wind binaries, cataclysmic variables and cometary HII regions. A lot of work has been done on the modelling of these (see van Buren et al. 1995, and references therein). The modelling of stellar bow shocks is outlined in Section 2.4.

2.3. Surveys of Stellar Bow Shocks

The first survey of bow shocks of runaway stars was performed by van Buren et al. (1995) on IRAS data of 188 runaway stars. It resulted in 58 bow shock candidates; i.e. a fraction of 30%. A structure is identified as a bow shock if the associated star is a high velocity wind-blowing star, the structure is aligned with the star's proper motion vector, and the large-scale properties match the theoretical description of van Buren & McCray (1988). The third publication in this series is by Noriega-Crespo et al. (1997). They produced

high resolution IRAS (HiRes) images that allowed to identify 6 new bow shocks and discard 3 of the original sample. More than half of the sample remains unresolved at the resolution of IRAS/HiRes of 1′. A resolved extended bow shock structure is present for 20 objects.

In the following years several stellar bow shocks have been found in searches of specific regions, but the first systematic study was performed by Peri et al. (2012). The E-BOSS (Extensive stellar BOw Shock Survey) catalogue is based on a search for infrared emission around 283 early-type stars, selected to be closer than 3 kpc, in the newest infrared data releases. The catalogue comprises 28 bow shock candidates with derived bow shock parameters listed in Table 2.1; the corresponding infrared images are shown in Fig. 2.5.

To obtain the sample of 28 bow shock candidates, Peri et al. (2012) defined two groups to create the initial sample: Group 1 includes all bow shock candidates from Noriega-Crespo et al. (1997). The exclusion of two Wolf-Rayet stars (HD 50896 and HD 192163) leads to a sample size of 56. Group 2 is based on Tetzlaff et al. (2011), that comprises ≈ 2500 runaway stars. From this catalogue, stars with spectral types O to B2 are selected, leading to a sample of 244 stars. A subgroup of 17 stars is present in both groups.

The authors used data from the following instruments: infrared data from the Midcourse Space eXperiment (MSX) and the Wide-field Infrared Survey Explorer (WISE)[2]; Hα data from Virginia Tech. Spectral Survey (VTSS) and the Southern Hemispheric Hα Sky Survey Atlas (SHASSA) and low frequency radio data from the postage server for NRAO/VLA Sky Survey (NVSS); for references see: Peri et al. (2012).

MSX covers about 55% of the candidates and WISE about 70%, the detailed detections are listed in the E-BOSS catalogue. The analysis of WISE data confirms 12 of the bow shaped emission features from Noriega-Crespo et al. (1997), others are rejected since there is only emission from the star itself or an extended source at the star's position. From MSX data three bow shocks are confirmed: BD+43°3654, HIP 38430 and HIP 101186.

Brown & Bomans (2005) searched for Hα emission from bow shocks using data from the Virginia Tech Spectral Survey (VTSS) and Southern Hemispheric Hα Sky Survey Atlas (SHASSA). They compare different methods to find bow shocks and conclude with the detection of eight bow shocks based on a list of 37 candidates from van Buren et al. (1995). Peri et al. (2012) cannot confirm the detections, they note that the regions are complex in Hα and thus they rely on the infrared emission.

The search for radio data was motivated by the detection of non-thermal radio emission from BD+43°3654 by Benaglia et al. (2010), see following section, and resulted in three

---

[2]via `http://irsa.ipac.caltech.edu/` and `http://wise.ssl.berkeley.edu/`
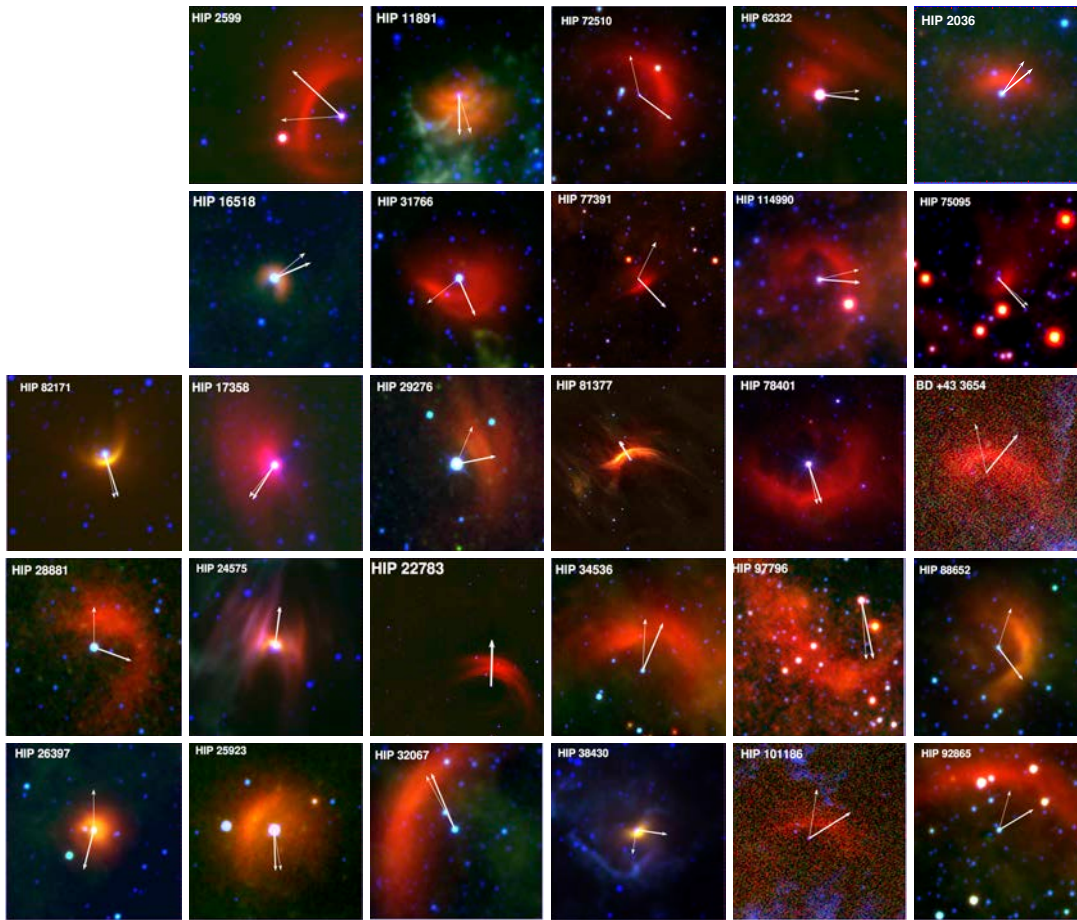
Figure 2.5.: Infrared images of the 28 bow shock candidates as published in Peri et al. (2012). WISE images with colour mapping: blue: 3.4 microns; green: 12.1 microns, red: 22.2 microns; for all except BD+43°3654 and HIP 101186. For the latter MSX images are shown, the color mapping is blue = 8.3 microns; green = 12.1 microns; red = 21.3 microns. The white vectors denote the proper motion of the star, the thicker one derived from Hipparcos data by van Leeuwen (2007), the thinner one after correction for the ISM motion due to Galactic rotation, both not to scale.

potential, coma-shaped radio sources at 1.4 GHz, namely HIP 11891, HIP 38430 and HIP 88652. Details on these radio sources are announced to be presented in a follow-up publication by the same authors.

Figure 2.6.: Spatial distribution of the bow shock candidates listed in the E-BOSS catalogue. Figure from: Peri et al. (2012).

(a) Distribution of the E-BOSS catalogue candidates in group 2 in age, binned in 5 Myr.

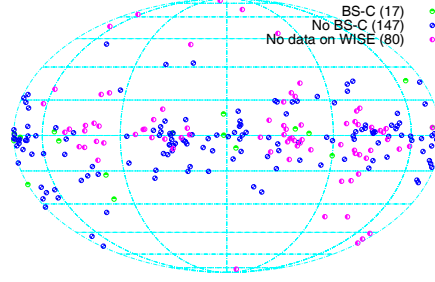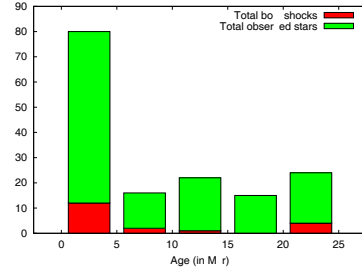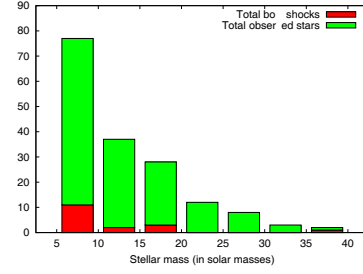(b) Distribution of the E-BOSS catalogue candidates in group 2 by mass, the data is split into bins of 5 M$_\odot$.

Figure 2.7.: Age and mass distribution of the bow shock candidates listed in the E-BOSS catalogue. Figures from: Peri et al. (2012).

For the 28 bow shock candidates they measure geometrical properties like the width and length of the bow shock and the stand-off radius R_0. From the latter they calculate the ambient density n_{ISM} at the position of the bow shock. The catalogue allows a first statistical study: Bow shocks are detected around 28 of the 283 OB stars; i.e. roughly 10%. Fig. 2.6 shows the spatial distribution of the stars in group 2 in galactic longitude and latitude, the bow shock candidates (depicted in green) seem to follow a similar distribution as the other stars. The distribution by spectral type also follows the distribution of the entire group. Fig. 2.7(a) shows that detections of bow shocks are more often associated to the youngest stars (might be expected), but also to the oldest observed stars. The same is true for the dependence on mass, shown in Fig. 2.7(b), where not only the suggested massive ones show bow shocks. In summary, no dependence of the detectability on either stellar mass, age, velocity or position is found. The sample is too small to conceive significant trends, but further studies are under way.

Star	l [°]	b [°]	d [pc]	v_* [km/s]	v_W [km/s]	$\dot{M}_* \cdot 10^6$ [$M_\odot$/yr]	Observational parameters (images) length [arcmin]	width [arcmin]	R_0 [arcmin]	n_{ISM} [cm^{-3}]
HIP 2036	120.9137	+09.0357	757±161[a]	16.0	1200.0	0.48	4.5	1.3	1	130
HIP 2599	120.8361	+00.1351	1457±300[a]	26.3	1105.0	0.12	9	1.3	3	0.4
HIP 11891	134.7692	+01.0144	(900)	49.5	2810.0	1.10	4	1	1	3
HIP 16518	156.3159	−16.7535	(650)	53.5	500.0	0.006	4	1	0.7	0.2
HIP 17358	150.2834	−05.7684	(150)	35.2	500.0	<0.001	3	1	1	600
HIP 22783	144.0656	+14.0424	1607±275[a]	52.4	1590.0	0.25	33	10	10	0.02
HIP 24575	172.0813	−02.2592	548±68[a]	152.0	1200.0	0.1	2	0.5	0.4	3
HIP 25923	210.4356	−20.9830	(900)	24.2	1000.0	0.06	4	1	1.5	1
HIP 26397	174.0618	+01.5808	(350)	22.4	750.0	0.014	3	1	1	2
HIP 28881	164.9727	+12.8935	1500[b]	17.7	2070.0	0.03	9	1.5	3	0.3
HIP 29276	263.3029	−27.6837	(400)	32.0	600.0	< 0.001	5	2	2	0.003
HIP 31766	210.0349	−02.1105	1414±28[a]	58.8	1590.0	1.07	5	2	2	0.03
HIP 32067	206.2096	+00.7982	2117±367[a]	38.8	2960.0	0.13	13	2.5	3	0.1
HIP 34536	224.1685	−00.7784	1293±206[a]	59.7	2456.0	0.19	12	3	4	0.01
HIP 38430	243.1553	+00.3630	(900)	30.9	2570.0	0.7	2	0.5	0.5	60
HIP 62322	302.4492	−05.2412	(150)	42.2	300.0	0.006	4	1.2	1	0.02
HIP 72510	318.7681	+02.7685	(350)	74.4	2545.0	0.27	4.5	0.8	1.5	0.2
HIP 75095	322.6802	+00.9060	(800)	28.9	1065.0	0.14	1.5	0.5	0.5	40
HIP 77391	330.4212	+04.5928	(800)	24.2	1990.0	0.25	4	1	1	30
HIP 78401	350.0969	+22.4904	224±24[a]	38.6	1100.0	0.14	25	2	6	2
HIP 81377	006.2812	+23.5877	222±22[a]	28.6	1500.0	0.02	22	2	5	1
HIP 82171	329.9790	−08.4736	845±120[a]	84.6	1345.0	0.09	2	0.5	0.7	1
HIP 88652	015.1187	+03.3349	(650)	31.1	1535.0	0.5	6	1	1.5	2
HIP 92865	041.7070	+03.3784	(350)	41.2	1755.0	0.04	11	1	3	0.003
HIP 97796	056.4824	−04.3314	2200[c]	110.4	1980.0	0.50	13	2.5	6	0.02
HIP 101186	082.3557	+02.9571	1486±402[a]	35.8	1735.0	0.23	19	2.5	4	0.1
BD+43°3654	082.4100	+02.3254	1450[d]	67.7	2325.0	6.5	12	3	3.5	0.2
HIP 114990	112.8862	+03.0998	1400[e]	135.7	1400.0	0.6	3.5	0.75	1.5	0.05

Table 2.1.: Bow shock candidates with measured parameters as listed in the E-BOSS catalogue. References for the distance values: (a) Megier et al. (2009), (b) Mason et al. (1998), (c) Schilbach and Roeser (2008), (d) Hanson (2003), (e) Thorburn et al. (2003); distances in brackets: derived from Hipparcos (van Leeuwen 2007) parallaxes.

The E-BOSS catalogue is based on the first release of data by the WISE team in April 2011, which covered 57% of the sky. The remaining data was published in March 2012. According to Benaglia et al. (2013) an updated version of the E-BOSS catalogue, taking the remaining WISE data into account, is ongoing. Further studies mentioned by these authors are: searches around stars that are not spectral types O or B, improved 3D modelling, dedicated observations of stellar bow shocks with hints of non-thermal emission, and the search for polarised radio emission from bow shocks of runaway stars.

2.4. Theoretical Description of Bow Shocks

Stellar bow shocks develop when a star with a strong wind moves supersonically through the interstellar medium. The surveys described before are based on the thermal emission of these objects at infrared wavelengths but there is theoretical motivation and experimental evidence for non-thermal emission as well. This section mainly follows the publication by del Valle & Romero (2012) and references therein. They present a model which includes thermal emission and a population of locally accelerated relativistic particles producing non-thermal emission. They apply their model to two example stars (type O9I and O4I) and ζ Ophiuchi as one of the best-studied objects of this kind. The flux prediction in high-energy and very-high energy gamma rays lies in reach for current and future experiments. This motivated the search for emission from bow shocks of runaway stars pursued in this work.

This section starts with a geometrical description of the bow shock system and its available power. The origin of the thermal emission is outlined in the second part. To produce non-thermal emission the particles have to be accelerated. The underlying principles of shock acceleration are thus presented in the third part, followed by the calculation of the non-thermal emission and the resulting particle distributions. The section concludes with the possible variability of emission from bow shocks of runaway stars.

2.4.1. Geometry of the Bow Shock System

A schematic view of the processes taking place at stellar bow shocks in the rest frame of the bow shock is shown in Fig. 2.8. The runaway star moves supersonically through the interstellar medium, material is compressed and a bow shock is formed.

In this system two shocks are created: a slow forward shock which develops in the same direction as the star's wind into the ISM with a speed $\approx v_*$ and a fast reverse shock, moving in the opposite direction at the much higher velocity of the star's wind. The bow shock is thus a confined layer of gas between two shock fronts with a contact discontinuity in between. The forward shock of these objects is usually rapidly cooling since the cooling
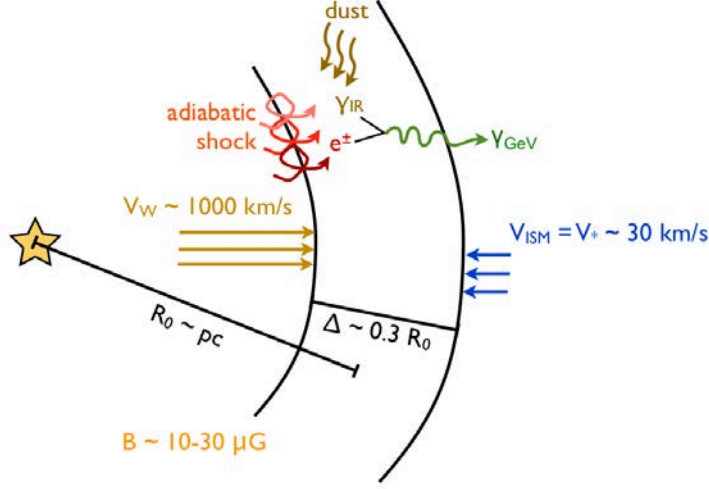
Figure 2.8.: Schematic view of a bow shock produced by a runaway star in the rest frame of the bow shock. Credit: S.Klepser.

length is much smaller than the stand-off radius (see definition below). This shock is thus called radiative shock. The reverse shock is much faster and therefore effectively adiabatic.

Stand-off Radius

One of the geometrical parameters which can be measured by analysing the infrared images is the so-called stand-off radius R_0. It is defined as distance between the star and the midpoint of the shock. In the E-BOSS catalogue the stand-off radii of the bow shocks are determined. By calculating the expected value for the stand-off radius it is possible to infer the density of the surrounding interstellar medium, ρ_{ISM}.

The ISM moves with the velocity of the star $v_{\text{ISM}} = v_* \approx 30\,\text{km/s}$, in the rest frame of the bow shock. This movement leads to a ram pressure $P_{\text{ISM}} = \rho_{\text{ISM}} \cdot v_{\text{ISM}}^2$ where ρ_{ISM} denotes the density of the ISM. The ram pressure of the stellar wind is $P_W = \rho_W \cdot v_W^2$ with the density ρ_W and the velocity of the wind v_W. The pressure of the stellar wind is decreasing with R^{-2} and balanced out by the constant ram pressure originating in the supersonic movement of the star through the ISM at the stand-off radius R_0, which can be calculated as:

$$
\begin{aligned}
P_{\mathrm{ISM}} &= P_{\mathrm{W}} && (2.1) \\
\rho_{\mathrm{ISM}} \cdot v_*^2 &= \rho_W \cdot v_W^2 \\
&= \frac{\dot{M}_*}{4\pi\,\mathrm{R}^2\,v_W} \cdot v_W^2 \\
\Rightarrow R_0 &= \sqrt{\frac{\dot{M}_* v_W}{4\pi\,\rho_{\mathrm{ISM}}\,v_*^2}} && (2.2)
\end{aligned}
$$

where $\dot{M}_*$ denotes the mass-loss rate of the star.

Peri et al. (2012) point out that the obtained values for ρ_{ISM} should be handled with caution since the width of the bow shock adds uncertainty to the R_0 determination and the mass-loss rate could be error prone.

Power distribution

The power available to accelerate particles in the shock can be estimated with the following assumptions: In the model by del Valle & Romero (2012), the width of the acceleration region Δ is estimated as $\Delta \sim \mathcal{M}^{-2} R_0$ with $\mathcal{M}$ being the Mach number of the shocked wind. The kinetic power of the stellar wind is

$$
L_T \sim \frac{1}{2}\dot{M}_* v_W^2. \qquad (2.3)
$$

The magnetic field is estimated with an assumption of the subequipartition factor, χ, between magnetic and kinetic energy density:

$$
\frac{B^2}{8\pi} = \frac{\chi L_T}{v_W 4\pi R_0^2}. \qquad (2.4)
$$

In the model by del Valle & Romero (2012) a subequipartition factor of $\chi = 0.1$ is assumed, the magnetic energy density is $10\,\%$ of the kinetic one. If the kinetic energy density is too small the material is not compressed, i.e. no shock is created and no particles are accelerated.

The next step is to calculate the power distribution in the acceleration region. The kinetic power of the stellar wind is assumed to be isotropically distributed, the available kinetic power in the acceleration region, $L_{T,acc.reg.}$, is thus only a part of this power. The geometrical factor is the volume fraction of a sphere with radius R_0 with respect to the volume of the acceleration region, $V_{acc.reg.}$.

$$L_{T,acc.reg.} = \frac{4/3\,\pi R_0^3}{V_{acc.reg.}} L_T \qquad (2.5)$$

Only a part of the kinetic energy power in the acceleration region, $L_{T,acc.reg.}$, is transformed into the acceleration of relativistic particles, L_{rel}:

$$L_{rel} = q_{rel} \cdot L_{T,acc.reg.} \qquad (2.6)$$

del Valle & Romero (2012) assume the fraction $q_{rel} = 10\,\%$. This relativistic power is divided into leptonic and hadronic particles. The model predictions in the paper are presented for two ratios, a, of hadronic to leptonic power ($L_{rel} = L_p + aL_e$): $a = 1$, meaning equal energy density in leptons and hadrons, and the hadron dominated case $a = 100$ as observed in galactic cosmic rays.

2.4.2. Thermal Radiation

The swept-up ISM gets heated up by the stellar radiation and the shock-excited radiation. Thermal radiation from the heated dust is detected at infrared wavelengths. The infrared luminosity of the star is only ~1% of the bolometric one, since the optical depth in dust is typically around 0.01 within 10 pc of a hot star (van Buren & McCray 1988). This radiation is not calculated in the model by del Valle & Romero (2012). Unlike the second component of thermal radiation, that is Bremsstrahlung (also called free-free radiation) produced by the shocked ISM. Bremsstrahlung is produced by the electrons being decelerated by the atoms in the medium, its peak is around 1 eV. In the model by del Valle & Romero (2012) this component is larger than the synchrotron radiation for the example 09I star, but negligible for the O4I star. Thermal processes are characterised by thermal equilibrium giving rise to a black-body spectrum.

2.4.3. Particle Acceleration at Shocks

The acceleration of particles is a necessary ingredient for non-thermal photon emission. The most common process for the acceleration of particles to high- and very-high energies is the so-called Fermi acceleration. This mechanism is explained before the radiative processes are introduced in the next part.

Fermi (1949) proposed a theory to explain the origin of cosmic radiation. He proposed the cosmic rays to be accelerated by collisions against "wandering magnetic clouds". The energy gain for a particle with energy E, $\Delta E/E$, after the collision with a cloud that has a much higher mass and moves with a velocity $v \ll c$ is calculated with the assumption

that the cloud is unaffected by the interaction and the momentum of the particle is inverted (from $\overrightarrow{p}$ to $-\overrightarrow{p}$).

$$\frac{\Delta E}{E} \sim \left(\frac{v}{c}\right)^2 \tag{2.7}$$

This process is called second order Fermi acceleration, since the energy gain is proportional to $(v/c)^2$. This mechanism predicts a power law energy spectrum for the accelerated particles, that can thus explain the shape of the cosmic ray spectrum.

Diffusive shock acceleration (e.g. Bell 1978; Drury 1983) is currently seen as the most probable model to describe the formation of high-energy particles. It is also called first order Fermi mechanism and explains the acceleration of particles with a successive bouncing of the particles across a shock. The energy gain per cycle is $\Delta E/E \sim v/c$, giving rise to the name Fermi I. Due to the escape probability of the particles it results in an energy spectrum with power law shape. An index of ~ 2 is expected for a strong shock, meaning that the ratio between upstream and downstream bulk velocities, the so-called compression factor, is ~ 4.

The time needed to accelerate a particle up to an energy E is the acceleration time τ_{acc}, calculated using the acceleration efficiency η:

$$\tau_{acc} = \eta \frac{E}{eBc} \qquad \text{with} \qquad \eta \sim 20 \frac{D}{r_g c}\left(\frac{c}{v_s}\right)^2 \sim \frac{20}{3}\left(\frac{c}{v_s}\right)^2, \tag{2.8}$$

where D is the diffusion coefficient that equals $r_g c/3$ in the Bohm limit, and $r_g = E/eB$ denotes the gyroradius of the particle. Faster shocks are more efficient in accelerating particles than slower shocks.

2.4.4. Non-Thermal Radiation of Shocks

Assuming that electrons and protons are accelerated in shocks, the contributions of the different processes which lead to a reduction of their energy can be calculated. For efficient acceleration, the time scales for acceleration have to be shorter than for the losses. The maximum energy the particle can achieve also depends on the relation of the time scales.

Radiative losses

Electrons mainly lose their energy due to synchrotron radiation, inverse Compton (IC) scattering and relativistic Bremsstrahlung. The dominant process for protons are inelastic proton-proton collisions with the shocked wind material.

Synchrotron radiation is emitted by charged relativistic particles that gyrate in a magnetic filed; in the non-relativistic case this radiation is called cyclotron radiation. The radiated power of the synchrotron emission is proportional to the inverse square of the particle's mass, thus mainly light particles, i.e. leptons, contribute to the synchrotron emission. The energy loss time scale for synchrotron radiation τ_{sync} is proportional to E^{-1}. The flux of the synchrotron radiation increases with increasing magnetic field. A detailed description of the processes that are taken into account and the corresponding time scales can be found in del Valle & Romero (2012) and references therein.

In Compton processes charged particles, mainly electrons and positrons, interact with photons. The Compton effect describes the case where the electron gains energy by scattering off a photon. If the process happens "the other way round", i.e. a highly energetic electron transfers energy to a photon, the process is called inverse Compton effect. The inverse Compton process is common in astrophysical sources. In principle this effect is also possible for nuclei and photons, but the cross section is much smaller. The cross section for the interaction of a photon and a lepton is given by the Klein-Nishima formula (Klein & Nishina 1929). The cross-section can be approximated by the Thomson cross-section for photon energies which are small compared to the electron rest mass ($E_\gamma \ll m_e c^2$). For large photon energies ($E_\gamma \gg m_e c^2$) the cross-section is suppressed compared to the Thomson cross-section. Details on the derivation of the inverse Compton spectrum for high-energy leptons are presented in Blumenthal & Gould (1970).

For the IC calculation in bow shocks two radiation fields are taken into account as target photon fields: the stellar photon field and the infrared radiation from the heated dust. Both are assumed to be black bodies at the corresponding temperatures. The stellar photon field is calculated at a distance R_0 from the star with the temperature T_*. The temperature of the dust is calculated following Draine & Lee (1984):

$$T_{\mathrm{IR}} = 27 \cdot a_{\mu\mathrm{m}}^{-1/6} \cdot L_{*,38}^{1/6} \cdot R_{0,\mathrm{pc}}^{-1/3} \, \mathrm{K} \tag{2.9}$$

Where $a_{\mu\mathrm{m}}$ denotes the dust grain radius in μm that is assumed to be 0.2. $L_{*,38}$ is the luminosity of the star in units of 10^{38} erg/s and $R_{0,\mathrm{pc}}$ the stand-off radius in parsec. The time-scales for this process are calculated following Blumenthal & Gould (1970), where a detailed description of the radiative losses of electrons is given.

Relativistic Bremsstrahlung is emitted when a charged particle is decelerated by the Coulomb field of protons and nuclei. The relevant time scale is inversely proportional to the density of the shocked wind and the logarithm of the electron energy.

Proton-proton collisions

The main process interaction process for protons are inelastic proton-proton collisions which, among others, lead to the production of charged and neutral pions. The neutral pions decay further into photons, the charged pions into leptons and neutrinos via the following channels:

$$
\begin{aligned}
\pi^0 &\rightarrow \gamma + \gamma, \\
\pi^\pm &\rightarrow \mu^\pm + \overset{(-)}{\nu_\mu}, \qquad\qquad \mu^\pm \rightarrow e^\pm + \overset{(-)}{\nu_e} + \overset{(-)}{\nu_\mu}.
\end{aligned}
\tag{2.10}
$$

The energy dependence of the time scale is rather small in the energy regimes considered in this work, see Fig. 2.9.

Maximum energy calculation

In addition to the radiative losses, the particles can escape the acceleration region through convection in the stellar wind. The corresponding time scale is $\tau_{conv} \sim \Delta/v_W$, with Δ being the size of the acceleration region.

The maximum possible energy for the particles is reached when cooling starts to dominate over acceleration, i.e. $\tau_{acc} = \tau_{cooling}$. For ζ Ophiuchi this maximum energy for protons and electrons is in the $\sim$TeV regime, see Fig. 2.9. The Hillas criterion states that the particles have to be magnetically confined in the acceleration region to get further accelerated, i.e. the gyroradius of the particles has to be smaller than the size of the acceleration region, denoted R. The maximum energy is limited by the size of the acceleration region R and the magnetic field:

$$
E_{max} < 300 \; \frac{R}{\text{cm}} \frac{B}{\text{G}} \; \text{eV}.
\tag{2.11}
$$

This criterion is fulfilled assuming the size of the acceleration region to be $R \sim \Delta$, as described before.

If the relativistic electrons and protons diffuse from the acceleration region into the shocked ISM, they create photons via relativistic Bremsstrahlung and p-p collisions. The model by del Valle & Romero (2012) shows that this contribution is negligible compared to the total IC emission.

The calculated cooling and acceleration times for electrons and protons for the example of ζ Ophiuchi are shown in Fig. 2.9.

(a) Acceleration and cooling times for electrons.   (b) Acceleration and cooling times for protons.
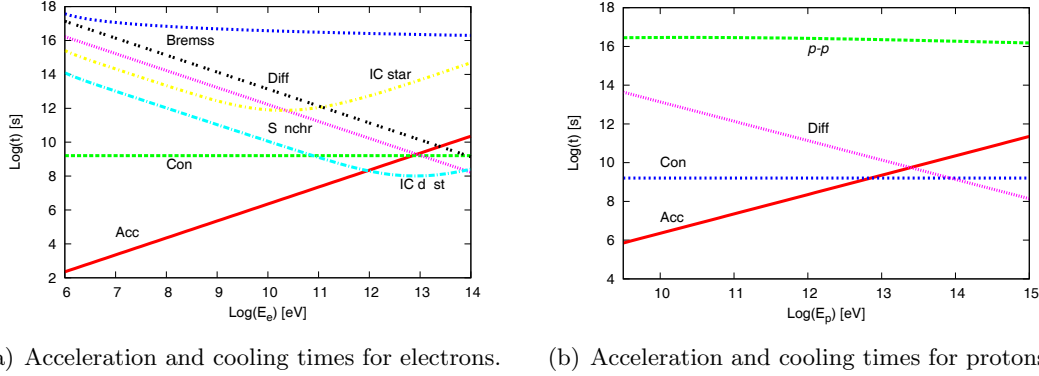
Figure 2.9.: Acceleration and cooling times for electrons and protons, assuming equipartition between electrons and protons, i.e. $a = 1$. Figure from: del Valle & Romero (2012).

Particle distributions

To calculate the particle distributions $N(E)$ in a steady state for electrons and protons the transport equation

$$\frac{\partial}{\partial E}\left[\left.\frac{dE}{dt}\right|_{loss} N(E)\right] + \frac{N(E)}{\tau_{esc}} = Q(E) \tag{2.12}$$

is solved, where $Q(E)$ is the injection function. Diffusive shock acceleration results in a power law shape: $Q(E) = Q_0 E^{-\alpha}$.

The above described processes give rise to the emission of photons. For the mathematical descriptions of the luminosity functions the reader is referred to del Valle & Romero (2012). The considered processes are synchrotron emission, inverse Compton scattering with the stellar photon field and the infrared photons, relativistic Bremsstrahlung and inelastic collisions of protons as described before. From these luminosities the spectral energy distribution (SED) is calculated. The result for the example of ζ Ophiuchi is shown in Fig. 2.17. The dominant process for the production of high- and very-high energy photons is the inverse Compton scattering on thermal emission from the dust. In first order approximation this depends on the temperature of the dust, the emission increases with increasing temperature. The temperature in turn depends on the luminosity of the star and the stand-off radius R_0 (see Eq. 2.9).

2.4.5. Bow Shocks of Runaway Stars as Variable Gamma-Ray Sources

Recently del Valle & Romero (2014) suggested bow shocks of runaway stars to be variable gamma ray sources. If runaway stars with bow shocks travel through molecular clouds, the characteristics of the bow shock change since they are determined by the ambient density. The variability time scale is a function of the density distribution of the molecular cloud and the stellar velocity. The emission depends, among other parameters as shown before, on the convection time scale τ_{conv}.

If the flow in the shock is turbulent due to inhomogeneities, the convection might take longer. Fig. 2.10 shows two variability lightcurves, extracted from del Valle & Romero (2014), for two different stars. For the O4I star two scenarios are depicted, case (a) with a normal convection time and case (b) with a ten times higher convection time. For the O9I star only the regular convection time is assumed. The integrated radio and X-ray luminosities increase with increasing density (n). The integrated gamma-ray luminosity increases for the O9I case and the O4I (b) case, but decreases in the O4I (a) case; see Fig. 2.10. The luminosity difference is up to a factor of ≈ 2. The calculated variability time scale is on the order of years, depending on the velocity of the star and the size of the density inhomogeneities of the surrounding medium.
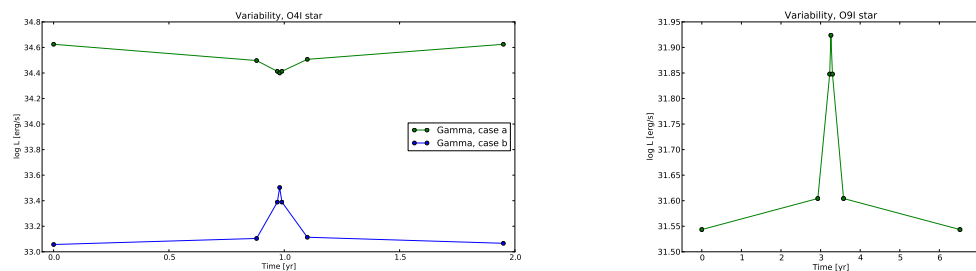
(a) Variability curve for an O4I star. Case a assumes a shorter convection time than case b, details see text.

(b) Variability curve for an O9I star.

Figure 2.10.: Variability curves for an O4I (O9I) star on the left-handed (right-handed) side, shown is the integrated luminosity between 0.03 and 100 GeV. Data points extracted from del Valle & Romero (2014).

The authors argue that the infrared and soft X-ray emission might be darkened by the molecular cloud, which does not effect radio and high-energy gamma-ray emission. Bow shocks of massive stars might be a new class of variable gamma-ray sources. The dedicated search for variable gamma-ray sources is beyond the scope of this work but might offer new possibilities and improve the sensitivity to detect high energy emission from these objects.

2.5. Studies of Individual Sources

After the discovery of bow shocks of runaway stars and the first catalogues based on infrared data, several individual sources were studied in more detail. This sections summarises the publications dealing with non-thermal emission.

2.5.1. BD+43°3654: Non-Thermal VLA Detection and Suzaku Upper Limits

BD+43°3654 is one of the bow shocks that was already mentioned in the first publication of van Buren & McCray (1988), although the central star was unidentified at that time. Comerón & Pasquali (2007) confirmed the bow shock detection by MSX observations and related it to the massive star BD+43°3654. A spatially coincident bow shock shape was also detected in the National Radio Astronomy Observatory - Very Large Array (NRAO-VLA) NVSS survey by Condon et al. (1998).

The first detection of non-thermal emission from the bow shock of a massive runaway star was published by Benaglia et al. (2010). Electrons, that gained energy through shock acceleration, cool via synchrotron radiation, and create a non-thermal radio source.
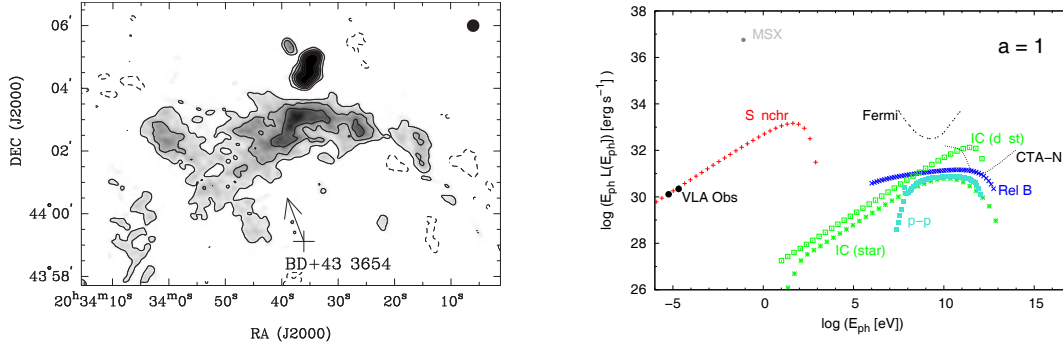
(a) Continuum emission at 1.42 GHz. BD+43°3654 is marked with a cross and the arrow depicts the velocity vector of the star. A synthesised beam of 12" · 12" is shown in the upper right corner.

(b) Spectral energy distribution for the case of equipartition between electrons and protons. The VLA and MSX data points are shown together with sensitivities for Fermi and CTA-North.

Figure 2.11.: Detection of non-thermal radio emission from BD+43°3654, together with the calculated spectral energy distribution. Figures taken from Benaglia et al. (2010).

The continuum radio emission of the source is shown together with the predicted SED in Figure 2.11. The SED shows that the emission predicted for the high- and very-high energy regime might be detectable by the *Fermi*-LAT and the future CTA-North.

Depending on the density of the surrounding medium and the energy-density distribution between electrons and protons either inverse Compton upscattering of dust photons on relativistic electrons or inelastic proton-proton collisions lead to high-energy gamma photons. To solve the puzzle of hadronic versus leptonic acceleration scenarios the observation of high- and very-high energy gamma radiation is crucial since it is the only energy range where both processes can produce photons, but be distinguished via the spectral shape of the energy spectrum.

This promising result was followed by a search for X-ray emission from the bow shock of BD+43°3654 by Terada et al. (2012). They find a possible enhancement of the X-ray count rate in a Suzaku observation conducted in April 2011 with 99 ks exposure, but the excess is not significant. The number of counts is compatible with the one in the background region within systematic errors. Their conclusions are an upper limit on the X-ray flux and a prediction for the SED, both shown in Figure 2.12.
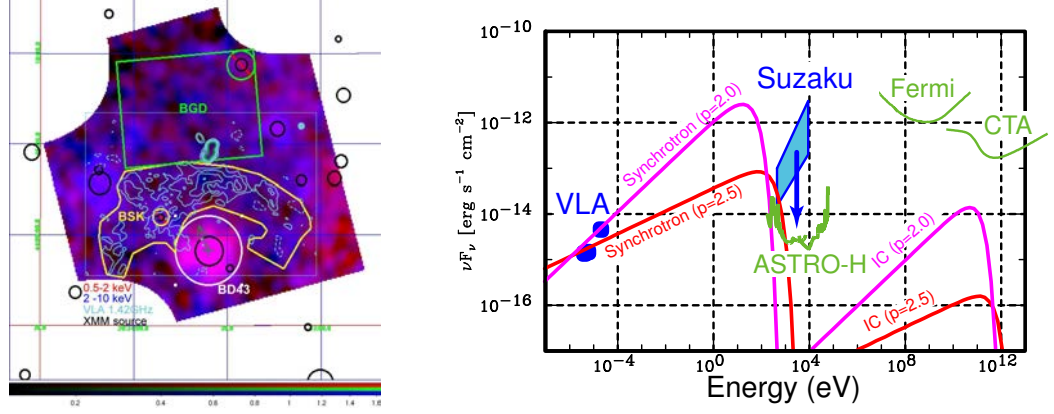
(a) Energy resolved X-ray image from Suzaku: Red and blue denote the 0.5– 2 keV and 2–10 keV images. XMM-Newton point sources are shown as black circles and the 1.42 GHz band from Benaglia et al. (2010) as cyan contour. The background (BGD), bow shock (BSK) and star (BD43) region are depicted in green, yellow and white, respectively.

(b) Spectral energy distribution for two cases, synchrotron emission with index 2 (2.5) in pink (red), both assume equipartition between electrons and protons. The VLA detection and the Suzaku upper limit are shown together with sensitivities for ASTRO-H, Fermi and CTA.

Figure 2.12.: X-ray image from BD+43°3654, together with the calculated spectral energy distribution. Figures taken from Terada et al. (2012).

The inverse Compton emission model in Fig. 2.12(b) accounts only for the cosmic X-ray background, which explains the much lower values compared to the calculation presented in Fig. 2.11(b) where the dust and the star photon fields are assumed as targets.

2.5.2. AE Aurigae (HIP 24575): XMM-Newton Detection

The first X-ray detection of a bow shock created by a runaway star was published by López-Santiago et al. (2012). The count images in two bands are shown in Fig. 2.13. They find an excess in the bow shocks regions (BS in the figure) and calculate the spectrum. The stellar spectrum, which was determined after subtracting the background from a nearby region, is clearly softer than the one from the BS region. Their conclusion is that a bow-shock shape is visible in the median photon energy map, shown in Fig.2.13(b) in green where the colour of each pixel represents the median energy of the detected counts, which is "somehow reminiscent"(López-Santiago et al. 2012) of the infrared bow shock.
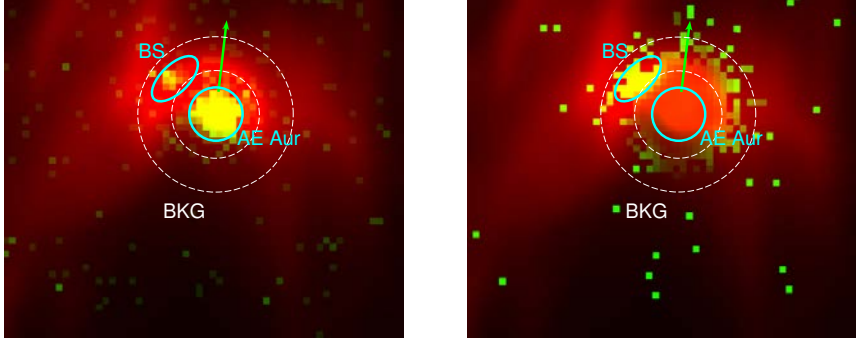
(a) EPIC pn count image in the 1–8 keV band in green and WISE 12.1 μm image in red.

(b) EPIC pn median photon energy map in the 0.3–8 keV band and WISE 12.1 μm image in red.

Figure 2.13.: AE Aurigae images from WISE 12.1 μm, shown in red, together with the EPIC pn count image in the 1–8 keV in the left panel and median photon energy map in the 0.3–8 keV band on the right-hand side. The bin size of the X-ray image is 4″. The regions of the star (AE Aur) and the bow shock (BS) are depicted in cyan, the background (BKG) region is denoted with the white dashed line. The proper motion vector of the star is superimposed in green. North is up and east is to the left. Figures from López-Santiago et al. (2012).

After subtracting the background from the region depicted in Fig. 2.13, the spectrum of the bow shock can be fitted with either a very hot thermal component or a non-thermal absorbed power law. The former seems unlikely since there is no counterpart in infrared or optical wavelengths and the temperature would have to be as high as kT= $2.4^{+2}_{-0.8}$ keV. The latter is supported by the very good spatial agreement between the infrared and hard X-ray emission as well as the spectral properties.

The authors therefore conclude that the X-ray emission originates from the bow shock of the runaway star and model the SED for AE Aurigae. The result, assuming equipartition
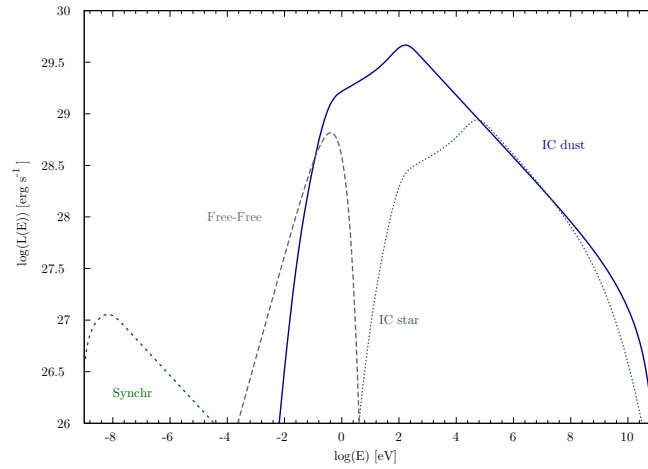
Figure 2.14.: Spectral energy distribution for AE Aur, assuming equipartition between electrons and protons. The different contributions are labelled accordingly, the sum is not shown. Figure taken from López-Santiago et al. (2012).

between electrons and protons, is shown in Fig. 2.14. Neither the detected spectrum nor the sum of the individual model components are shown in this plot of the paper.

2.5.3. HD 195592 (HIP 101186): Possible Gamma-Ray Association

In 2012 del Valle et al. (2012) suggested HD 195592 (HIP 101186) to be the first detection of a gamma-ray emitting bow shock of runaway stars. The position of the source 2FGL J2030.7+4417, published in the Second Fermi-LAT catalog (Nolan et al. 2012, hereafter 2FGL) is compatible with the one of the bow shock, as is shown in Fig. 2.15. The white circle depicts the 95% uncertainty on the position of the 2FGL source.

In the 2FGL (Nolan et al. 2012) the similarity of its spectral shape to known gamma-ray pulsars is noted and followed by a word of caution to not overinterpret the association to the star. 2FGL J2030.7+4417 was identified as a gamma-ray pulsar by Pletsch et al. (2012) in a blind search method, the phasogram is shown in Fig. 2.16. This result was confirmed by the Second *Fermi* Large Area Telescope Catalogue of Gamma-Ray Pulsars (Abdo et al. 2013), hereafter 2PC. In the latter, the pulsar is listed among the sources with no significant off-pulse emission. This is a clear indicator that the gamma-ray photons predominantly originate in the pulsar and not the bow shock. The first detection of gamma-ray emission from a bow shock of a runaway star is thus still pending.
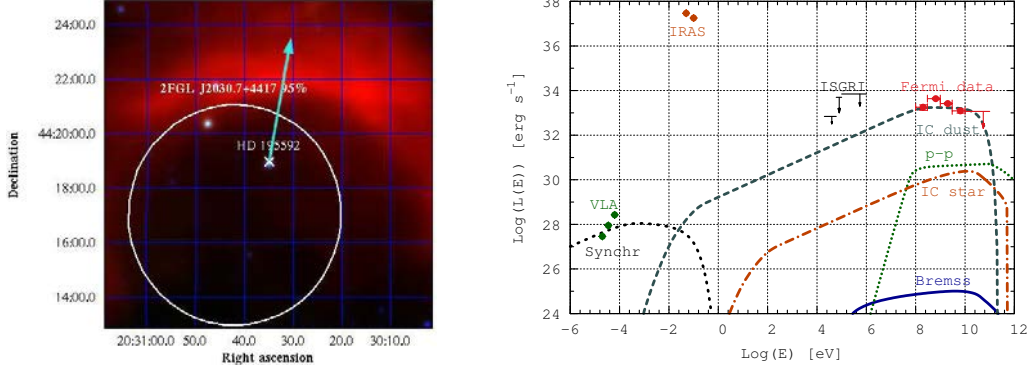
(a) WISE RGB image in three energy bands (4.6, 12 and 22 μm), the position of the star is marked with a white cross, the cyan arrow depicts the velocity. The white circle denotes the 95% contour of the position of 2FGL J2030.7+4417.

(b) SED computed for the bow shock of HIP101186, together with the *Fermi*-LAT data points from 2FGL J2030.7+4415, the thermal radio and IRAS data and INTEGRAL upper limits.

Figure 2.15.: WISE image and computed SED for the bow shock of HIP101186. Figures from del Valle et al. (2012).
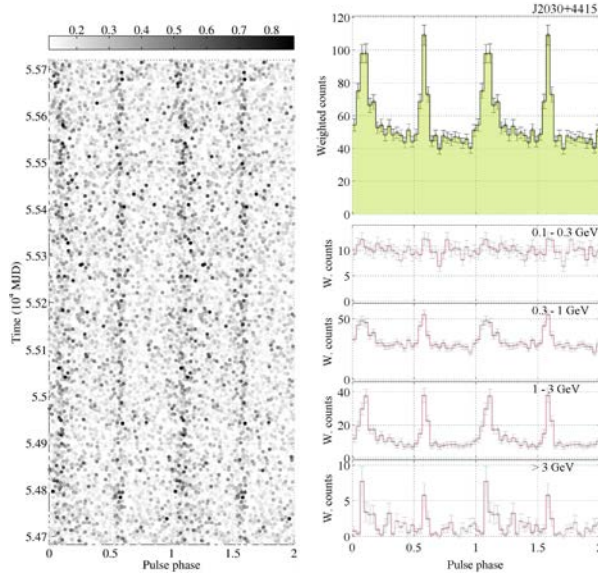
Figure 2.16.: Phase-time diagram and pulse profile for PSR J2030+4415. Figure taken from Pletsch et al. (2012).

2.5.4. ζ Ophiuchi (HIP 81377)

The best candidate for high-energy emission, as pointed out by del Valle & Romero (2012), is ζ Ophiuchi. This star is relatively close (222 pc) and the WISE and Spitzer images shows a clear bow shock structure. The model by del Valle & Romero (2012) describes the geometrical shape as well as the spectrum of the bow shock. The predicted SED is shown in Fig. 2.17 together with the thermal data points measured by IRAS, theoretical upper limits from XMM-Newton, and a VLA upper limit from the NVSS survey. The sensitivities of current and future gamma-ray experiments are indicated in red and black, showing that the prediction for this source is in reach for current instruments.
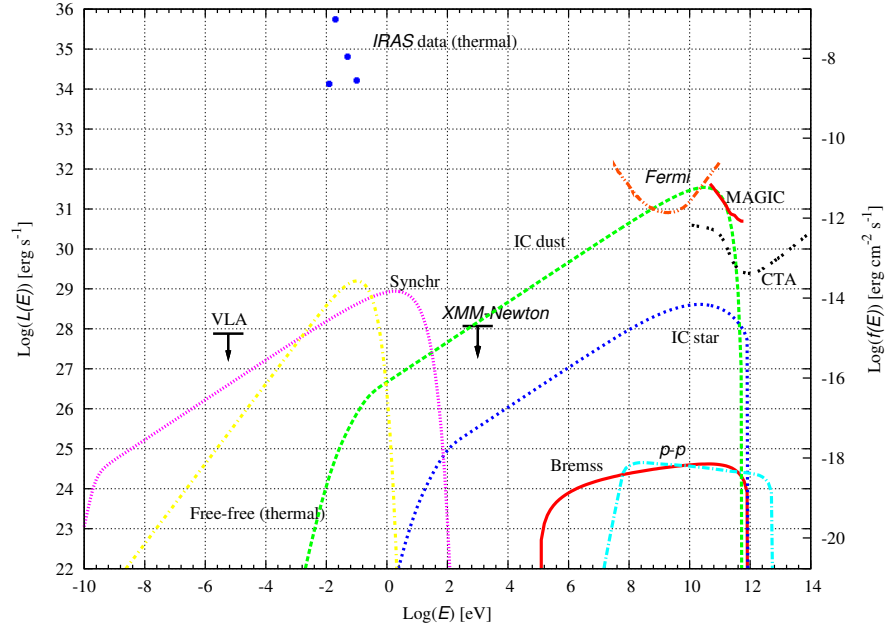
Figure 2.17.: Predicted SED for ζ Ophiuchi, computed assuming a distance of 222 pc. Together with data points from IRAS and upper limits from VLA and XMM-Newton. Also shown are the sensitivities for *Fermi*, MAGIC, and CTA. Figure from: del Valle & Romero (2012).

The key energy range to study acceleration of particles in bow shocks of runaway stars is the high- and very-high energy regime. The experimental methods used to detect photons in the two energy ranges are described in the following chapter.

3. Experimental Techniques in Gamma-Ray Astronomy

Astronomy is nowadays performed all across the electromagnetic spectrum. The energy spectrum of the photons spans over amazing 18 decades in energy; from radio waves with energies starting in the μeV range up to gamma rays with energies reaching beyond TeV. The methodology for the different wavelengths depends on the opacity of the Earth's atmosphere, as illustrated in Fig. 3.1. In the optical and radio range the atmosphere is transparent, allowing for ground-based observations. The Earth's atmosphere is opaque to gamma rays, which leads to two ways of detecting this kind of radiation: to measure above the atmosphere by putting a detector on a satellite or a balloon into space or to collect secondary products of the interaction of the particle in the atmosphere from which it is possible to determine the primary particle's properties.
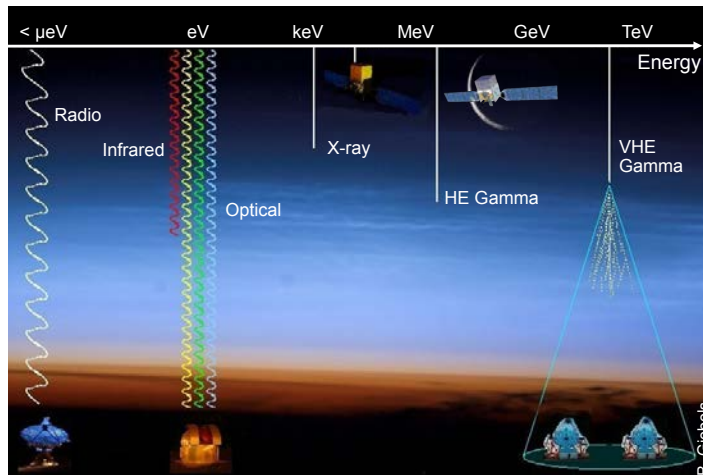
Figure 3.1.: The Earth's transmission spectrum as a function of energy, for some energies exemplary experiments are shown. Image credit: Berrie Giebels/CNRS/France.

In the course of the study presented here, the energy range from MeV to TeV was investigated. This energy regime is divided into two parts: high-energy (HE: 100 MeV to ~100 GeV) and very-high-energy (VHE: ~100 GeV to 100 TeV) gamma-ray astronomy.

In this chapter the two techniques in this field, pair conversion detectors and imaging atmospheric Cherenkov telescopes (IACTs), are introduced and the corresponding analyses are presented. The chapter concludes with a comparison of the performance of the two approaches.

3.1. High-Energy Regime

The methods to detect photons depend on the interaction mechanism in the corresponding energy range. Photons with energies in the MeV regime cannot be reflected but interact via the photoelectric effect, the Compton effect and pair creation. The mass attenuation coefficient for photons in air as a function of energy is shown in Fig. 3.2(a). Fig. 3.2(b) shows the dependence of the cross section on energy and the atomic number of the absorber material (Z). The green lines depicts the points where the probability for Compton scattering (σ) equals either the photoelectric one (τ) or the pair production one (κ). Pair creation is the dominant mechanism of interaction above 10 MeV and thus the key element in the detection of highly energetic photons.

In the following an introduction to the technique of direct photon detection at HE is given, followed by a description of the *Fermi*-LAT instrument and the data analysis.

3.1.1. The Technique: Pair-Conversion Detectors

The goal of any gamma-ray instrument is to determine the energy, direction and arrival time of photons, while ensuring that the particles are indeed photons. A pair-conversion detector achieves this, as the name suggests, by converting gamma rays into electron-positron pairs. The schematic setup of such a detector is shown in Fig. 3.3(a).

Conversion foils are made of a dense material, e.g., tungsten, to enhance the probability that the gamma ray converts into an electron-positron pair. The tracks of both particles are recorded by particle tracking detectors. The direction of the incoming photon is obtained via the reconstruction of the tracks. The photon's energy is calculated from the energy deposits of the electron and the positron in the calorimeter at the bottom of the detector. The calorimeters absorb the entire energy of the particles. The pattern created by incoming protons and nuclei in the calorimeter are different than for gamma-ray induced electrons and positrons, which also helps to reject such background events. The anticoincidence detector acts as a veto for background particles, in this case mainly
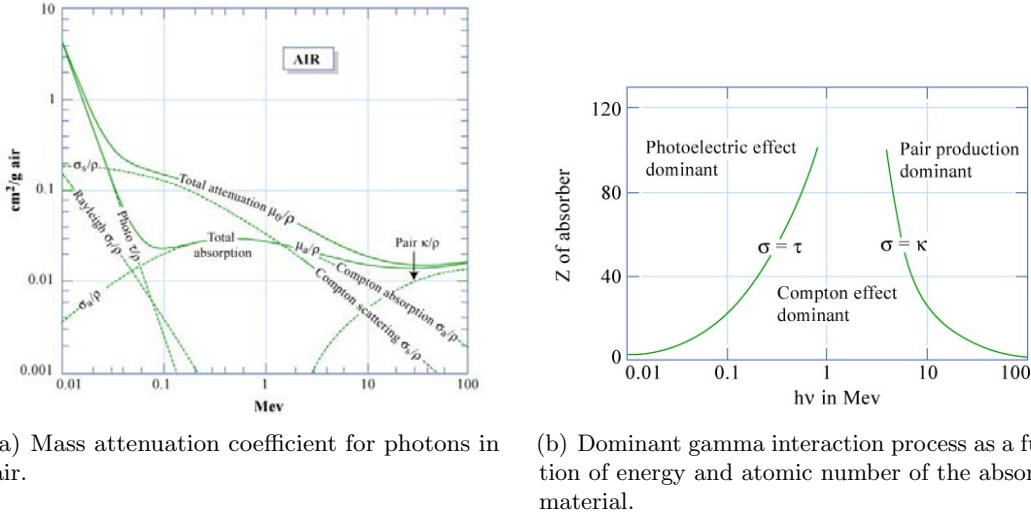
(a) Mass attenuation coefficient for photons in air.

(b) Dominant gamma interaction process as a function of energy and atomic number of the absorber material.

Figure 3.2.: Mass attenuation coefficient for photons in air and dominant gamma interaction as a function of energy and atomic number of the absorber material. Figure credit: MIT OpenCourseWare[1].

charged cosmic rays, which also create signals in the tracking detectors and the calorimeter. An incident photon does not leave a signal in the anticoincidence detector, in contrast to a charged cosmic ray particle. The path information of both particles is used to discriminate photons against the background of cosmic rays.

Fig. 3.3(b) shows the detector entries for a gamma-ray candidate event: the tracks of the electron and the positron are visible in the tracker layers and the entries in the calorimeter show the energy deposit.

3.1.2. The Instrument: Fermi-LAT

The *Fermi* Large Area Telescope (LAT) is a pair conversion telescope on board the *Fermi Gamma-ray Space Telescope*, hereafter *Fermi*. It is sensitive to gamma-rays from 20 MeV to over 300 GeV. Details of the instrument are described in Atwood et al. (2009), while the in-orbit performance of the telescope is described in Ackermann et al. (2012). The second instrument on board is the gamma-ray burst monitor (GBM), designed to observe gamma ray bursts in the energy range from 8 keV to 40 MeV. Details about the GBM are outlined in Meegan et al. (2009). *Fermi* was launched June 11, 2008 on a Delta II rocket from Cape Canaveral and is in an orbit of ∼565 km altitude since then.

---

[1]`https://www.flickr.com/photos/mitopencourseware/3775266331`
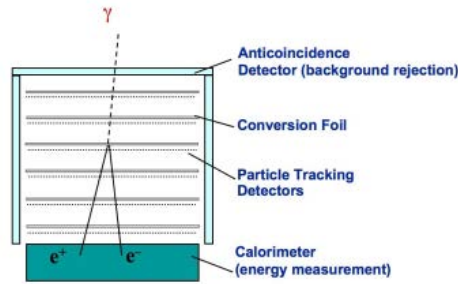
(a) Schematic of a pair-conversion detector including the tracker, calorimeter and the anticoincidence detector.
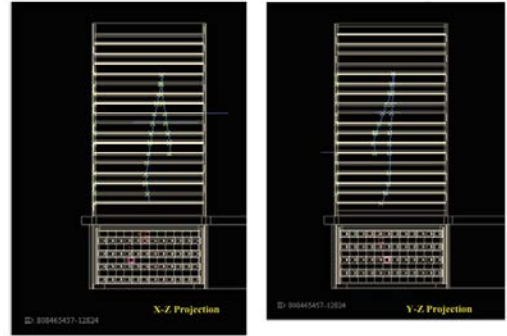
(b) Candidate gamma-ray event in a pair-conversion detector, shown in two projections. In the upper part the tracks can be identified, in the lower part the energy deposit in the calorimeter is shown in red.

Figure 3.3.: Schematic of a pair conversion telescope together with a gamma-ray candidate measured before launch. Image credit: NASA.

The basic detector components of the *Fermi*-LAT are the same as described in the previous section. The instrument is divided in 16 towers, each containing a tracker and a calorimeter. The tracker comprises 18 silicon strip tracking planes interleaved with tungsten foil as converter. The crucial length scale for this process is the so-called radiation length X_0. The radiation length is equal to 7/9 of the mean free path for pair creation of a high-energy photon. It is at the same time equal to the distance a high-energy electron travels before it loses all but $1/e$ of its energy due to Bremsstrahlung. The upper 12 trays pf the *Fermi*-LAT have tungsten layers with a thickness of 3 % of a radiation length, also referred to as the front section. The following 4 layers, the so-called back section, have a thickness of 18 % of a radiation length. The last two layers have no converter layers, since the tracker trigger needs signals from at least 3 consecutive layers.

The calorimeter of the *Fermi*-LAT is made of 8 layers, each layer featuring 12 crystals of cesium iodide, adding up to 8.6 radiation lengths. The layers allow longitudinal and transversal tracing of the energy deposit. The anticoincidence detector consists of 89 plastic scintillator tiles covering the top and the sides of the detector. The data acquisition combines the data from the three detectors and performs a first level trigger to distinguish between gamma rays and background events, deciding which events get sent to the science centre on Earth.

The LAT instrument was built by several institutes in the US, with contributions from France, Italy, Japan, and Sweden.
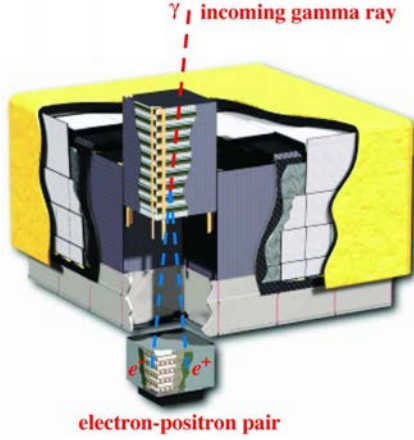
(a) *Fermi*-LAT in a schematic view. Its dimensions are $1.8 \times 1.8 \times 0.72\,\mathrm{m}^3$ and the weight is $2789\,\mathrm{kg}$.
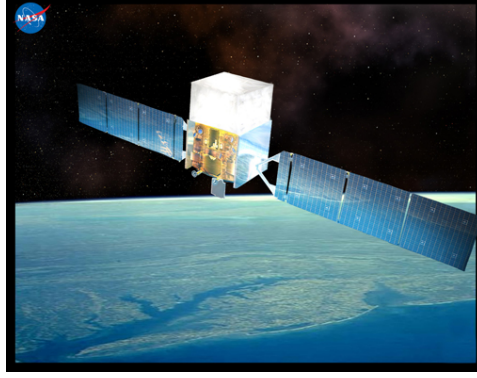
(b) Artist's impression of *Fermi* in the sky, the long arms are solar panels.

Figure 3.4.: An schematic view of the *Fermi*-LAT together with an image of it. Image credit: NASA.

Response functions

Each instrument has a certain probability to detect an incoming photon with certain properties. This probability depends on the detector and the observation conditions. The instrument response functions (IRFs) translate the number of detected events into an incoming photon flux and are thus essential to perform a scientific analysis of the data. It is assumed that the IRFs of the *Fermi*-LAT can be factorised in three parts that are used in an likelihood analysis following Mattox et al. (1996). These parts are: the effective area (A_{eff}), the point spread function (PSF), and the energy dispersion (D). All of them depend on the applied event selection and are thus calculated for the different event classes separately. The effective area is the product of the geometrical area, the conversion probability, the detector efficiency and the reconstruction efficiency, it therefore depends on the energy E of the photon and its direction in the LAT frame $\hat{v}$: $A_{\mathrm{eff}}(E, \hat{v})$. The PSF, as shown in Fig. 3.5(a), describes the probability density to reconstruct an event with direction $\hat{v}'$ for an event with energy E and direction $\hat{v}$: $PSF(\hat{v}'; \mathrm{E}, \hat{v})$. The energy dispersion, see Fig. 3.5(b), represents the probability density to measure an event with energy E' for an gamma ray with energy E and direction $\hat{v}$: $D(E'; E, \hat{v})$.

The IRFs depend on the direction of the photon in the LAT frame, as shown in Fig. 3.6 on the right-hand side for the effective area. The exposure is consequently calculated depending on the direction $\hat{v}$. The incidence angle Θ of an event is defined with respect to the z axis of the LAT, the line normal to the top surface of the LAT.

For a given source of gamma rays the IRFs can be used to calculate the flux of observed gamma rays by integrating the distribution of photons at the source convolved with the IRFs over the time and region of interest, the solid angle in the LAT and the energy range.

All performance plots are shown for the front and back sections separately since their architecture is different. During the analysis it is possible to select events converting in the front, the back, or both, depending on the goal of the analysis. The front section has a better PSF, as shown in Fig. 3.5(a). The PSF of the $Fermi$-LAT decreases strongly with increasing energy, the reason being the decreasing probability for multiple scattering. The limiting factor at high energies is the spatial resolution of the silicon tracker. The variation of the PSF is from $6°$ at $100\,$MeV to $0.25°$ at $10\,$GeV.

The energy resolution, shown in Fig. 3.5(b) is of the order of $\sim 10\,\%$. For lower energies it is better for the front section, for higher energies the back section is superior. The two plots in Fig. 3.5 also show the reason for the two components, on the one hand to achieve a good PSF and on the other hand to have a good energy resolution. The peak effective area of the $Fermi$-LAT is $\sim 8000\,$cm^2.
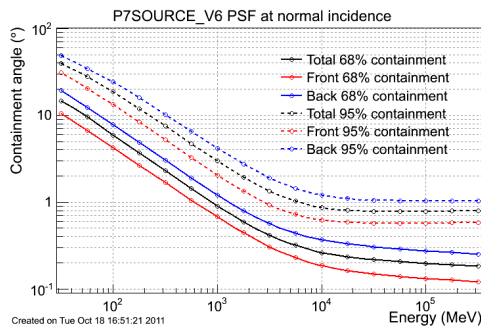
(a) The point spread function of the front and back sections of the $Fermi$-LAT at normal incidence, depending on energy.
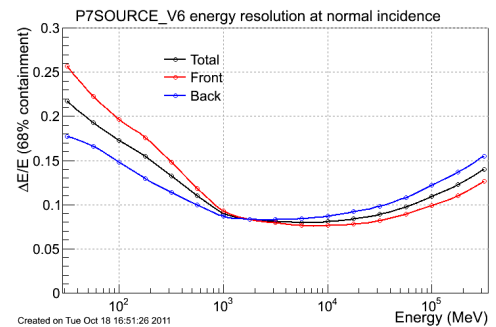
(b) The energy resolution of the front and back sections of the $Fermi$-LAT as a function of energy.

Figure 3.5.: The PSF and energy resolution of the $Fermi$-LAT for a photon with normal incidence angle. Image credit: Ackermann et al. (2012).

The $Fermi$-LAT features a large field of view (fov) of $\sim 2.4\,$sr, i.e., $20\,\%$ of the sky are visible to the instrument at any time. The usual observation mode is scanning the whole sky, uniform exposure is achieved by rocking the telescope perpendicular to the orbital motion. The telescope is rocked $50°$ north for one orbit and $50°$ south for the following orbit. In this mode the entire sky is covered after 2 orbits, i.e., 3 hours. From time to time so-called target of opportunity observations can interrupt the scanning, this happens if an earlier defined variable source of interest has an outburst. In 2013 the
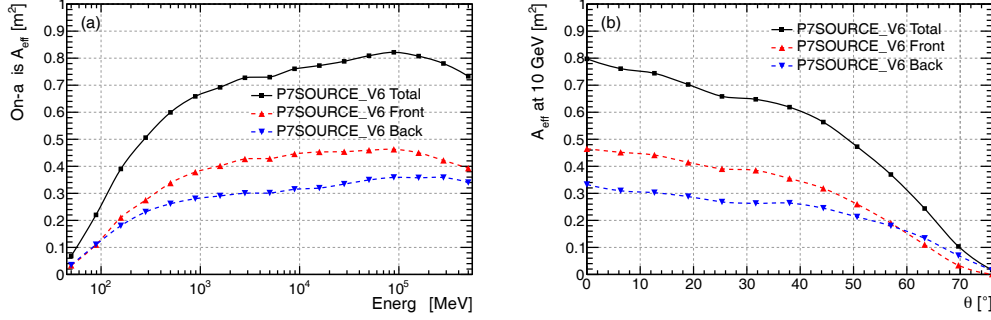
Figure 3.6.: The effective area of the *Fermi*-LAT, the left-hand side shows the dependence on the energy, the right-hand side on the incidence angle, respectively. Image credit: Ackermann et al. (2012).

Fermi collaboration decided to switch into a scanning mode which has a higher exposure on the galactic centre compared to other spots in the sky.

3.1.3. Fermi-LAT Data Analysis

This section summarises the different steps which are necessary to perform an analysis of *Fermi*-LAT data. The *Fermi*-LAT collaboration developed high-level analysis tools[2] to facilitate *Fermi*-LAT analysis. In principle it is possible to perform `UNBINNED` and `BINNED` analyses, the former treats each event individually while the events in the latter get binned in spatial and energy bins leading to a reduction in computing time. The `BINNED` method is recommended for most analyses, except for short time intervals with few events only. The following section summarises the different steps for a `BINNED` analysis which is used in this work.

Event and time selection

The events detected in the LAT get classified as photons according to different criteria for the signals in the tracker and the calorimeter. The different event classes are based on trade-offs between acceptable contamination levels by non-photon background, effective area and good spatial and energy resolution. The class optimised for point source analyses is `P7SOURCE` (the detailed class descriptions are explained in Ackermann et al. 2012). The corresponding Instrument Response Functions used are the so-called P7SOURCE_V6 IRFs.

---

[2]publicly available at `http://fermi.gsfc.nasa.gov/ssc/data/analysis/software/`

The data files provided by the *Fermi* Science Support Centre[3] are photon and spacecraft files. The former list various properties of the detected events and information of good time intervals (GTIs). The GTIs specify time intervals in which the spacecraft was in nominal observation conditions. The spacecraft files describe the position and orientation of the spacecraft for 30 second intervals.

The first step is to select events and time intervals valid for the analysis. The photons are selected based on time, energy, zenith, position on the sky, instrument coordinates, spacecraft conditions, and event classes. The region of interest (ROI) is typically defined as a circle with a radius of $15°$ around the position of the potential source. A strong source of photons in the *Fermi*-LAT energy regime is the Earth's upper atmosphere, thus photons with a zenith angle larger than $100°$ are usually excluded. The zenith angle is defined as the angle between the direction of the event and a line connecting the centre of the earth and the centre of mass of the spacecraft. In addition a cut on the rocking angle of the telescope is suggested, e.g., events detected in a time period where this angle is larger than $52°$ are rejected.

All cuts which are applied on the data and remove certain time intervals have an influence on the livetime, therefore the GTIs have to be recalculated. The data is then binned into a "count cube" (two spatial dimensions and one energy dimension) that defines the parameter space for the later fit.

Model selection

A model describing the known gamma-ray sources is needed since the whole ROI is fitted simultaneously. Each source is characterised by its photon flux density, that is separable into a spectral part dN/dE and a spatial part for most cases. The exception are sources with an energy-dependent morphology where the parts do not decouple.

The basic spectral shape used to describe the spectrum of gamma-ray sources is a power law, as expected from Fermi acceleration, described in Section 2.4.3:

$$\frac{dN}{dE} = N_0 \left(\frac{E}{E_0} \right)^{-\gamma} \tag{3.1}$$

with the prefactor N_0, the index γ and the scale E_0.

Dedicated analyses of sources have shown that modified spectral shapes better describe the observed spectra. The spectra of active galactic nuclei, the most common source class in the *Fermi*-LAT energy regime, are best described with a logParabola, defined as:

---

[3]http://fermi.gsfc.nasa.gov/ssc/

$$\frac{dN}{dE} = N_0 \left(\frac{E}{E_b} \right)^{-(\alpha + \beta \log(E/E_b))} \tag{3.2}$$

with the indices α and β and the break value E_b.

The spectra of pulsars typically follow power laws with super exponential cut-off:

$$\frac{dN}{dE} = N_0 \left(\frac{E}{E_0} \right)^{-\gamma_1} \exp \left(- \left(\frac{E}{E_c} \right)^{\gamma_2} \right) \tag{3.3}$$

with two indices γ_1 and γ_2 and the cutoff energy E_c. For point sources the units of dN/dE are $\mathrm{cm}^{-1}\mathrm{s}^{-1}\mathrm{MeV}^{-1}$ and for diffuse sources $\mathrm{cm}^{-1}\mathrm{s}^{-1}\mathrm{MeV}^{-1}\mathrm{sr}^{-1}$. An overview of all available models is given at the FSSC: `http://fermi.gsfc.nasa.gov/ssc/data/analysis/scitools/source_models.html`.

The available spatial models are point source, constant value, spatial map, and spatial cube. The spatial map uses a FITS image as a template to describe the distribution of photons on the sky. The spatial cube is a spatial map with an additional energy dimension, also provided in the FITS format.

The brightest source of diffuse gamma rays in this energy regime is Galactic diffuse emission, which can nicely be seen in Fig. 4.1. This emission is produced by the interaction of cosmic rays with the gas and radiation fields in our Milky Way and unresolved gamma-ray sources. A spectral and spatial model for this emission is provided by the *Fermi*-LAT collaboration and has to be included in every analysis. The second diffuse source includes extragalactic diffuse gamma-rays and misclassified cosmic-ray radiation. This emission is assumed to be isotropic and the file provided by the collaboration contains therefore only spectral information.

The known sources are also included in the model. The input model for known sources is the second *Fermi*-LAT source catalogue (Nolan et al. 2012, hereafter 2FGL). The 2FGL lists 1873 γ-ray sources detected in the $100\,\mathrm{MeV} - 300\,\mathrm{GeV}$ energy range. The sources are assumed to be point like with the exception of twelve previously-detected extended sources. The spectral shape of the sources depends on the observed properties. Pulsars are modelled with an exponentially cutoff power law, others are modelled with a power law or a logParabola if statistically significant curvature is detected.

The input model for the analysis consists of all sources listed in the 2FGL within a certain distance to the potential source. The distance has to be larger than the selection of the ROI since also sources from outside the ROI can contribute due to the large *PSF* of the *Fermi*-LAT, typically the radius is $\sim 5°$ larger than the ROI. The parameters for the closest sources are typically left free during the fit to ensure a proper spectrum determination. The normalisations of the Galactic and isotropic components are also released during the fit. They are a good indicator for the goodness of the fit.

Exposure calculation

The amount of measured photons depends on the time the instrument has looked at the source. To evaluate the amount of time the *Fermi*-LAT has spent observing a certain position in the sky, exposure maps are calculated. The exposure is defined as the effective area multiplied by the observation time for a given point in the sky. Since the effective area of the *Fermi*-LAT depends on the inclination angle of the photon (see, e.g., Fig. 3.6), one needs to know the amount of time the instrument has been observing at different inclination angles, the so-called livetime. The computation of the livetime for any position in the sky only depends on the orientation of the spacecraft. The livetime cube can therefore be precomputed to speed up the fitting procedure.

The exposure cube is then calculated for the same region as the count cube, the livetime cube is needed as input. The exposure cube is used to calculate the expected number of events for extended sources like the galactic diffuse component. The next step is to compute source maps which are model count maps for each source specified in the model. The spectrum of the source is multiplied by the exposure at the source position and convolved with the effective *PSF*.

Maximum likelihood analysis

The main challenges in the analysis of *Fermi*-LAT data are the limited statistics of photons originating in the source compared to a high background level and the *PSF* that varies with energy. The analysis of *Fermi*-LAT data is thus performed with a likelihood fit following Mattox et al. (1996). The likelihood is defined as the probability to obtain the measured data assuming a specific model. For a binned analysis as presented in this work the likelihood $\mathcal{L}$ is defined as the product of the probabilities for the individual bins. The distribution of events in one bin follows a Poisson distribution. The probability p_i to detect n_i counts in bin i is $p_i = m_i^{n_i} \cdot e^{-m_i}/(n_i!)$ with m_i being the average number of counts predicted by the model in bin i. The likelihood can then be calculated as

$$
\begin{aligned}
\mathcal{L} &= \prod_i p_i = \prod_i e^{-m_i} \cdot \prod_i \frac{m_i^{n_i}}{n_i!} \\
&= e^{-N_{\mathrm{pred}}} \prod_i \frac{m_i^{n_i}}{n_i!}
\end{aligned}
\tag{3.4}
$$

where $N_{\mathrm{pred}} = \sum_i m_i$ is the sum of counts predicted by the model. A higher probability is expected for a model that describes the data better than for a model which is not describing the data properly.

The model parameters are optimised by maximising the likelihood, or minimising the negative logarithm of the likelihood due to convenience in the calculation process:

$$-\log \mathcal{L} = \mathrm{N_{pred}} - \sum_i \mathrm{n}_i \cdot \log \mathrm{m}_i + \sum_i \mathrm{n}_i! \qquad (3.5)$$

The first term makes sure that model counts are "parsimoniously allocated" (Mattox et al. 1996): the likelihood increases with decreasing amounts of predicted events. The middle term increases the likelihood as counts are predicted in the bins where they occur. The last term is model-independent and can therefore be neglected. To detect gamma-ray emission from additional sources like the bow shocks we perform a likelihood ratio test using the test statistic (TS):

$$\mathrm{TS} = -2 \cdot \log \frac{\mathcal{L}_{\mathrm{max},0}}{\mathcal{L}_{\mathrm{max},1}} \qquad (3.6)$$

where $\mathcal{L}_{\mathrm{max},0}$ and $\mathcal{L}_{\mathrm{max},1}$ are the maximum likelihood for a model without the source (null hypothesis) and with the additional source, respectively. Wilks' theorem (Wilks 1938) states that the distribution of the TS follows a χ_n^2 distribution with n degrees of freedom, where n is the difference of degrees of freedom in the null hypothesis model and the alternative model, if the true data is distributed as the null hypothesis and the models are nested. The significance of the source can therefore be approximately calculated as the square root of the TS value if there is one additional degree of freedom.

The input files for the fit are the count cube, the spacecraft file, the source model, the exposure cube, and the livetime cube. The goal of the fit is to find the set of parameters that maximise the likelihood, this is accomplished in an iterative process.

Spectral points

The likelihood fit of the model to the data is performed over the entire energy range. Spectral points are calculated to reveal possible deviations from the assumed spectral shape. The energy range is split into bins, typically equally spaced in logarithmic energy. In each bin a fit is performed to determine the prefactor of the source, the parameters of the other sources are fixed, except for the normalisations of the diffuse components. The likelihood fit also allows to determine the significance of the source in each bin. Upper limits are calculated if the source is not detected with a sufficient TS, typically $\mathrm{TS} \geqslant 4$ if the source is significant over the entire energy range. For each bin, i.e. each data point, the residual value can be calculated as the relative difference of the expected counts (calculated from the overall model fit) and the data point. From this the spectral points are calculated.

3.2. Very-High Energy Regime

The flux of photons from cosmic sources decreases strongly with increasing energy. The reference source in this energy regime is typically the Crab Nebula. Its flux above $1\,\text{TeV}$ is $\sim 1{\cdot}10^{-7}\text{m}^{-2}\text{s}^{-1}$, meaning that a large area is needed to detect several photons in a reasonable amount of time. Space measurements with collection areas $\geqslant 1\,\text{m}^2$ are not feasible. Instead, the Cherenkov light from secondary particles of the interaction of the photon in the atmosphere is detected with ground-based instruments. The typical collection area of the ground-based telescopes is $\sim 10^5\,\text{m}^2$.

3.2.1. The Technique: Imaging Atmospheric Cherenkov Telescopes

In this section the technique of imaging atmospheric Cherenkov telescopes is explained. The basic ingredients are very-high energy photons hitting the Earth's atmosphere and producing cascades of new particles, so-called air showers. The principles of air showers are outlined in the first part of this section. The second physical process exploited by this technique is the Cherenkov effect, explained in detail afterwards. The telescopes used to detect this radiation are introduced in the last part.

Air Showers

High-energy photons entering the Earth's atmosphere typically react at a height of about 10-20 km in the Coulomb field of a nucleus creating an electron-positron pair as described above. These secondary particles are highly energetic as well and produce new particles via Bremsstrahlung, followed by even more particles. Bremsstrahlung is created when charged particles are decelerated by other charged particles. The energy is then released in the form of a photon. The number of particles in the shower increases until absorption effects, mainly ionisation and excitation of atmospheric nuclei, start to dominate over pair creation and bremsstrahlung. The energy at which that happens is called "critical energy" E_c, in air $E_c \sim 80\,\text{MeV}$ (Beringer et al. 2012). The characteristic length scale is the so-called radiation length X_0, in air $X_0 = 36.62\,\text{g/cm}^2$ (Beringer et al. 2012). It describes the amount of matter traversed by a high-energy electron before it loses all but $1/e$ of its energy due to bremsstrahlung and at the same time it equals 7/9 of the mean free path for pair production.

A model to describe the evolution of an electromagnetic shower was introduced by Heitler (1954). It takes only bremsstrahlung and pair creation into account and neglects the difference in length scale between the two. Further simplifications, also shown in Fig. 3.7, are: both parts of the electron positron pair get the same amount of energy during pair

creation and electron and positron radiate the bremsstrahlung photon at X_0 and lose half their energy to it.
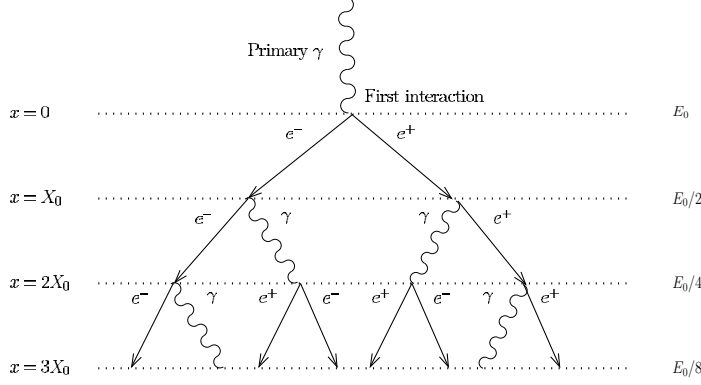
Figure 3.7.: Schematic view of an electromagnetic shower in the Heitler model. Figure credit: Funk (2005).

The model illustrates several important properties of the shower despite its simplifications. Assuming a gamma ray with energy E_0 the cascade develops and the number of particles (N_n) after $n = X/X_0$ radiation lengths as well as the mean energy of the particles (E_n) can be calculated:

$$N_n = 2^n \qquad \text{with} \qquad E_n = E_0 \cdot 2^{-n} = E_0/N_n \tag{3.7}$$

The number of particles reaches its maximum at the critical energy, hence:

$$X_{max} = \frac{X_0}{\ln 2} \cdot \ln \frac{E_0}{E_c} \qquad \text{and} \qquad N_{max} = E_0/E_c. \tag{3.8}$$

The maximum number of particles N_{max} is proportional to the energy of the photon E_0 and the maximum depth X_{max}. The position of this so-called shower maximum is proportional to the logarithm of the photon energy. The typical value for X_{max} is $\sim 10\,\mathrm{km}$ for a $1\,\mathrm{TeV}$ photon, the diameter of the air shower on the ground is $\sim 200\,\mathrm{m}$ (increasing with energy of the incident gamma) and a thickness of ~ 1–$2\,\mathrm{m}$ (Aharonian et al. 2008).

Air showers are not only created by photons, but also by electrons, protons and heavier nuclei hitting the Earth's atmosphere. The showers initiated by electrons are also only electromagnetic and thus very similar to the photon induced ones. Showers originating from electrons develop higher in the atmosphere and inherit a broader lateral distribution. The influence of the geomagnetic field is stronger for the electron showers and their thickness is larger (Sahakian et al. 2006). These differences can be used to separate

photon and electron induced showers. The hadronic air showers from protons and heavier nuclei are much more numerous and constitute the main background for the detection of photon induced air showers.

The development of a hadronic shower is depicted in Fig. 3.8. In contrast to the development of electromagnetic showers also strong and weak force interactions play an important role. The inelastic scattering off nuclei leads to many secondary particles. Hadronic showers comprise many parts: pions and fragments of nuclei, electromagnetic sub-showers created by gamma rays from the decay of π^0, muons being the decay products of charged mesons, and neutrinos produced in different decay channels. The variety of interaction processes leads to much more irregular showers. Especially the strong force interactions lead to a larger transverse momentum transfer. Electromagnetic showers are closely aligned with the shower axis, which is not the case for hadronic ones. Another difference is that for hadronic showers only about one third of the energy is contained in the electromagnetic sub-showers, long-lived secondary particles like $\mu^{+/-}$ and ν leave the shower region.
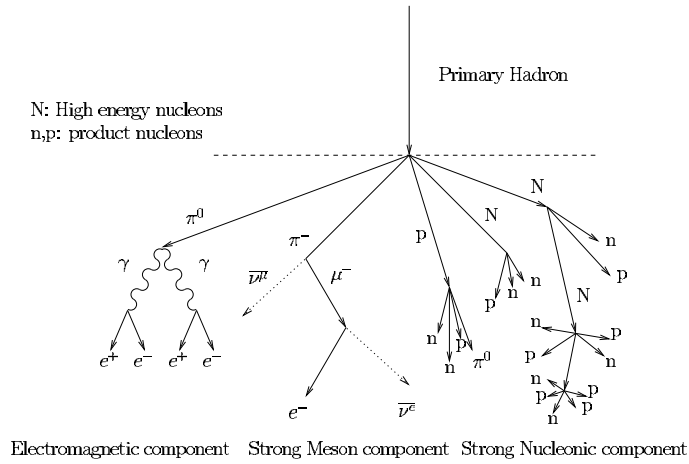
Figure 3.8.: Schematic view of an hadronic shower. Figure credit: Funk (2005).

Cherenkov radiation

Charged particles that travel through a medium induce a polarisation of the atoms in the medium. If the velocity v of the charged particle is larger than the speed of light in the medium $c_n = c_0/n$ (where c_0 denotes the speed of light in vacuum and n the refractive index of the medium) a coherent shock wave is emitted. A common analogon is the sonic boom that aircrafts create when travelling faster than the speed of sound.
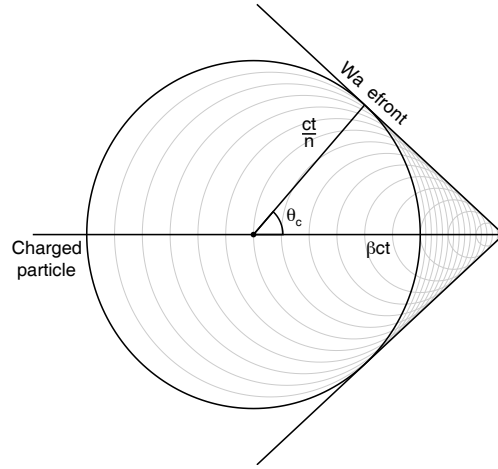
Figure 3.9.: Schematic view of the Cherenkov light cone emitted by a particle travelling at a speed $v = \beta \cdot c$. Figure credit: Baldini (2014).

The geometry of this emission is depicted in Fig. 3.9, the opening angle θ can be calculated as:

$$\cos \theta = \frac{c_n \cdot t}{v \cdot t} = \frac{1}{\beta n} \tag{3.9}$$

with $\beta = v/c_0$.

The secondary particles in air showers are energetic enough to emit Cherenkov light. The refractive index of air changes with altitude which infers an altitude-dependent opening angle of the Cherenkov cone, the angle is smaller for higher altitudes. The sum of the Cherenkov light from all particles in an air shower is therefore a blurry circle on the ground, with a radius of $\sim$120 m. A Monte Carlo simulation of the Cherenkov light from air showers is shown in Fig. 3.10. The pictures cover $400 \times 400 \, \mathrm{m}^2$ and the color scale depicts the amount of photons. The difference of electromagnetic and hadronic shower is striking, two different hadronic showers are shown to outline the more irregular pattern.

Cherenkov light is strongly peaked in the ultraviolet-blue wavelength range. Attenuation by scattering and absorption processes leads to a sharply cut off spectrum below 300 nm (Bernlöhr 2000). The duration of the Cherenkov flash from an electromagnetic air shower is 5–20 ns (Hinton 2009). A primary gamma ray with an energy of 1 TeV leads to $\sim$100 Cherenkov photons per square meter at 2000 m above sea level.

(a) 300 GeV photon.   (b) 1 TeV proton.   (c) Another 1 TeV proton.
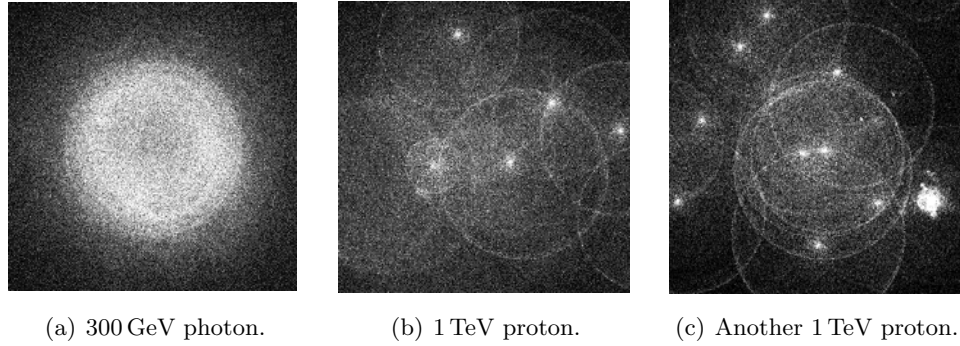
Figure 3.10.: Monte Carlo simulations of lateral distribution of Cherenkov light from air showers for a height of 2200 m above sea level. The area covers $400 \cdot 400 \, \text{m}^2$, the shower core is in the image centre, white pixels correspond to 80 or more photons per m^2. The images depict different incident particles, as written in the captions. Image credit: K. Bernlöhr[4].

Imaging Atmospheric Cherenkov Telescopes

Imaging atmospheric Cherenkov telescopes (IACTs) measure the Cherenkov light emitted by the secondary particles in air showers. The atmosphere is thus used as a calorimeter, with an altitude from sea level that corresponds to ~ 28 radiation lengths for vertically incident particles. The schematic of a stereoscopic IACT setup is shown in Fig. 3.11(a) where several telescopes detect light from the same shower. Each telescope focusses the Cherenkov emission of the shower onto a camera consisting of photo-multipliers and fast read-out electronics. The imaging is schematically depicted in Fig. 3.11(b). The image has an elliptical shape, the main axis of the ellipse corresponding to the shower axis.

The effective area of a telescope adds up to $\sim 10^5 \, \text{m}^2$ since the position of the telescope in the light pool is not critical. This huge area is beneficial in the comparison to instruments on board satellites with an area of the order of $1 \, \text{m}^2$. The energy threshold of the telescopes is inversely proportional to the mirror area since the number of Cherenkov photons increases with energy.

The cameras of the Cherenkov telescopes have to be very sensitive, since the typical photon densities for a 1 TeV shower are ~ 100 photons per m^2, and very fast, since the duration of the Cherenkov flash is a few nanoseconds, as pointed out in the previous paragraph. The triggering scheme of IACTs has to ensure that as many shower-induced events as possible get read out while background events get suppressed. To discriminate gamma-ray events against the night-sky background (NSB) originating in stars and other light sources, several trigger levels are installed. The camera is divided into sectors,

(a) Schematic view of the IACT principle, not to scale.

(b) Schematic view of the imaging of the Cherenkov light from the air shower particles. Image credit: Antonelli et al. (2009).
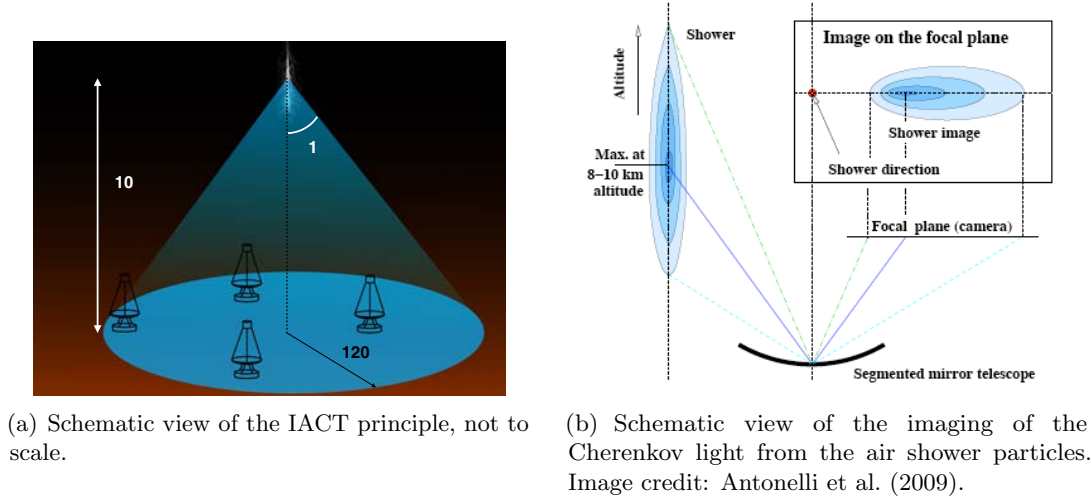
Figure 3.11.: Schematic view of the IACT principles.

in which a certain number of pixels needs to be above the pixel threshold to trigger the readout. The sectors are overlapping to ensure a uniform trigger response. For a stereoscopic event there is the additional central trigger, which requires coincident camera triggers from at least two telescopes. The central trigger reduces the amount of local muons and hadronic showers dramatically since the Cherenkov light from hadronic showers is less homogeneous.

History of IACTs

VHE gamma-ray astronomy is a quite young and dynamic field, a nice summary of the status in 2008 and the road to it is presented in Weekes (2008) and Aharonian et al. (2008). The idea to measure the Cherenkov light from air showers was proposed by Jelley & Porter (1963). The first TeV gamma-ray observatory in the US is shown in Fig. 3.12(a): The telescopes, built from searchlight reflectors from World War II, were manually operated and the computer-free analysis revealed no sources.

Weekes & Turver (1977) pioneered the idea to use large reflectors and pixellated cameras. The 10 m *Whipple* telescope was constructed in 1982 and lead to the first detection of an astrophysical source, the Crab Nebula, with an IACT in 1989 (Weekes et al. 1989). By now the third generation of IACTs is operating, the VERITAS telescopes in the US (at the exact same spot as the telescope in Fig. 3.12(a)), the MAGIC telescopes on the Canary Island of La Palma and the H.E.S.S. telescopes in Namibia.

(a) The first TeV gamma-ray observatory in the United States consisted of two searchlight reflectors from World War II with a size of 1.5 m each. They were operated in the year 1967. Image from Weekes (2008).

(b) The H.E.S.S. telescope array consisting of five telescopes, situated in the Khomas Highland in Namibia. The first telescope was operational in 2002, the large telescope was inaugurated in 2012.

Figure 3.12.: From first generation IACTs to third generation IACTs.

The improvements in the detectors revealed a huge number of sources, the evolution of source detections as a function of time is shown in Fig. 3.13. The big success of this technology lead to the foundation of the Cherenkov Telescope Array (CTA) consortium, comprising experts from all current Cherenkov telescope collaborations. Its aim is to build an array of $\sim$80 Cherenkov telescopes at two sites, one in the southern and one in the northern hemisphere. The sensitivity for CTA is expected to be a factor of $\sim$10 more sensitive than current instruments, see Fig. 3.19.

3.2.2. The Instrument: H.E.S.S.

The high energy stereoscopic system (H.E.S.S.) is an array of five imaging atmospheric Cherenkov telescopes. It is located in the Khomas Highland in Namibia ($23°16'18''$ S, $16°30'01''$ E) at 1800 m above sea level. The location in the southern hemisphere was chosen to allow for observations of the inner regions of the Galactic plane. The scan of the inner region of the galactic plane revealed a wealth of sources (Aharonian et al. 2006) reflected in the dramatic increase in source discoveries in Fig. 3.13. Phase I of the array denotes the time from 2002 (first telescope inaugurated) or 2004 (all four telescopes inaugurated) until 2012, when the fifth telescope saw first light, the system is since then called H.E.S.S. Phase II. A picture of H.E.S.S. Phase II is shown in Fig. 3.12(b).

The four H.E.S.S. 12 m telescopes are arranged in a square of 120 m side length. The distance of the telescopes is optimized between a large effective area and a high probability
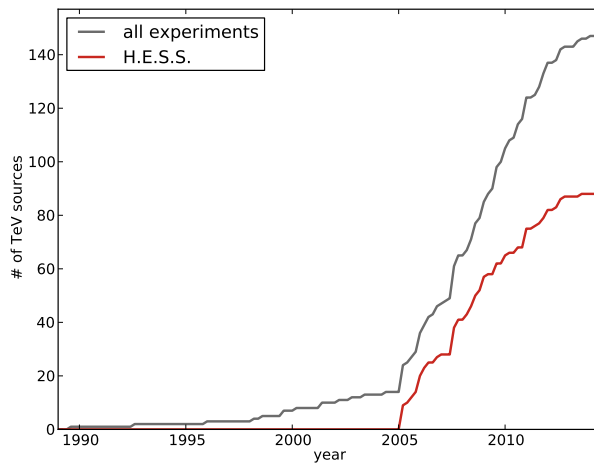
Figure 3.13.: The number of sources detected in the VHE regime as a function of time, data as listed by: `http://tevcat.uchicago.edu`. The grey line represents the discoveries by all experiments, the red line the ones by H.E.S.S. only.

to observe stereoscopic events. The H.E.S.S. 28 m telescope is placed in the centre of the square and extends the energy range to lower energies. In the course of this work only data taken during H.E.S.S. Phase I is used. A picture of two of the H.E.S.S. 12 m telescopes is shown in Fig. 3.14.

The key elements are the $107 \, m^2$ mirror area, the alt-azimuth mount, and the camera. The mirror of each telescope consists of 382 round facets with a diameter of 60 cm each and a focal length of 15 m. The mirrors are arranged in a Davies-Cotton design, meaning that the individual mirrors are positioned on a sphere with a radius equal to the focal length. This layout ensures a good off-axis imaging at the cost of higher time differences for different incident positions. The camera has a diameter of 1.6 m and consists of 960 Photomultipliers (PMTs) adding up to a $5°$ field of view. Winston cones are placed in front of the PMTs to close the gaps between the PMTs and to shield them from light that is not coming from the telescope's mirror.

3.2.3. H.E.S.S. Data Analysis

This section outlines the different steps needed to perform an analysis of IACT data. The first challenge is to infer the photon's properties from the image of the Cherenkov light emitted by the charged particles in the air shower. The second important step is

Figure 3.14.: Two of the H.E.S.S. 12 m telescopes, each with 382 mirror facets. Credit: H.E.S.S. collaboration.

to distinguish gamma-ray induced air showers against the outnumbering background of cosmic ray induced showers. The analysis starts with the calibration, which is outlined first. Then two types of analyses are presented: The Hillas analysis is based on the second moments of the image and is used by most IACTs. It also serves as input for the more advanced Model analysis described in the last part.

Calibration

The PMTs in the cameras are read out via three different channels, one for the trigger and two channels to ensure an optimal processing of faint and bright signals from the air showers. The "high gain channel" has a dynamic range from 1–150 photo electrons (PE) with a precision of single PE while the "low gain channel" covers the range from 20–2000 PE. The analogue signal from the PMTs is integrated over a 16 ns read out window and digitised via an analogue-to-digital converter (ADC). The calibration of the two channels are performed in a sophisticated procedure including the calculation of the conversion factor from ADC counts to PE, the differences in response for different PMTs, and the pedestal values for both channels (the baseline of the PMTs consisting of electronic noise and NSB photons). To get a final camera image the information from both channels is merged and hardware defects, like broken pixels or oversaturated pixels due to bright stars, are taken into account.

The conversion from photo electrons into Cherenkov photons is done with images of atmospheric muons. The Cherenkov light emitted by the muons has a similar radiation spectrum as gamma-ray induced showers, the only difference being that muons penetrate deeper and their light is thus less absorbed. The light yield of the ultra-relativistic muons does not depend on their energy since the Cherenkov angle saturates at these energies, but on the track length only. The overall optical efficiency of the H.E.S.S. telescope system including PMTs, mirrors, etc. is around 10 % (de Naurois 2012).

Image cleaning

The camera images include not only the photons originating from the air shower but also photons from other sources. Before an analysis of the image is performed, it is important to ensure that all detected photons belong to the air shower. The background photons from the night sky background originating from star light and other ambient light sources have to be separated. Another background is the electronic noise in the pixels.

The so-called "image cleaning" discards all pixels that do not fulfil the threshold criterion: the amplitude of the pixel is above 10 PE and at least one of its neighbours' above 5 PE or vice versa. The two threshold values can be adjusted in the analysis, 5 and 10 PE are generally used by H.E.S.S.
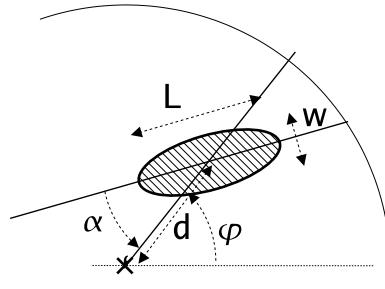
Figure 3.15.: Geometrical definition of the Hillas parameters. Image from: de Naurois (2012).

Hillas Analysis

A very fast and robust way to analyse images from IACTs was proposed by Hillas (1985). He shows that the discrimination between gamma-ray showers and hadronic showers based on the width, length and orientation of the Cherenkov images is possible, even

with a camera with rather large pixels as the *Whipple* telescope, which saw first light in the same year.

The Hillas analysis is based on the second moments of the camera image. The shower parameters are: the length (L) in the direction of the major axis, the width (W) in the direction of the minor axis, the centre of gravity of the image (COG), the orientation angle of the major axis in the camera coordinate system (α), the total sum of the pixel amplitudes, the nominal distance (d) between camera centre and COG, and the azimuthal angle of the image main axis (φ).

The image shape does not only depend on the type of particle, but also its energy and the orientation with respect to the telescope. The impact parameter is defined as the shortest perpendicular distance of the shower axis to the telescope. Look-up tables are created from simulations to reconstruct the energy of the primary particle depending on the impact distance and the image size.

The observation of one shower with two or more telescopes, so-called stereoscopic events, allows for a much better direction reconstruction since the origin of the shower is located at the intersection point of the main axes of the ellipses, see Fig. 3.16. The shower impact point can also be constructed geometrically by the intersection of the planes defined by the telescope positions and the shower track. The energy is calculated with a weighted average of the energies reconstructed by the individual telescopes.
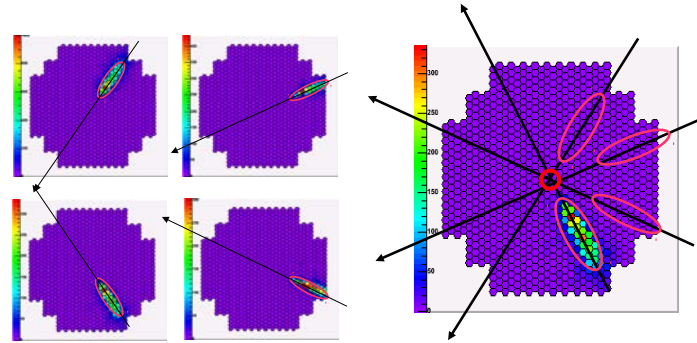
Figure 3.16.: Geometrical reconstruction of the shower direction using four telescope images. The direction of the primary particle has to lie on the main axis for each image. Left: superposition of all four camera images, leading to the direction reconstruction, depicted by the red circle. Image from: de Naurois (2012).

The Hillas parameters can be used to distinguish between showers induced by gammas and hadrons, the so-called gamma-hadron separation. The *scaled width* and *scaled length* are calculated by comparing the width and length to distributions obtained from simulations: The expectation value from the simulation is subtracted from the corresponding image

parameter and divided by the variance of the parameter from the simulations. The advantage of the scaled parameters is their independence of energy which allows for an energy independent selection efficiency. In stereoscopic observations the scaled parameters are combined to the *mean scaled width* and *mean scaled length*. By cutting on the *(mean) scaled width* and *length* a large part of the background can be rejected, for details the reader is referred to de Naurois (2012).

Model Analysis

The Model analysis is more sophisticate. Its basis is a likelihood fit of the calibrated, uncleaned camera images to model images generated by a semi-analytical model. The application to H.E.S.S. data is presented in de Naurois & Rolland (2009). The semi-analytical model describes the shower development, the spatial distribution of the charged particles and includes the depth of first interaction as a shower parameter. The shower images are simulated for 40 zenith angles, 40 impact distances, 64 different energies, and 6 first interactions depths; two examples are shown in Fig. 3.17 for a 1 TeV shower with two different impact distances. The night sky background, leading to noise in the pixels, is included in the modelled images based on a statistical analysis.
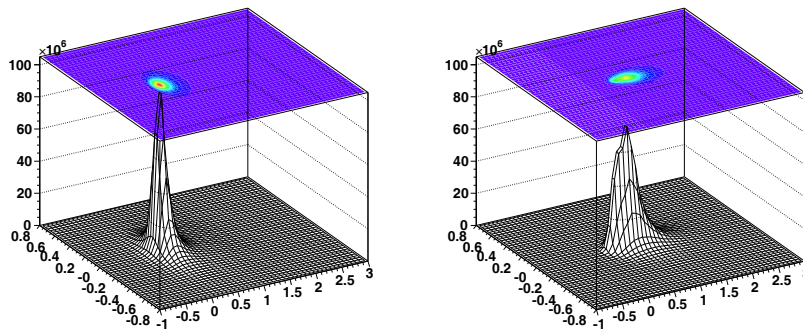
Figure 3.17.: Model of a 1 TeV shower started at one radiation length and an impact parameter of 20 m (100 m) on the left-hand (right-hand) side. Image from: de Naurois & Rolland (2009).

A Levenberg-Marquardt fit algorithm is used to compare the actual shower images with the ones from the simulation on a pixel-per-pixel level. Contrarily to the Hillas analysis no cleaning is needed since all pixels in a camera image are included in the fit taking night sky background variations properly into account. The best matching model and the corresponding shower parameters are determined in one minimisation procedure for all participating telescopes. The start parameters for the fitting procedure are obtained from

a Hillas reconstruction with different cleaning levels. A variable called *goodness-of-fit* is introduced to reject background events in a way that increases the signal to noise ratio. It compares the pixel log-likelihood with its expectation value and therefore serves as an estimator for the fit quality. This value is calculated after the fitting procedure for each pixel and two sums are calculated: the *ShowerGoodness* and the *BackgroundGoodness*. The *ShowerGoodness* includes all pixels belonging to the shower, defined as having an expected amplitude above 0.01 PE. The remaining pixels are added to construct the *BackgroundGoodness*, which is very sensitive to hadronic clusters outside the main shower image. The goodness parameters are again scaled to have cut values which do not dependent on energy or other parameters. The standard cuts for the Model analysis, outlined in de Naurois & Rolland (2009) and also used in this work, are: an image amplitude $\geqslant 60$ PE per telescope, a nominal distance $\geqslant 2°$, a shower goodness $\geqslant 0.6$, a reconstructed primary interaction depth between -1 and 4 X_0, and a squared angular distance cut of $\theta^2 \geqslant 0.01 \deg^2$ (for a point source). For faint sources the cuts are adjusted to: an image amplitude $\geqslant 120$ PE per telescope, a shower goodness $\geqslant 0.4$, and a squared angular distance cut of $\theta^2 \geqslant 0.005 \deg^2$ (for a point source).

The sophisticated analysis leads to an improved performance, e.g. better angular and energy resolution and a higher signal to noise ratio, and higher robustness against environmental and instrumental effects. The sensitivity is up to a factor ~ 2 better than for the Hillas parameter technique.

Background estimation

To make reliable statements on the position, extension, significance, and spectrum of a gamma-ray source, it has to be ensured that the reconstructed air showers are truly originating from the potential gamma-ray source. The high number of hadronic air showers is diminished by the gamma-hadron separation as described before. The resulting background are gamma-like hadronic and electron induced showers which passed the cuts, and a possible diffuse gamma-ray background. Different methods to determine this background are outlined in the following (based on Berge et al. 2007).

The first step is to define an "ON" region, where the potential source is situated, and "OFF" regions, where no source is expected and which can thus be used to infer the background in the ON region. The number of excess counts (N_{excess}) is calculated with the number of events in ON and OFF regions (N_{on} and N_{off}) and the factor α correcting for differences between the ON and OFF region, e.g. size, exposure, zenith angle.

$$N_{\mathrm{excess}} = N_{\mathrm{on}} - \alpha N_{\mathrm{off}} \qquad (3.10)$$

The number of background counts is determined in the OFF region, which is chosen to best mimic the ON region. An ideal background region has the following characteristics: it is contemporaneous to limit the effect of ageing parts of the system, it has the same angular distance to the observation position as the source, it is in a similar position in the sky concerning the night sky background level, and it has high statistics to decrease fluctuations, and has a similar acceptance as the ON region.

Different background estimation strategies are pursued depending on the analysis type. The most used approaches are the ring and the reflected-region methods, schematically shown in Fig. 3.18. The data in this image are taken in so-called wobble mode. The telescopes are pointed off the source position, alternating between $\pm 0.5°$ in declination, the observation positions are depicted with yellow circles. The ring method defines the
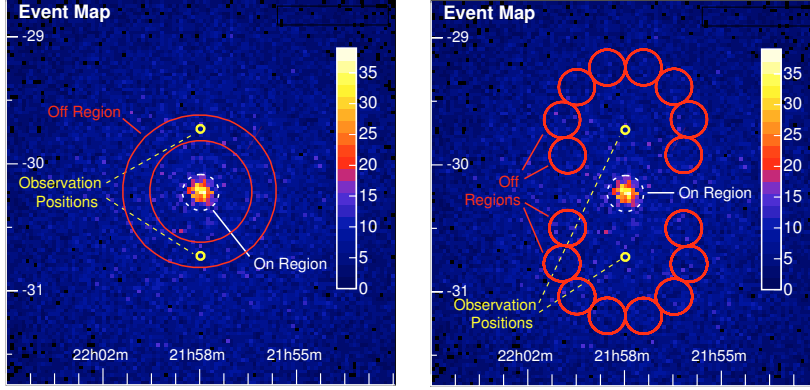
Figure 3.18.: Count map of γ-like-events from 5 h of H.E.S.S. observations of the active galaxy PKS 2155-304. Overlaid are schematic illustrations of the ring- and reflected-region-background method on the left-hand and right-hand side, respectively. Image from: Berge et al. (2007).

OFF regions as a ring around the source position in celestial coordinates. The acceptance, i.e. the probability to detect photons, depends on the distance to the camera center. Since the acceptance is not constant across the ring a correction factor for each point, depending on the distance to the observation position, is added to the α calculation.

To estimate the background in wobble observations, as shown in the image, the reflected region method was invented. The OFF regions are a ring of circular regions, each of the same size as the ON region, reflected around the observation position. The distance of the OFF regions to the observation position is exactly the distance between source and observation position. This has the advantage that no radial acceptance correction is needed and α is simply $1/n_{\text{off}}$. This method is ideally suited for spectral analyses.

The significance of an excess can be calculated following the famous formula 17 by Li & Ma (1983), the only input parameters are $N_{\text{on}}, N_{\text{off}}$, and α:

$$S = \sqrt{2}\sqrt{N_{\text{on}} \ln\left[\frac{1+\alpha}{\alpha}\left(\frac{N_{\text{on}}}{N_{\text{on}} + N_{\text{off}}}\right)\right] + N_{\text{off}} \ln\left[(1+\alpha)\left(\frac{N_{\text{off}}}{N_{\text{on}} + N_{\text{off}}}\right)\right]} \quad (3.11)$$

They developed the method for an on-off observation, where an observation of a source is followed by a dedicated off observation. But the same formula for (N_{excess}) as Equation 3.10 is used and the results can thus also be applied to the above described background methods. They show that several formulae used by various collaborations to calculate significances are mathematically unstable. But formula 17 is shown to give consistent results with simulations under the following constraints: $N_{\text{on}} \gtrsim 10$, $N_{\text{off}} \gtrsim 10$, and $0.1 \leqslant \alpha \leqslant 10$. A formula to calculate the confidence level is also given.

Spectrum calculation

To fit a spectrum to the data a forward-folding technique is used: in the first step a spectral model (e.g. a power law as in Equation 3.1), depending on true energy, is convolved with the instrument response functions (IRFs). The spectrum calculation relies on the comparison of on and off events just like described above. The background determination is therefore a crucial part. The reflected region technique is used since it introduces less systematic effects due to its inherent design. Otherwise an energy-dependant α factor would be needed.

The number of expected gamma-ray events per reconstructed energy bin is calculated by integrating the source flux convolved with the energy dispersion and effective area over the reconstructed energy and true energy. The best fit parameters and the corresponding covariance matrix are determined in a likelihood fit of the convolved model to the measured data, which also results in the number of expected events per bin. Residual spectral points are calculated in each energy bin to show deviations between observed and expected counts. The flux uncertainty at each energy is calculated from the spectral parameters and the covariance matrix.

3.3. Upper Limit Calculation

The ultimate goal of observations is the detection of significant emission from a gamma-ray source. Nevertheless, a non-detection also represents a valuable result. In gamma-ray astronomy different approaches are used to calculate upper limits, i.e. the flux level which can be excluded by the measurement at a certain confidence level. The model analysis in

H.E.S.S. relies on Feldman & Cousins (1998) which is a Frequentist formulation. The Frequentists' way of thinking is to integrate along possible realisations of the experiment, leading to a upper limit definition like "if the amplitudehad been larger than this, it would have been detected with a certain confidence level".

The *Fermi* Science Tools have this method as well as a Bayesian method following Helene (1983) implemented. The Baysians main ingredients are the probability density function and two hypothesis, null (being background) and one (being signal). The upper limit is calculated as upper integration bound for which the probability assuming the signal hypothesis is larger than a certain confidence level.

For a comparison of the two approaches, the reader is referred to Röver et al. (2011). The main argument against the Bayesian approach is that the distribution depends on the degree of belief, visible in the formulation of the prior, and is thus subjective. But the Frequentist approach can have the problem of unphysical parameters, the range the parameter can have is not limited. This is not true for the Bayesian calculation, the parameter range is part of the calculation procedure. Thus the Bayesian method is used for the calculation of the upper limits in the *Fermi* analyses.

3.4. Performance Comparison

Despite the differences in the detection principle and the analysis, the performance of both techniques (pair-conversion telescopes and imaging atmospheric Cherenkov telescopes) is comparable. Funk et al. (2013) show a comparison of the performance of *Fermi*-LAT, H.E.S.S., and the future High-Altitude Water Cherenkov Observatory (HAWC[5]) and the earlier mentioned Cherenkov Telescope Array (CTA[6]). The curves for CTA are preliminary in a sense that neither the site nor the array layout are yet decided.

HAWC uses a different method to observe TeV gamma rays and cosmic rays: many particle detectors, which measure the air shower particles, are placed on the ground. The air shower arrays started with scintillation detectors, but the newer generation uses water tanks in which the particles create Cherenkov light that is detected by photo detectors. The advantage of air shower arrays is the high duty cycle: The arrays can operate during the day and bad weather conditions. The main disadvantage is the worse discrimination between gamma rays and cosmic rays. The other performance parameters are shown in this section. For the analyses performed in this work no data from air shower arrays is used.

---

[5]http://www.hawc-observatory.org
[6]http://www.cta-observatory.org

The sensitivity for an E^{-2} type power law spectrum, shown in Fig. 3.19, compares 10 years of *Fermi*-LAT observations with 100 hours of H.E.S.S. and CTA observations. The performance of the *Fermi*-LAT depends on the location of the source in the Galaxy, therefore two scenarios are distinguished: "inner Galaxy" refers to a source at $l = 10°$, $b = 10°$, "extragalactic" to a source not influenced by Galactic diffuse emission. In the overlapping energy region the sensitivity of the *Fermi*-LAT is limited by the amount of collected photons and thus $\sim E^1$. The IACT sensitivities are limited by systematic uncertainties, hence do not improve with longer exposure times. For HAWC no sensitivity is shown since it was not provided by the collaboration.
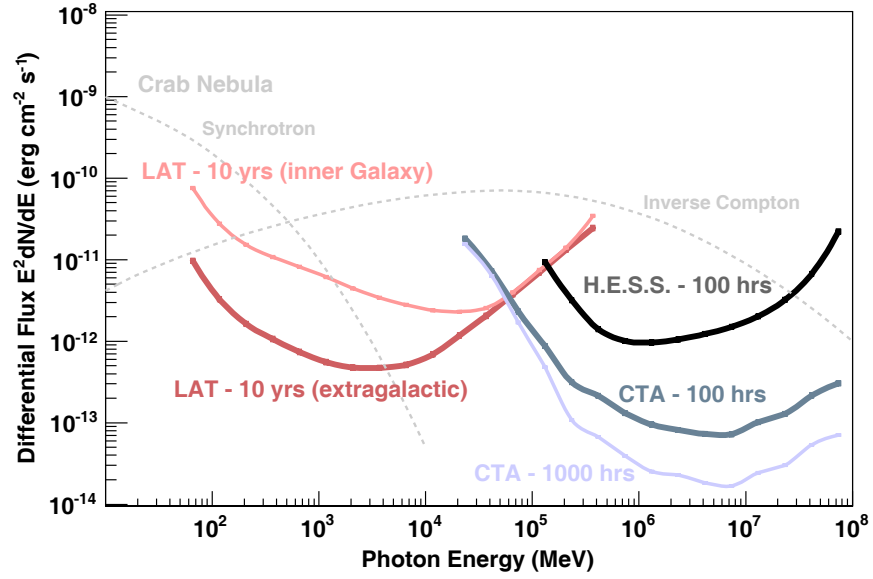
Figure 3.19.: Differential sensitivity for a minimum significance of 5σ per bin, minimum 10 events per bin and 4 bins per decade in energy. The curve "inner Galaxy" refers to a source at $l = 0°$, $b = 10°$, "extragalactic" to a source not influenced by Galactic diffuse emission. Image credit: Funk et al. (2013).

The angular and energy resolution are essential to be able to resolve the spatial and spectral distribution of photons of a gamma-ray source. Also shown are the curves for HAWC, which is not competitive concerning these parameters. The dashed line in Fig. 3.20(a) represents the limit for IACTs obtained from simulations (performed by Hofmann 2006), assuming that all Cherenkov photons could be detected by the telescope. The limiting factor are the inherent fluctuations in the particle showers.

The performance plots also show the great opportunities and the complementarity of the two approaches. Space and ground based gamma-ray telescopes have energy ranges not
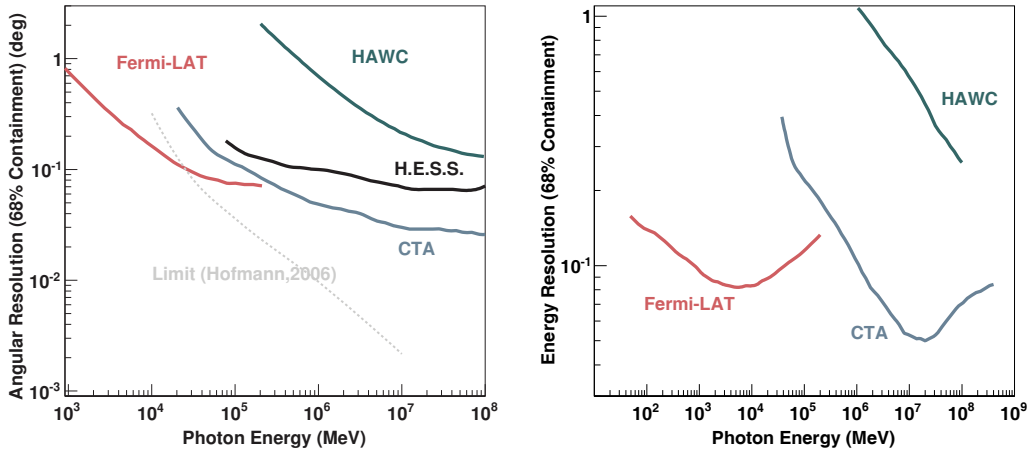
Figure 3.20.: Angular and energy resolution of *Fermi*-LAT, H.E.S.S., and CTA. Image credit: Funk et al. (2013).

covered by any other instrument and the overlapping energy range provides a unique opportunity to perform cross-calibrations of the instruments. To study the gamma-ray emission from bow shocks of runaway stars, analyses with both instruments are performed in the course of this work, outlined in Chapter 4.

4. Gamma-Ray Analyses of Bow Shocks of Runaway Stars

This chapter describes the analyses of gamma ray emission from bow shocks of runaway stars in the HE and VHE range performed during this work. The reconstruction and analysis approaches in the two energy ranges are quite different as described before. The analyses were performed with the dedicated analysis software provided by the *Fermi*-LAT and H.E.S.S. collaborations as described in the previous chapter.

The analyses can be performed in a single framework when starting from photon lists. This idea is pursued in the *GammaLib/ctools* analysis framework. It is developed in the CTA community as a high-level analysis software. CTA will be the first IACT array operated as an open observatory with publicly available software. A unified analysis framework offers great possibilities. The development on *GammaLib/ctools* has started and the first results are very promising, details are outlined in the Appendix A. Since several methods remain to be implemented in *GammaLib/ctools* and the work on systematic studies has just started, all analyses presented here are performed with the standard analysis software packages.

The chapter starts with the *Fermi*-LAT analyses of the bow shock candidates. The distribution of the bow shock candidates from the E-BOSS catalogue on the sky is shown in Fig. 4.1 overlaid on a *Fermi*-LAT count map for 57 months of data. The count map is created by selecting events between $100\,\mathrm{MeV}$ and $300\,\mathrm{GeV}$. The binning is $0.1°$ and the map is displayed in an Aitoff projection. The sum of all photons in this map is 66,414,865. All but one bow shock candidate listed in the E-BOSS catalogue are analysed in a pipeline as described in the first section. This analysis is published in Schulz et al. (2014). The only exception is HIP 101186, which is spatially coincident with a 2FGL source and therefore treated separately as described in Sec. 4.4.

The second part of the chapter describes the H.E.S.S. analysis of seven bow shock candidates. No dedicated observations were performed on this source class, but during the scan of the inner Galactic plane and other sources some bow shock candidates were observed serendipitously.
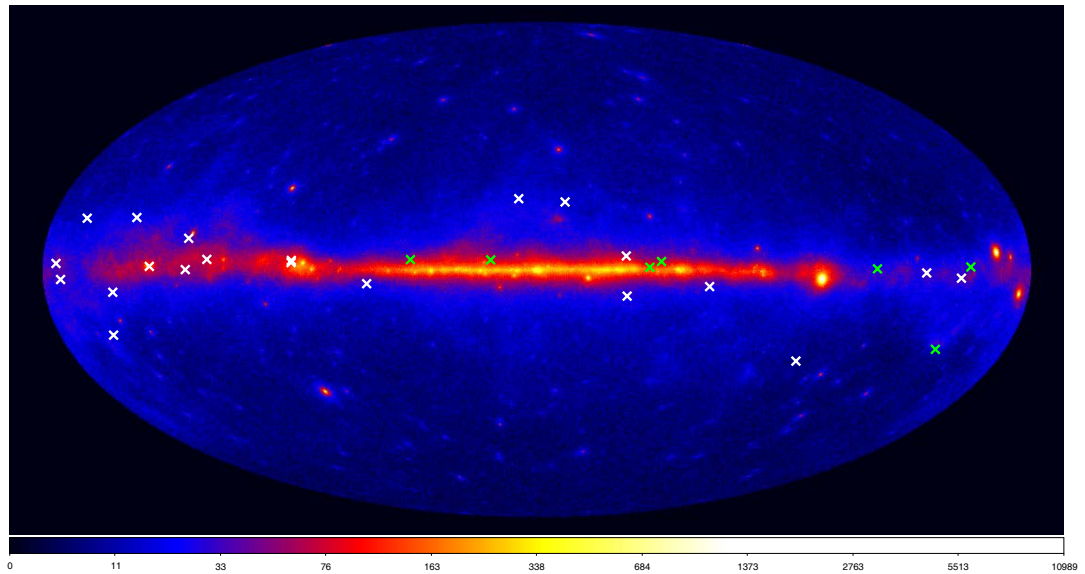
Figure 4.1.: Positions of the E-BOSS catalogue candidates as white crosses, the ones with H.E.S.S. exposure are depicted with green markers, overlaid on the *Fermi*-LAT count map from 57 months of data. The photons are selected to have energies between $100\,\mathrm{MeV}$ and $300\,\mathrm{GeV}$.

4.1. Pipeline Analysis (Fermi-LAT)

A pipeline was constructed to analyse all bow shock candidates with the same procedure. The relevant parameters for the analysis are listed in Tab. 4.1.

The analyses were performed as described in Section 3.1: the events were selected according to the parameters specified in Tab. 4.1, followed by the calculation of the good time intervals (GTIs). The data was binned into the count cube and input models were created. Since the livetime calculation is computationally intensive it was decided to precompute the livetime cube for the entire sky and all ROIs. This implies that the same GTIs are used for all bow shock candidates. In particular it was impossible to exclude time intervals when individual sources were observed under high zenith angles. This effect was mitigated by using a conservative cut on the zenith angle in the event selection. The likelihood fit was performed with the 2FGL catalogue as input model. The investigated bow shock candidates were modelled as point sources at the star's position, with the exception of four bow shocks, outlined in the next paragraph. All fit results were validated with the investigation of residual maps and TS maps.

Parameter	Value
Science Tools version	v9r29p0
Time cuts in `gtmktime`	DATA_QUAL==1 && (LAT_CONFIG==1)
	&& ABS(ROCK_ANGLE) ⩽ 52
Event class	P7SOURCE
IRF	P7SOURCE_V6
Diffuse models	*gal_2yearp7v6_v0.fit, iso_p7v6source.txt*[1]
Energy range	$100 \,\mathrm{MeV} - 300 \,\mathrm{GeV}$
Time range	August 4th, 2008 – May 2nd, 2013
Zenith angle	$95°$
Source characteristics	point source at star's position
	or template from WISE data
	power law spectral shape
ROI	Circle; radius $15°$ and centre at star's position
Count cube	$20° \times 20°$ in RA and Dec, bin size $0.1°$,
	30 bins in energy
Input model	2FGL sources with distance ⩽ $17°$
Free parameters during fit	Normalisation of diffuse components
	2FGL sources with distance ⩽ $3°$

Table 4.1.: Parameters and models used in the pipeline analysis of the 27 bow shock candidates

Template Analysis

High-energy emission from bow shocks is expected to follow the infrared morphology, which is tracing the emission from the heated dust, since inverse Compton emission from the dust is the major contribution to high-energy photons. The above-mentioned characteristics of the *PSF* of the *Fermi*-LAT does not allow for the spatial resolution of most of the bow shock candidates. Therefore, the assumption of a point-like source at the position of the star is good, except for cases where the bow shock is too large or the distance from the shock to the star is too far. The point spread function of the *Fermi*-LAT decreases from $6°$ at $100 \,\mathrm{MeV}$ to $0.25°$ at $10 \,\mathrm{GeV}$. Two criteria are defined to decide on using the infrared emission as a spatial template for the *Fermi*-LAT analysis instead of a point source: if the arc length of the bow shock is larger than $0.3°$ or the distance between the star and the shock is larger than $0.1°$. The values for the bow shock morphology are taken from the E-BOSS catalogue. The bow shock size criterion leads to three bow shocks for which a template is used instead of a point source, namely HIP 22783, HIP 78401, and HIP 81377. The distance between star and bow shock adds HIP 97796 to the group of bow shocks analysed with a template.

The templates are created from publicly available(via `http://skyview.gsfc.nasa.gov`) WISE data with a wavelength of $22\,\mu$m. The WISE images are processed to dismiss all emission not originating from the bow shock. Regions immediately outside the bow shock are set to zero and bright stars are eliminated by setting all values above a certain threshold to zero as well. The templates are then normalised to be handled properly by the likelihood analysis. The results of the processing of HIP 22783 and HIP 78401 are shown in Figs. 4.2 and 4.3. The remaining two for ζ Ophiuchi and HIP 97796 are shown in Appendix B, Figs. B.1(a) and B.1(b).
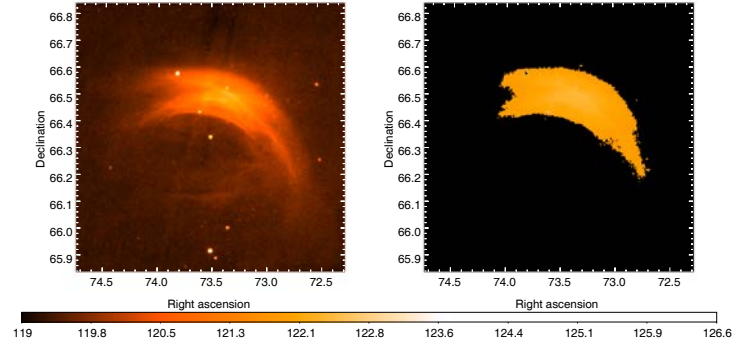
Figure 4.2.: WISE count map for HIP 22783 in $22\,\mu$m. The image on the left-hand side shows the publicly available data, the one on the right-hand side the corresponding template.
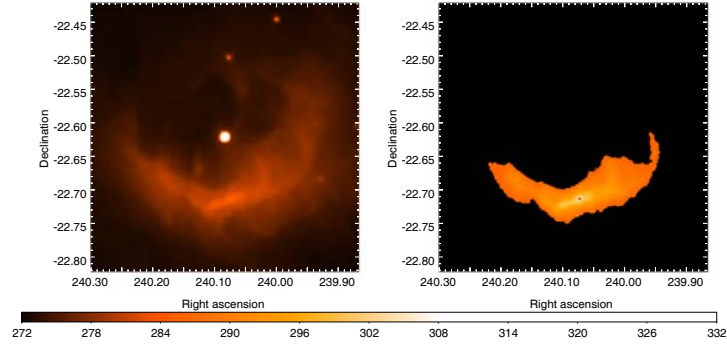
Figure 4.3.: WISE count map for HIP 78401 in $22\,\mu$m. The image on the left-hand side shows the publicly available data, the one on the right-hand side the corresponding template.

Validation of Fit Results

The result of the likelihood fit is a model describing the emission in the ROI. The input model including the diffuse emission and known sources is generated from 24 months of data. Since the analysis presented here is performed on 57 months of data, the fit results have to be validated. It is expected that fainter sources are newly detected in the larger data set and that the parameters of some known sources change. The diffuse models are also created with the two year data set only. Small discrepancies in the Galactic diffuse model can lead to large residuals, since the diffuse emission from the galaxy is very strong, The calculation of TS maps is a powerful method to localise possible excesses of photons.

Residual count maps

To validate the goodness of the fit, a model map is created for each fit result. This model map is a count map based on the fitted model assuming infinite statistics. An example for a count and model map is shown in Fig. 4.4 on the left-hand and right-hand side, respectively. The residual count map is calculated binwise from the count map and the model map. An entry R_{ij} in the residual count map is calculated as:

$$R_{ij} = \frac{M_{ij} - C_{ij}}{\sqrt{M_{ij}}} \tag{4.1}$$

where M_{ij} denotes the entry in the model map and C_{ij} the corresponding count map one.

An example for such a residual count map is shown in Fig. 4.5(a), the white crosses depict positions of 2FGL sources which are fixed during the fit, while blue crosses denote sources left free during the fit. The 2FGL is based on two years of data and does therefore not include all point sources visible in our data set.

The validation of the fit result is performed using the residual count map: if a bright residual is found at the position of a 2FGL source, an adjustment of the source parameters is performed in a subsequent likelihood fit. An example for such a case is BD+43°3654, the initial fit includes many 2FGL sources as can be seen by the number of crosses in the figure. At the position of 2FGL J2001.1–1141 a negative residual is clearly visible. This 2FGL source is associated with a BL Lac object and its flux is found to be varying in the Fermi All-sky Variability Analysis (Ackermann et al. 2013a, hereafter FAVA). Its spectral parameters are left free in a subsequent fit. The residual count map for this fit is shown on the right-hand side of Fig. 4.5(a). No bright residuals are visible, which is a good indication for a valid fit.

In the case of HIP 78401 a bright residual is found at a position where no 2FGL source was located, see left-hand side of Fig. 4.5(b). A source at this position, namely Fermi J1532-1319, was recently published by Ackermann et al. (2013a) and is included in the model
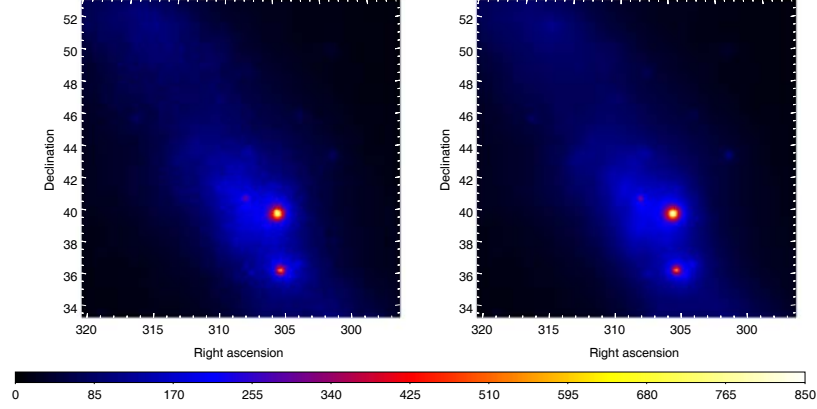
Figure 4.4.: Count and model map for BD+43°3654 on the left-hand side and right-hand side, respectively. The two very bright sources are two pulsars, namely 2FGL J2021.5+4026 (the upper and brighter one) and 2FGL J2021.0+3651 (the lower one). The galactic diffuse emission is visible as a diagonal band due to the coordinate system.

for a subsequent fit, the resulting residual map is shown on the right-hand side of the same figure and illustrates the good match of model and data.

The next step in the validation was the examination of the entry distributions in the residual count map. The entry distribution for HIP 78401 is shown in Fig. 4.6. If the model describes the data properly, a Gaussian distribution with a width $\sigma = 1$ and a mean $\mu = 0$ is expected. The fit results are shown in the title of the figure and depicted by the blue curve. The fit results of the two residual maps are very similar, although a bright source is missed in the first case, as shown above by the optical inspection of the residual map.

An indicator for the quality of the fit and potential sources are the minimum and maximum values, shown in the legend of the entry distributions. In the initial fit the minimum entry is -3.4 while the maximum was 8.1; after including the source the maximum entry decreased to 4.6 and the minimum stayed at -3.4. The probability values can be calculated for these entries. Including trial correction the p-values are $8.97 \cdot 10^{-12}$ and 0.081 for residual counts of 8.1 and 4.6, respectively. This confirms the need for adjustment in the first case and the proper modelling in the second case.

To ensure a proper inclusion of all sources in the ROIs, the residual maps are inspected visually, as described in the first part, and outliers in the statistical approach are looked at individually. The detailed information about all ROIs and corresponding 2FGL sources, which parameters were released, can be found in Table B.1.
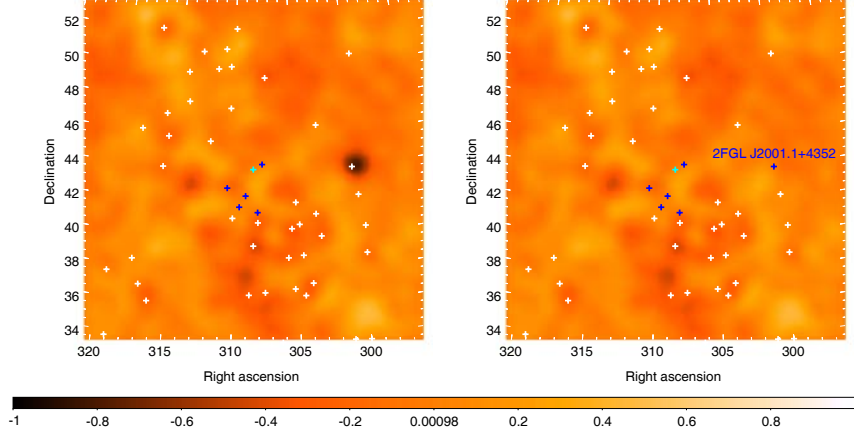
(a) For BD+43°3654: *Left-hand side*: fixed parameters for 2FGL J2001.1+4352. *Right-hand side*: parameters for 2FGL J2001.1+4352 freed.
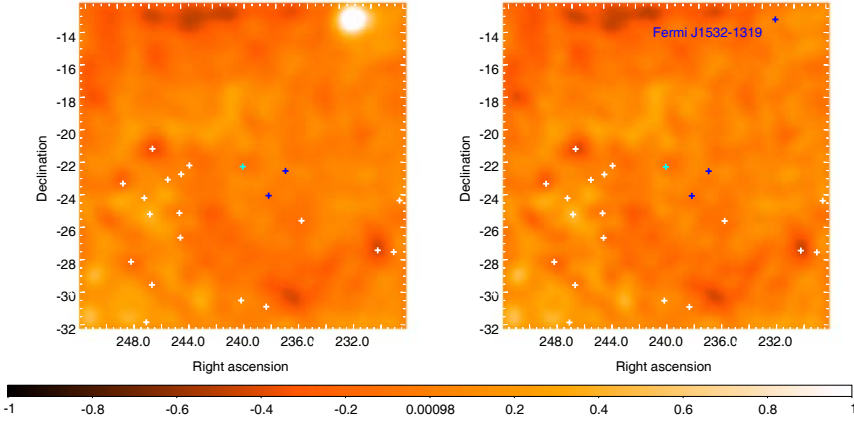
(b) For HIP 78401: *Left-hand side*: Fermi J1532-1319 not included. *Right-hand side*: Fermi J1532-1319 included in the model.

Figure 4.5.: Evolution of the residual count map during the validation process in the energy range from 100 MeV to 300 GeV on a 20° square around the respective source with a bin size of 0.1°. The maps have been smoothed with a Gaussian kernel of 1°. Blue crosses denote sources with free spectral parameters in the fit. White crosses denote positions of 2FGL sources with spectral parameters fixed to the catalogue values in the fit. The cyan cross depicts the position of the bow shock candidate.
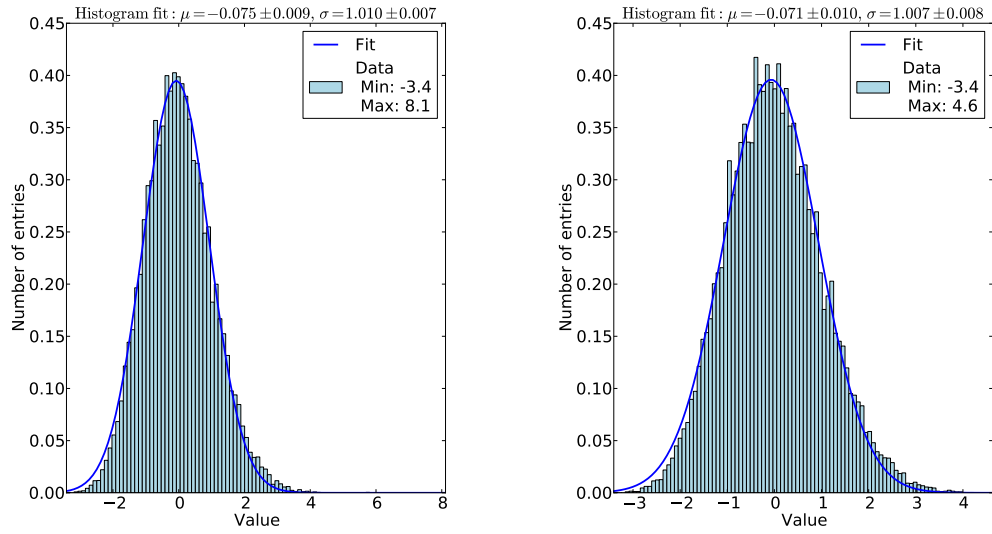
(a) The entry distribution for the residual map of HIP 78401, with no additional source; i.e. corresponding to the left-hand side of Fig. 4.5(b).

(b) The entry distribution for the residual map of HIP 78401, with an additional source; i.e. corresponding to the right-hand side of Fig. 4.5(b).

Figure 4.6.: The entry distributions for the residual maps of HIP 78401, corresponding to Fig. 4.5(b). The blue curve represents a fit to the data, the fit results are listed in the title of the figure. The minimum and maximum values of the distribution are listed in the legend.

TS maps

The next step in the analysis is the calculation of TS values, as outlined in Eq. 3.6, allowing for the determination of the significance of a source. To search for the origin of the emission, TS sky maps are created. They are calculated on a $0.1°$ grid in a $2°{\times}2°$ region around a potential source. For each bin a likelihood fit is performed with a model that has all parameters fixed to the fit results and an additional point source at the centre of the bin is introduced. This procedure is the same for sources analysed with a template and the point sources. The entries in the TS map are the respective TS values of the potential source. An example is shown in Fig. 4.7. The maps are used to localise the excess. If significant emission is present in the TS map at a position which is not compatible with a bow shock, an additional source is introduced in the model with a power law as a spectral shape at the point of highest TS. The minimal distance of the additional source to the bow shock was $0.5°$. In the analyses of the bow shock candidates, this occurred in three cases, namely HIP 32067, HIP 38430 and HIP 81377.

The TS map for HIP 38430 after introducing source A, which is not related to the bow shock, in the model is shown on the right-hand side of Fig. 4.7. The search for a multiwavelength counterpart for source A remained unsuccessful. The model in the 2FGL is based on two years of data. It is thus expected that dimmer sources are detected in an analysis like the one performed here. The model describing the galactic diffuse component is also based on two years of data, which might also lead to points of residual emission. The TS at the position of the bow shock decreased after the introduction of source A, which is expected due to the large PSF at low energies.

The second example is ζ Ophiuchi (HIP 81377), the TS map is shown in Fig. 4.8. The white contours depict the infrared emission, which is also used to model the *Fermi*-LAT emission. The centre of the emission is clearly offset from the bow shock, at a position where no gamma-ray source was detected so far. The multi-wavelength databases do not reveal a potential counterpart either. As mentioned above, the discovery of new sources is expected due to the larger dataset compared to the 2FGL.

The analysis of the third case, HIP 32067, followed the same principle and is outlined in detail in Section 4.4.
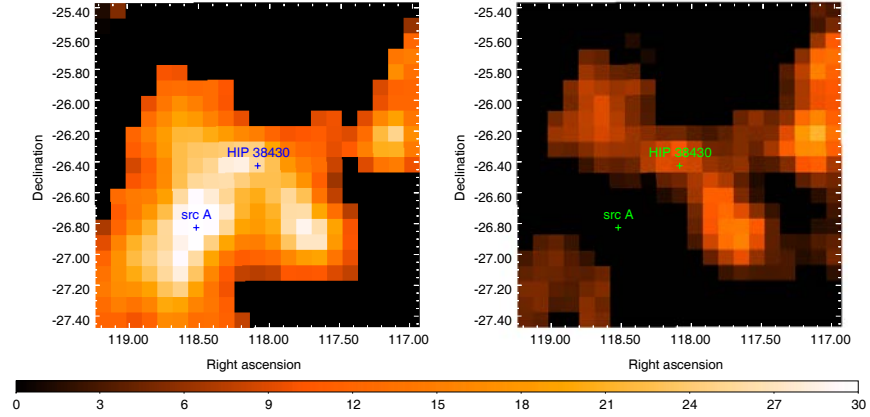
Figure 4.7.: TS map centred on the position of HIP 38430, on a square with a side-length of $2°$ and a bin size of $0.1°$. The blue (green) crosses indicate the positions of the bow shock and the additional source A on the left (right) map. On the left side, only 2FGL sources are included in the fitted model, in the right map the additional source A is also included. The colour scale is the same for both maps.
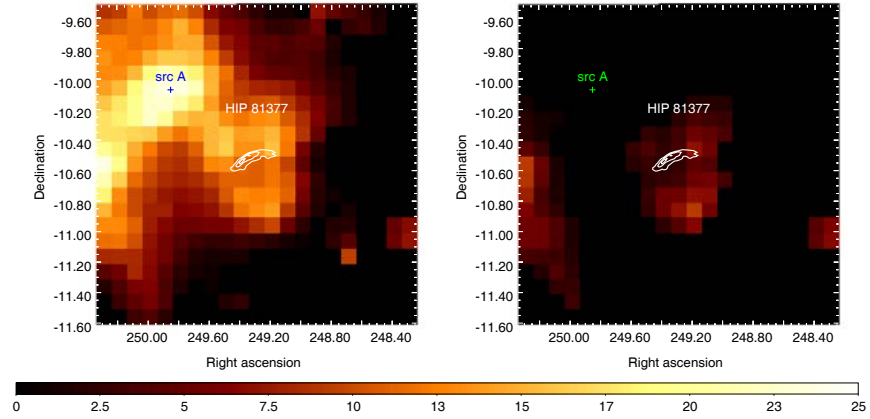
Figure 4.8.: TS map centred on the position of ζ Ophiuchi (HIP 81377), on a $2°$ square with a bin size of $0.1°$. The blue (green) cross indicates the position of the additional source A on the left (right) map. White contours show the bow shock of ζ Ophiuchi observed in infrared at $22\,\mu$m by WISE. On the left side, only 2FGL sources are included in the fitted model, in the right map the additional source A is also included. The colour scale is the same for both maps.

Values of diffuse components

The normalisations of the galactic and isotropic diffuse components are left free to vary during the fit. The fit values are expected to be around 1 for both components. The distribution of the normalisations of all fits can thus be used as an additional validation of the fit results, complementing the checks performed on the residual count and TS maps. The distribution of the normalisations for the Galactic diffuse is shown in Fig. 4.9(a). The values cluster around 1, the average being close to 1.1. These values are reasonable since the ROIs are all located in the galactic plane, where the emission is very bright. The diffuse models are prepared for the 2FGL and are thus not sufficient to describe all features in the 57 months data set.

The distribution of the isotropic normalisation is shown in Fig. 4.9(b). The values have a larger spread but also cluster around 1. The contribution from the galactic component is much higher in the galactic plane. The combination of both distributions, the galactic slightly above 1 and the isotropic slightly below, confirms the goodness of the fits.
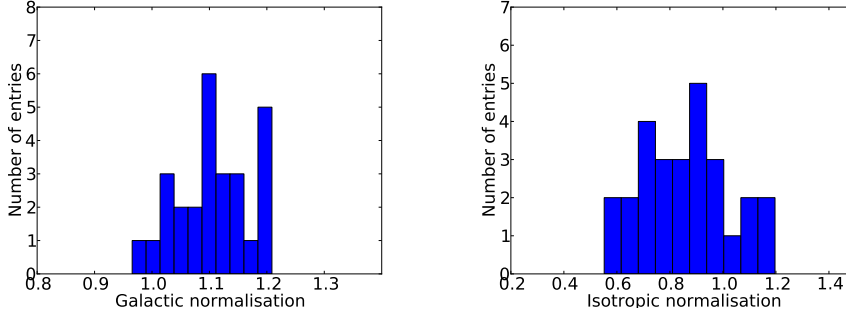
Figure 4.9.: Distribution of the galactic and isotropic normalisation values of all performed fits for the pipeline analysis.

Distribution of TS values

The distribution of the TS values is shown in Fig. 4.10, the expectation for background is shown in red. The maximum TS value in this distribution is 9.3. A TS value of 9.3 has a probability of 0.0022, assuming a χ^2 distribution. Including the correction for trials a probability of 0.6 can be calculated. The results are compatible with background only.
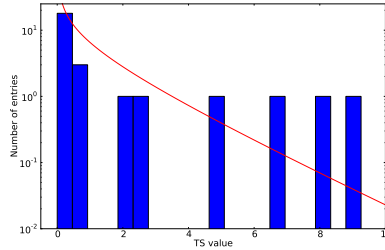
Figure 4.10.: The blue histogram shows the distribution of TS values for the 27 bow shock candidates in the pipeline analysis. The red line depicts the expected distribution for background.

4.2. Serendipitous Discovery of HE Emission from an SNR

During the analysis of the region around HIP 32067 a serendipitous discovery was made. The analysis procedure was the same as for the other sources in the pipeline, but the initial fit, including 2FGL sources only, gave a TS for the bow shock candidate of $\sim$60. The search for possible sources in the ROI led to a gamma-ray transient, published by Cheung et al. (2012a). This transient was later associated with the Nova Mon 2012 (Cheung et al. 2012b). A nova is an thermonuclear explosion on the surface of a white dwarf, that is located in a binary system and accretes matter from its companion. The accumulated matter on the surface of the star starts nuclear fusion once the temperature and pressure are high enough. The white dwarf is not destroyed and returns to its original brightness after the explosion. Recurrent novae are observed if the accretion continues.

The light curve, e.g., counts per second and cm^2 as a function of mission elapsed time (MET), for the region around HIP 32067 is shown in Fig. 4.11. The time when the nova occurred is depicted by the vertical dashed line. The transient event is clearly visible. In order to not confuse potential sources with the transient, further searches are performed on a data set with a restricted time range, e.g., before the nova occurred.

From the calculated TS map, shown in Fig. 4.12, it is clearly visible that the remaining emission does neither originate from the nova nor the bow shock, but from a region outside
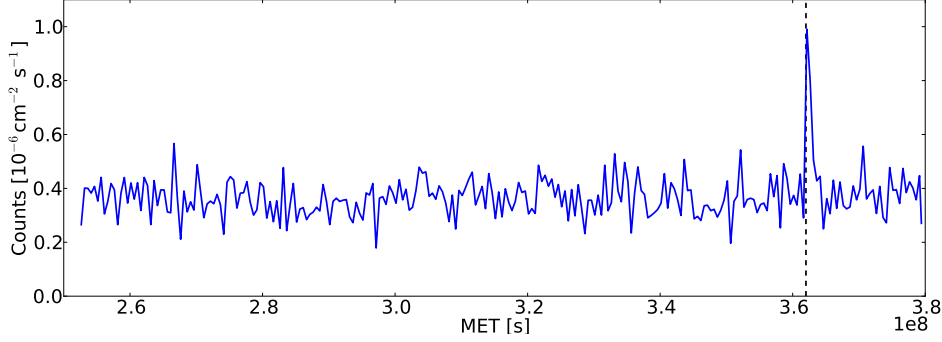
Figure 4.11.: Counts per second and cm^2 from a circular region around HIP 32067 with a diameter of 1° as a function of mission elapsed time (MET), the vertical dashed line depicts the time of the nova.

the usual 2° size of the TS map. Thus a TS map covering 5×5° was calculated, the result is shown in Fig. 4.12 for two energy cuts. The left map shows the TS map for events above 100 MeV, on the right-hand side the energy cut was set to 500 MeV. The higher energy cut results in a better PSF and therefore a potentially better source localisation. The two maps confirm that the emission does not originate in the bow shock but from an offset source. The point of highest TS ($\sim$80) is at RA(J2000)= 102.01°, DEC(J2000)= 6.83°. After introducing an additional source A at this position, a subsequent fit reveals a second source of high emission at the position RA(J2000)= 100.74°, DEC(J2000)= 5.35°.

The multi-wavelength counterpart search resulted in two SNRs, namely G205.5+0.5 and G206.9+2.3. The former is the so-called Monoceros Loop with a size of 220′ (Green 2009). In the 2FGL three sources (2FGL J0631.6+0640, 2FGL J0636.0+0554, and 2FGL J0637.8+0737) lie within this large structure. G206.9+2.3 is not yet associated to a HE source. The contours in Fig. 4.12 are created from publicly available data[2] of the Sino-German 6 cm survey (Gao et al. 2010).

The supernova remnant G206.9+2.3, also called PKS 0646+06, is detected in radio (Graham et al. 1982), optical (Davies & Meaburn 1978) and X-rays (Leahy 1986). It is $\sim$4 kyr old and at a distance of $\sim$8 kpc (Leahy 1986). The radio emission is spatially coincident with the *Fermi*-LAT source that is detected with a TS of $\sim$90. The spectrum of the source is shown in Fig. 4.13, the spectral points are calculated in six energy bins, logarithmically evenly spaced between 100 MeV and 300 GeV. The two curves depict fits to the data, the green one of a power law and the red one of a

---

[2]`http://zmtt.bao.ac.cn/6cm/surveydata.html`
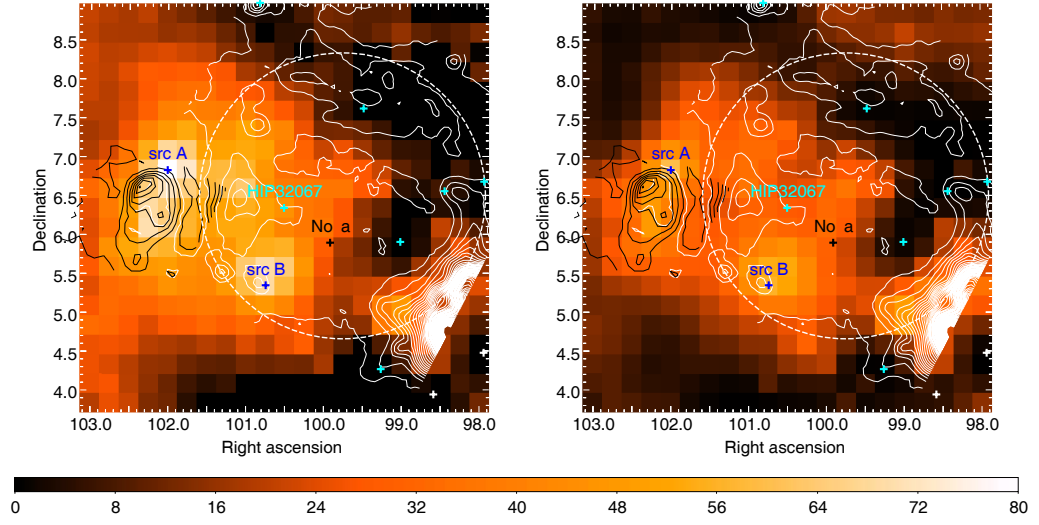
Figure 4.12.: TS map centred on the position of HIP 32067, on a $5°$ square with a bin size of $0.25°$. The blue crosses indicate the positions of the additional sources A and B. White (black) contours depict the radio emission from G205.5+0.5 (G206.9+2.3). The dashed circle indicates the size of G205.5+0.5 in radio. The position of the Nova is depicted with a black cross. Cyan (white) crosses depict 2FGL sources with parameters free (fixed) during the fit. On the left-hand side the lower energy threshold is $100\,\text{MeV}$, on the right-hand side it is $500\,\text{MeV}$.

logParabola. The significance of the curvature of the spectrum is determined with the formula: $\text{TS}_{\text{curve}} = 2(\mathcal{L}(\text{logParabola}) - \mathcal{L}(\text{PowerLaw}))$ (following Nolan et al. 2012). The spectral models are nested and the logParabola function has one additional parameter, the distribution of the TS_{curve} should therefore follow a χ^2 distribution with one degree of freedom. The spectral fit of the additional source results in $\text{TS}_{\text{curve}} = 15.4$, which translates into a significance of 3.9σ. The spectral parameters for the power law are: $N_0 = (5.0 \pm 0.3)10^{-10}\,\text{cm}^{-2}\,\text{s}^{-1}\text{MeV}^{-1}$ and $\gamma = -2.53 \pm 0.02$ with $E_0 = 100\,\text{MeV}$. For the logParabola: $N_0 = (3.5 \pm 0.2)10^{-11}\,\text{cm}^{-2}\text{s}^{-1}\text{MeV}^{-1}$, $\alpha = 1.82 \pm 0.03$, $\beta = 0.38, \pm 0.02$ and $E_b = 300\,\text{MeV}$. The spectrum is consistent with the expectations for an SNR with that age and distance.

The analysis of the Monoceros Loop in the high-energy regime is beyond the scope of this work. A dedicated study on the shape of the high-energy emission and whether source B is part of a large-scale emission is not relevant for the analysis of the bow shocks of runaway stars.
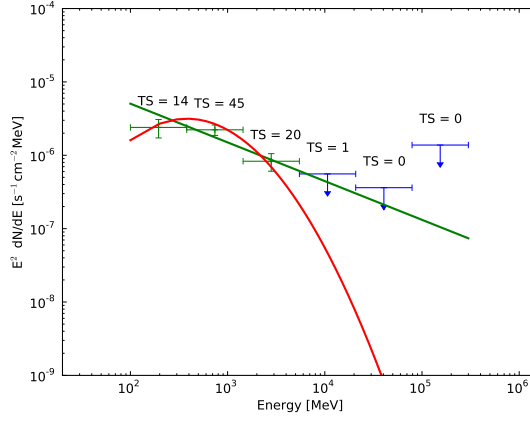
Figure 4.13.: The spectral points of the additional source A, potentially the SNR G206.9+2.3, together with a power law and a logParabola fit shown in green and red, respectively.

After introducing the two additional sources in the model, both not associated to the bow shock, the next steps in the analysis are again performed on the entire data set. The TS value for the bow shock is 8, which means that no significant emission is detected. The further analysis is performed in the pipeline together with the other candidates.

4.3. Analyses with Varying Energy Thresholds

The analyses of the bow shocks are performed with different cuts on the lower energy bound. The *PSF* of the *Fermi*-LAT depends strongly on energy. A higher energy cut results in a much better angular resolution, but the effective area and the flux of photons decrease with energy. A cut in energy has to balance between optimal angular resolution and sufficient photon statistics. The TS values for three different energy cuts are shown in Fig. 4.14. The energy cuts applied are 100 MeV, 500 MeV and 1 GeV. None of the bow shocks is detected significantly in any of the cut configurations. Three sources show a variation in the TS values, namely HIP 32067, HIP 38430 and HIP 81377, these are the ones where additional sources were included in the model based on the TS maps, as described above. The differences in the TS values can partly be attributed to the close-by sources.
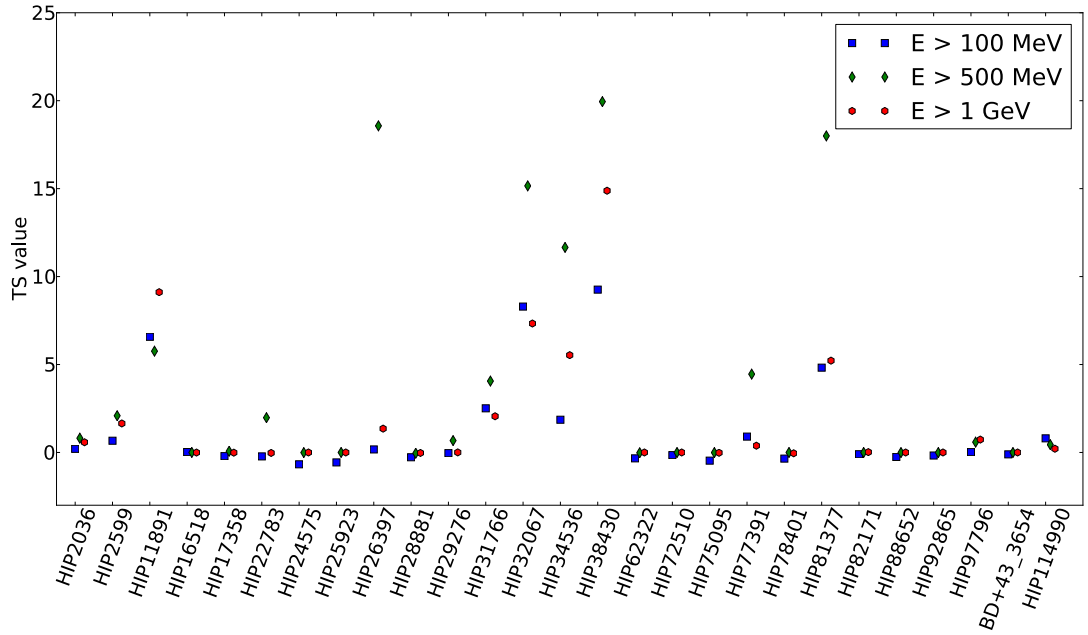
Figure 4.14.: TS values for the pipeline analysis for different minimum energies.

4.4. Dedicated Analysis of HIP 101186 (Fermi-LAT)

HIP 101186 is not included in the pipeline analysis. Instead, a dedicated analysis is performed. This source was suggested to be the first bow shock detected in high-energy gamma rays by del Valle et al. (2012) due to a spatially coincident Fermi source, but the *Fermi*-LAT source is associated with a gamma-ray pulsar, see Chapter 2 for details. In Fig. 4.15 the WISE count map in $22\,\mu\mathrm{m}^3$ is shown, overlaid are the positions of the relevant sources. The cyan arrow points to the position of the star (HIP 101186). The white circle depicts the 95% positional uncertainty of the source 2FGL J2030.7+4417 and the green cross depicts the position of the pulsar. The positional errors for the pulsar are on much smaller scales, the statistical error in Pletsch et al. (2012) is given as $0.04''$. On the right-hand side the template created to perform the *Fermi*-LAT analysis is shown.
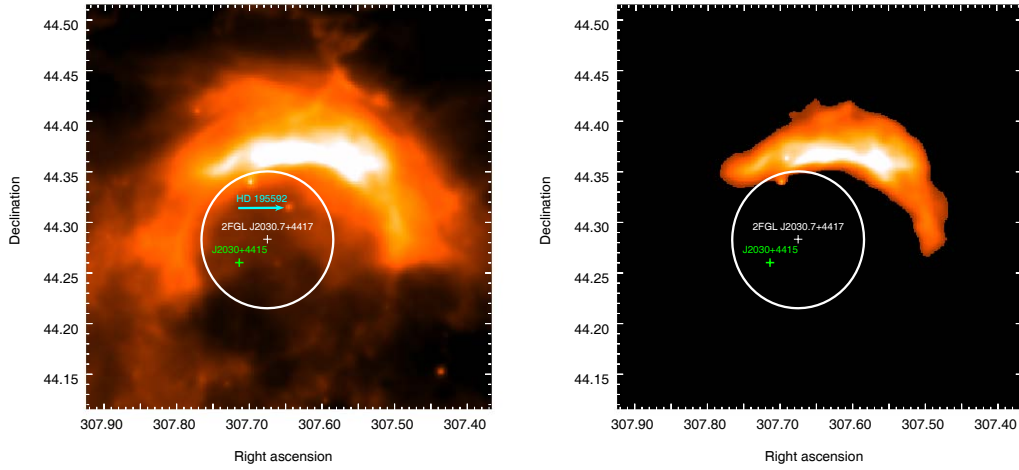
Figure 4.15.: WISE count map of HIP 101186 in $22\,\mu\mathrm{m}$, including the positions of 2FGL J2030.7+4417 and PSR J2030+4415 in white and green, respectively. The white circle represents the 95% positional uncertainty of the 2FGL source. The cyan arrow points to the position of the runaway star HD 195592, visible in infrared as well. On the left-hand side the original image is shown, on the right-hand side the template used for the *Fermi*-LAT analysis.

In this case the emission from the pulsar has to be disentangled from potential emission from the bow shock. In the second pulsar catalogue (Abdo et al. 2013) PSR J2030+4415 is listed as a pulsar with no significant off-pulse emission. The phasogram shows two clear peaks and the off-pulse phase region is calculated as ranging from phase 0.65–0.01.

---

[3] obtained via `http://skyview.gsfc.nasa.gov`

The phasogram of a circular region with a radius of $0.5°$ around the position of HIP 101186 is shown in Fig. 4.16 together with the published one. The vertical dashed lines are at phases 0.65 and 1, which denote the off-pulse phase of this pulsar as calculated in Abdo et al. (2013).
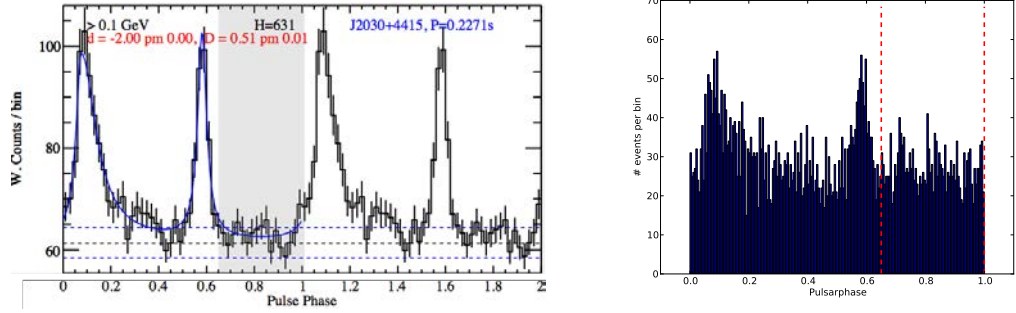
(a) Phasogram of PSR J2030+4415 as published in the 2PC. For clarity two rotation periods are shown. Figure credit: Abdo et al. (2013).

(b) Phasogram from a circular area with radius $0.5°$ around the position of the star. The vertical dashed lines are at phases 0.65 and 1.

Figure 4.16.: Phasogram of PSR J2030+4415 as published on the left-hand side and obtained from our analysis on the right-hand side.

To disentangle emission from the pulsar and the potential bow shock emission two approaches are pursued: version A is to analyse only data which is in the off-pulse phase of the pulsar. Version B is to include the pulsar as a source in the model using the spectral and spatial values published in the 2PC and perform the analysis with the new model. The advantage of version A is that the data set does not include photons from the pulsar since there is no off-pulse emission detected from the pulsar. The disadvantage is that the assignment of pulsar phases to the *Fermi*-LAT data requires an ephemeris for the according time period. The ephemeris describes the temporal evolution of the pulsar, i.e. the pulse phase at a specific point in time, the pulse frequency and its first and second time derivative at the same point in time. The 2PC published ephemeris for all listed pulsars, but only for three years of observations. Thus, version A is limited to a time interval of three years. Version B does not have this drawback, but assumes that the pulsar does not change its spectral parameters during time. Both analysis are performed and give consistent results.

For the off-pulse analysis an intermediate step is needed in the analysis. The tempo2[4] pulsar timing package with the *Fermi* plugin is used to assign pulse phases to each photon after the usual event selection. Then an additional event selection based on the off-pulse

---

[4] http://www.atnf.csiro.au/research/pulsar/ppta/tempo2/

definition from the 2PC, see Fig. 4.16, is performed, i.e. only events with pulsar phases between 0.65 and 1 are kept. The remaining steps in the analysis are the same as for the analyses described above. The models of the other sources have to be scaled by the fraction of selected off-pulse time.

The bow shock has a length of 19 arcmin, which might be resolved with the *Fermi*-LAT. Thus a template, created from infrared data and shown in Fig. 4.15 on the right-hand side, is used to model the spatial distribution of the potential source.
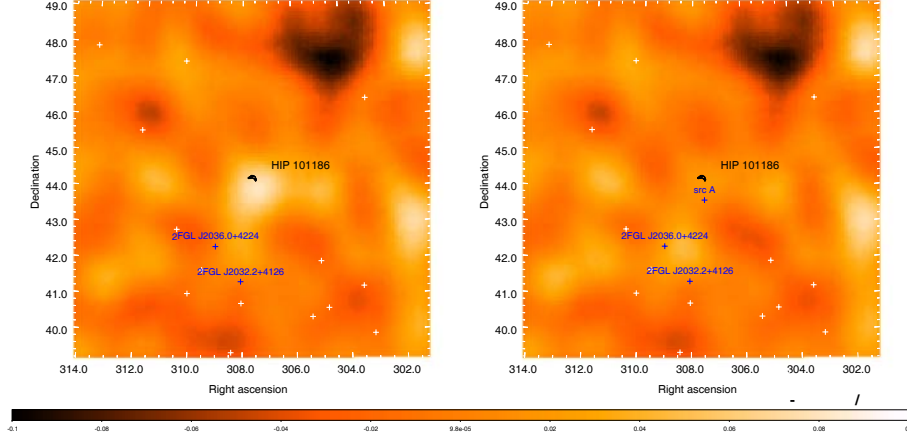
Figure 4.17.: Residual count map in the energy range between 100 MeV and 300 GeV around HIP 101186. The size is $20 \times 20°$ and the binsize is $0.1°$, the map is smoothed with a gaussian kernel of $1°$. White (blue) crosses denote 2FGL sources which are held fixed (free) during the fit. The black contour shows the WISE ($22\,\mu$m) emission. On the left-hand side only 2FGL sources are present in the model, while for the right-hand side an additional source is included.

In the residual count map, shown in Fig. 4.17 on the left-hand side, enhanced emission is visible in the region south of the bow shock, depicted with black contours. The TS value for the bow shock template is 15 in this fit. Fig. 4.18 shows the TS map, which reveals a source with a TS of ∼30. This source is neither at the position of the pulsar, depicted with a cyan cross in the figure, nor the bow shock, depicted with the black contours. A new source is therefore introduced at the position RA(J2000)= 307.51°, DEC(J2000)= 43.71°. In the subsequent fit the bow shock achieves a TS value of 0, compatible with background. This is also visible in the TS map for this subsequent fit that is shown on the right-hand side of Fig. 4.18.

All examined bow shock candidates give TS values smaller than 10. This means that high-energy emission from a bow shock of a runaway star remains yet to be discovered.
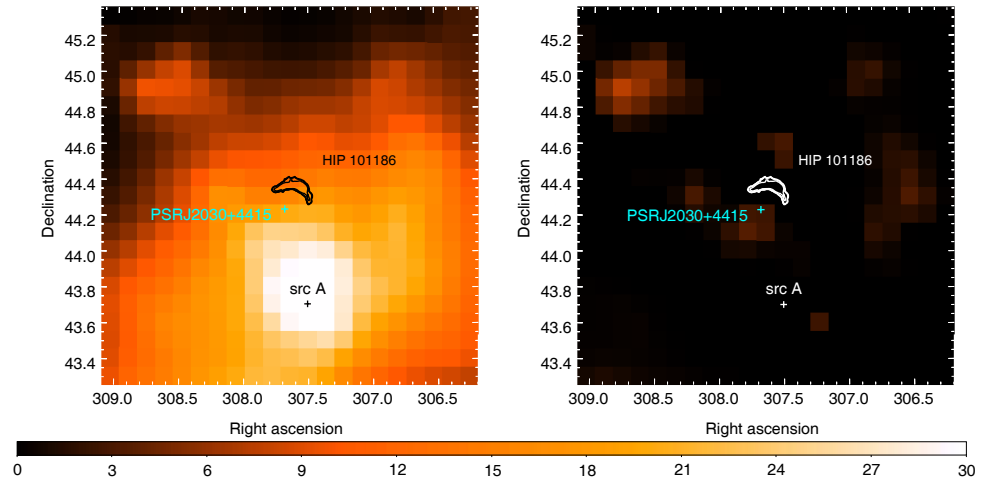
Figure 4.18.: TS map of a $2 \times 2^\circ$ region around HIP 101186. The bins in RA and Dec have a size of 0.1°. The black contours show the $22\,\mu m$ WISE emission from the bow shock of HIP 101186, the cyan cross depicts the position of the pulsar PSR J2030+4415. The black cross depicts the position with the highest TS where an additional source is introduced.

From the non-detection it is possible to calculate upper limits on the flux of the potential sources. This is described in detail in the following section.

4.5. Fermi-LAT Upper Limits

Since there is no significant HE emission from bow shocks of runaway stars we calculate
upper limits on the energy flux, following Helene (1983), in four energy bins, logarithmi-
cally equally spaced between 100 MeV and 300 GeV. The spectrum in each bin is assumed
as a power law with a spectral index of 2. The upper limits for all sources are shown in
Tab. 4.2 and visualised in Fig. 4.19.
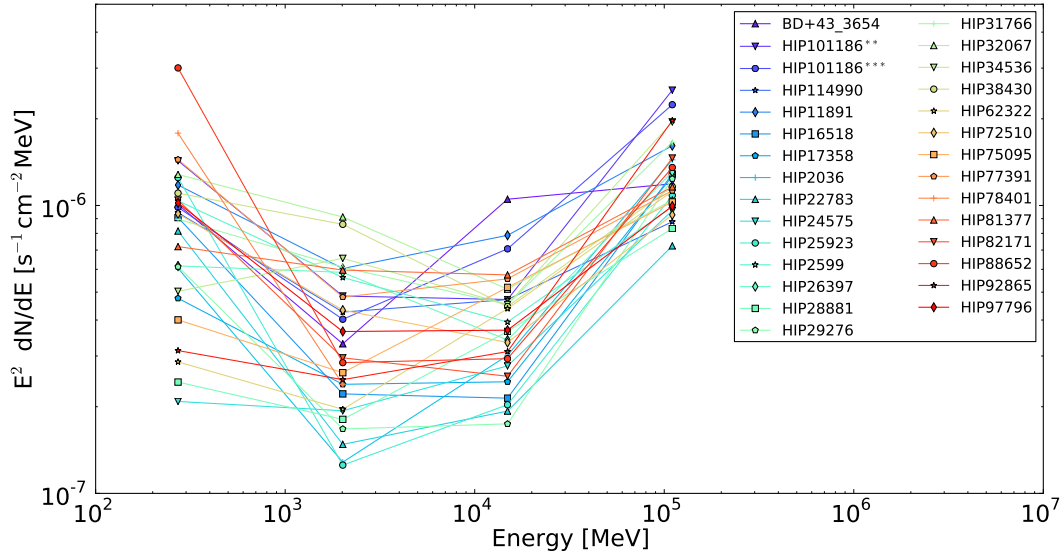
Figure 4.19.: Upper limits calculated using *Fermi*-LAT data of 28 bow shock candidates.
The ** denotes the off-pulse analysis, *** with the pulsar included in the model. The
values of the upper limits in each bin are also presented in Tab. 4.2.

Star	l	b	TS	UL $\epsilon_\gamma F(\epsilon_\gamma)$ $[10^{-6}\,\mathrm{MeV\,cm^{-2}\,s^{-1}}]$			
	[°]	[°]		$0.1 - 0.74$ [GeV]	$0.74 - 5.5$ [GeV]	$5.5 - 41$ [GeV]	$41 - 300$ [GeV]
HIP 2036	120.9137	+09.0357	0.2	0.61	0.13	0.30	1.44
HIP 2599	120.8361	+00.1351	0.6	0.99	0.55	0.39	0.99
HIP 11891	134.7692	+01.0144	6.6	1.20	0.60	0.79	1.61
HIP 16518	156.3159	−16.7535	0.1	0.93	0.22	0.21	1.29
HIP 17358	150.2834	−05.7684	0	0.56	0.24	0.24	1.26
HIP 22783*	144.0656	+14.0424	0	0.82	0.15	0.19	0.72
HIP 24575	172.0813	−02.2592	0	0.21	0.19	0.28	0.96
HIP 25923	210.4356	−20.9830	0	1.31	0.13	0.20	1.08
HIP 26397	174.0618	+01.5808	0.2	0.64	0.59	0.34	1.31
HIP 28881	164.9727	+12.8935	0	0.24	0.18	0.37	0.83
HIP 29276	263.3029	−27.6837	0	0.70	0.17	0.17	1.24
HIP 31766	210.0349	−02.1105	2.5	0.90	0.61	0.45	1.66
HIP 32067	206.2096	+00.7982	8.3	1.28	0.91	0.51	1.04
HIP 34536	224.1685	−00.7784	1.9	0.51	0.65	0.45	1.95
HIP 38430	243.1553	+00.3630	9.3	1.10	0.86	0.45	1.16
HIP 62322	302.4492	−05.2412	0	0.32	0.19	0.44	1.12
HIP 72510	318.7681	+02.7685	0	0.94	0.43	0.33	0.93
HIP 75095	322.6802	+00.9060	0	0.40	0.26	0.52	1.03
HIP 77391	330.4212	+04.5928	0.9	1.44	0.48	0.56	1.13
HIP 78401*	350.0969	+22.4904	0	0.57	0.15	0.34	1.06
HIP 81377*	006.2812	+23.5877	4.8	0.72	0.60	0.57	1.16
HIP 82171	329.9790	−08.4736	0	1.04	0.30	0.26	1.46
HIP 88652	015.1187	+03.3349	0	3.00	0.28	0.29	1.35
HIP 92865	041.7070	+03.3784	0	0.31	0.25	0.31	1.97
HIP 97796*	056.4824	−04.3314	0.1	1.02	0.36	0.37	1.00
HIP 101186**	082.3557	+02.9571	0	1.43	0.48	0.47	2.52
HIP 101186***	082.3557	+02.9571	0.7	0.99	0.40	0.71	2.24
BD+43°3654	082.4100	+02.3254	0	1.00	0.33	1.05	1.19
HIP 114990	112.8862	+03.0998	0.8	0.94	0.43	0.47	0.88

Table 4.2.: 95% confidence-level, gamma-ray flux upper limits for bow shocks of runaway stars. For the 4 bow shocks indicated with stars, the limits were calculated for spatial emission profiles obtained from the WISE infrared emission intensity; for the remaining 23 bow shocks the limits were calculated for a point-like source at the position of the runaway star; see text for details. All bow shock candidates are listed in the E-BOSS catalogue. l and b denote the Galactic coordinates of the star. $\epsilon_\gamma F(\epsilon_\gamma)$ corresponds to the integral energy flux upper limit within the energy range provided (GeV) assuming a power-law spectrum of gamma-ray emission with photon index $\alpha=2$ within this energy band. ** denotes the off-pulse analysis, *** with the pulsar included in the model.

4.6. H.E.S.S. Analyses

In the VHE domain, data is unfortunately not available for all bow shock candidates. H.E.S.S. is not scanning the entire sky but performs dedicated observations on individual sources. The inner Galactic plane has been scanned by H.E.S.S. starting in 2004 (Aharonian et al. 2005) and the scan has continued in the following years (the most recent results are outlined in: H.E.S.S. collaboration in prep.). Since the telescopes are located on earth, it is not possible to observe all parts of the sky during night-time. Due to the small field of view and the limited observation time of about 1000 hours per year, only small parts of the sky have been looked at with H.E.S.S.

Checking the archival data led to a sample of seven bow shock candidates which have been observed with H.E.S.S. These bow shock candidates are marked with green crosses in Figure 4.1. The star, its position and the amount of runs, specifying a 28 minute observation period, on the sources are shown in Tab. 4.3.

A model analysis with standard cuts as described in Chapter 3 is performed on all seven candidates. The extensions of the bow shocks in infrared are all smaller than 2.5 arcminutes ($\simeq 0.04°$). This is slightly less than the PSF of the H.E.S.S. experiment. Therefore a point source analysis is the most sensitive way to establish a detection. The sources are thus assumed as point sources at the position of the respective star. The reflected region background methods is applied and the number of on and off events are used to calculate the significance (σ) of the source following Li & Ma (1983). The results of the analyses are summarised in Table 4.4 in the fourth column.

Star	l [°]	b [°]	Number of runs	mean θ [°]	mean offset [°]
HIP 25923	210.4356	−20.9830	21	25	1.8
HIP 32067	206.2096	+00.7982	87	35	1.9
HIP 38430	243.1553	+00.3630	9	8	2.4
HIP 72510	318.7681	+02.7685	31	35	2.1
HIP 75095*	322.6802	+00.9060	98	38	1.6
HIP 88652*	015.1187	+03.3349	21	17	1.9
HIP 92865*	041.7070	+03.3784	12	37	1.4

Table 4.3.: Overview about bow shocks with H.E.S.S. exposure of the bow shock candidates from the E-BOSS catalogue. θ denotes the zenith angle. Sources labelled with a * are in the range of the H.E.S.S. galactic plane scan.

The Θ^2 distribution for HIP 75095 is shown in Fig. 4.20 as an example. The number of events as a function of squared angular distance from the source position are shown for the source region as filled histogram and for the background region as black crosses. The distribution of the counts in the source region is constant, as is expected for an isotropic background, and compatible with the distribution from the background region.
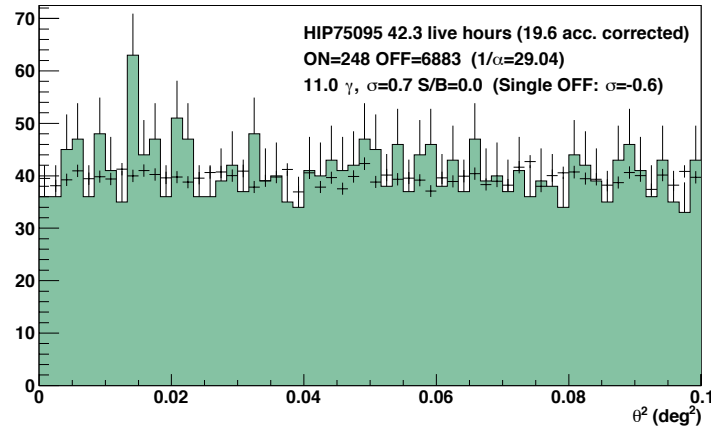
Figure 4.20.: Θ^2 distribution, i.e. the number of events as a function of squared angular distance, around HIP 75095. The filled histogram shows the distribution for the source region and the black crosses the one of the background region. The statistics of the analysis as the number of events in ON and OFF region, and the significance σ are also presented.

Fig. 4.21 shows the significance distributions for two of the bow shocks. If only background is present in the region analysed, the distribution of significances is expected to follow a Gaussian distribution with a sigma of 1 and a mean of 0. The fit results are displayed in the figure and show clearly that no sources are detected.

In the model analysis framework a dedicated set of cuts for faint sources is implemented, as outlined in Section 3.2. The analyses performed with faint cuts do not reveal significant emission either. The upper limits are less constraining due to the higher signal to background ratio.
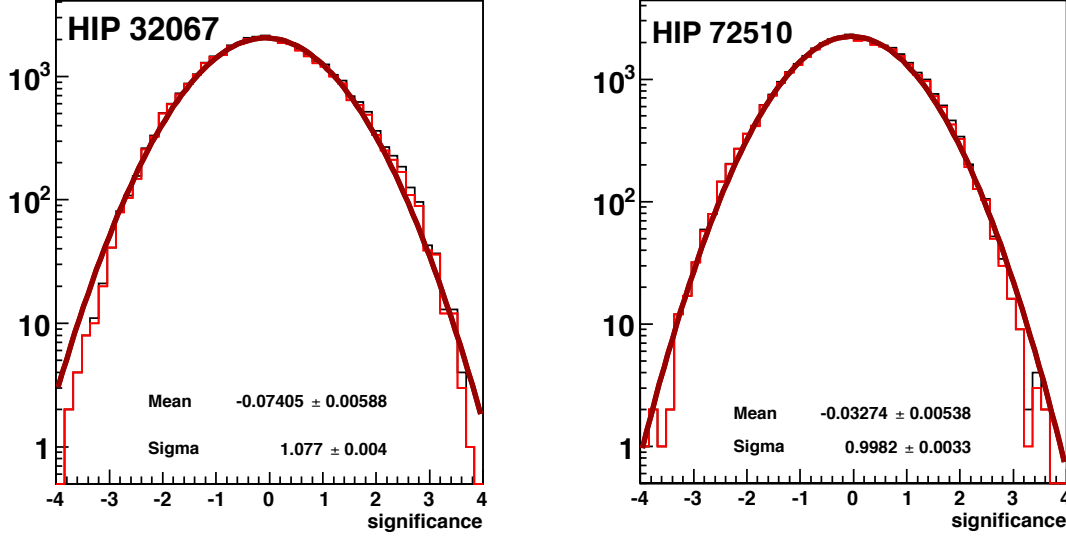
(a) Significance distribution for HIP 32067.

(b) Significance distribution for HIP 72510.

Figure 4.21.: Significance distribution for two of the bow shocks, HIP 32067 and HIP 72510.

For the three sources inside the H.E.S.S. Galactic plane scan region a cross-check with an independent calibration and analysis chain has been performed. The H.E.S.S. collaboration is working on the publication of maps from the Galactic plane scan (H.E.S.S. collaboration in prep.). This allows for an independent calculation of upper limits in regions where no significant emission is found. The upper limits from this analysis are calculated as integral upper limits above 1 TeV, the results are consistent with the ones presented here.

4.7. H.E.S.S. Upper Limits

Upper limits are calculated in energy bins, equally spaced in logarithmic energy, following Feldman & Cousins (1998). The results presented here are obtained with standard cuts. The spectrum is assumed to follow a power law shape with index of 2 in each energy bin. The results of the upper limit calculation are shown in Tab. 4.4. The energy threshold for H.E.S.S. depends on the observation conditions, especially the zenith and offset angles. This leads to higher energy thresholds in the cases of HIP 38430, HIP 72510, and HIP 92865. A comparison of the upper limits and the predicted SEDs is presented in the next chapter.

Star	σ	UL $\epsilon_\gamma F(\epsilon_\gamma)$ $[10^{-12}\,\mathrm{TeV\,cm^{-2}\,s^{-1}}]$				
		$0.37 - 0.97$	$0.97 - 2.57$	$2.57 - 6.78$	$6.78 - 17.92$	$17.92 - 47.33$
HIP 25923	1.2	0.96	0.30	0.32	1.21	6.84
HIP 32067	-0.6	0.41	0.08	0.63	0.44	0.80
HIP 38430	0.1	-	0.39	1.91	1.12	3.53
HIP 72510	0.3	-	0.28	0.74	1.58	1.77
HIP 75095	0.7	0.60	0.19	0.24	0.34	1.57
HIP 88652	0.9	0.65	0.56	1.17	0.91	3.63
HIP 92865	-0.8	-	0.48	0.32	0.90	0.84

Table 4.4.: 99% confidence-level, gamma-ray flux upper limits for bow shocks of runaway stars obtained with H.E.S.S.. The significance σ of a source detection is given in the second column.

5. Constraining the Gamma-Ray Emission of Bow Shocks of Runaway Stars

5.1. Comparison of Upper Limits to Model Predictions

Model predictions for the HE and VHE emission have been published for four of the bow shocks listed in the E-BOSS catalogue: ζ Ophiuchi (HIP 81377), HIP 101186, BD+43°3654, and AE Aurigae (HIP 24575). The publications on these sources are outlined in detail in section 2.5. None of these published bow shock candidates exhibits H.E.S.S. exposure. In this section the published predictions are thus compared to the *Fermi*-LAT upper limits calculated in this work. The spectral energy distributions (SEDs) of the individual objects are discussed in the first part, followed by a comparison of the different model predictions to the upper limits from the entire sample observed with H.E.S.S.

5.1.1. ζ Ophiuchi (HIP 81377)

ζ Ophiuchi is the best candidate for HE and VHE emission as pointed out by del Valle & Romero (2012). The comparison of the upper limits and the model predictions, published by del Valle & Romero (2012) are shown in Figure 5.1. The VLA upper limits are taken from the VLA survey (Condon et al. 1998). The theoretical upper limits in the X-ray regime are obtained from Hasinger et al. (2001).

The upper limits obtained here are a factor of $\sim$5 lower than the predicted emission. This constrains some of the assumptions in this model. Either particle acceleration is not efficient enough to produce photons with these energies or the magnetic fields are lower than expected. The subequipartition factor χ between kinetic and magnetic energy density is assumed to be 10 %. In Eqn. 2.4 the factor is used to estimate the magnetic field. A wrong estimation of χ would lead to a wrong estimation of the magnetic field.
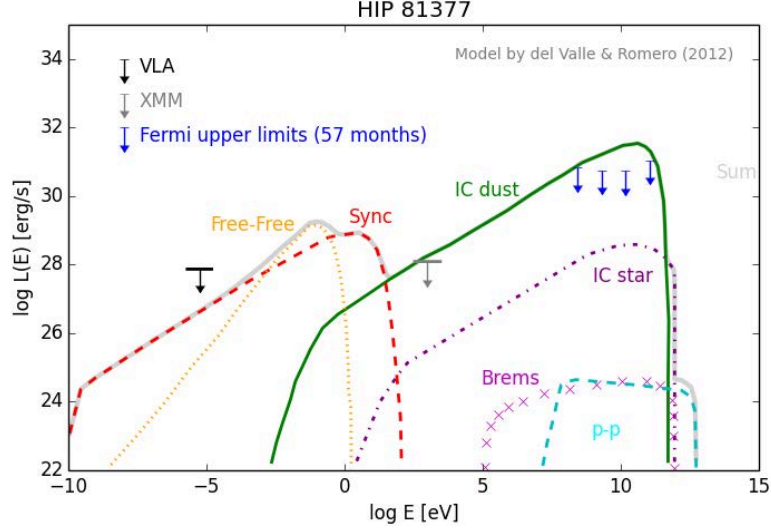
Figure 5.1.: Upper limits of HIP 81377 obtained with VLA, XMM and *Fermi*-LAT data, compared to model predictions by del Valle & Romero (2012).

An additional input parameter in the model is the fraction of kinetic energy which is transformed into the acceleration of particles, q_{rel} introduced in Eqn. 2.6. This might be lower than 10 % as assumed by del Valle & Romero (2012). The fraction of leptonic and hadronic power, a, might be different than 1 as assumed for the calculation of the SED prediction presented in Fig. 5.1.

There are no observations of non-thermal emission in any energy regime. Upper limits are found from radio to gamma rays, constraining the level of the possible non-thermal emission over a broad energy range.

5.1.2. HD 195592 (HIP 101186)

The first possible detection of high-energy emission from a bow shock of a runaway star was published by del Valle et al. (2012), who related the *Fermi*-LAT source 2FGL J2030.7+4415 to the bow shock of HD 195592 (HIP 101186). This source is a gamma-ray pulsar and thus not connected to the bow shock as pointed out earlier.

The model calculation by del Valle et al. (2012) are shown in Figure 5.2 together with the upper limits obtained with *Fermi* with the pulsar included in the model. The data from VLA and IRAS are of thermal origin. The model does not include thermal processes, it is thus not expected to match this measurements. This is the second case where the
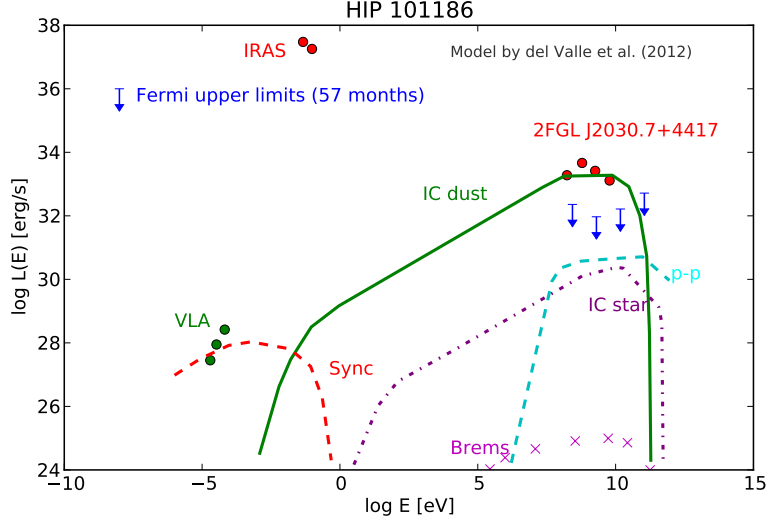
Figure 5.2.: Upper limits of HIP 101186 in the *Fermi*-LAT energy regime compared to model predictions. The red data points depict the *Fermi*-LAT emission for 2FGL J2030.7+4417. The measurements of thermal radiation with IRAS and VLA are also shown.

upper limits constrain the model predictions. In the publication by del Valle et al. (2012) the model is adjusted to match the *Fermi*-LAT emission level of 2FGL J2030.7+4415. The upper limits calculated for the bow shock in this work are lower than the flux of the 2FGL source and consequently constrain the model. The best fit results (del Valle et al. 2012) are obtained with a value of 20 % for q_{rel}, which depicts the fraction of the available power that goes into the acceleration of relativistic particles. This fraction might be much lower.

The second parameter which is adjusted is the equipartition factor χ between kinetic and magnetic energy density. The magnetic energy density is estimated from the kinetic energy density as described in Eq. 2.4. The best fit results of del Valle et al. (2012) yielded $\chi = 0.05$, while the modelling of ζ Ophiuchi assumed $\chi = 0.1$. The other possible reasons for the non-detection are the same as outlined in the previous case, i.e. inefficient particle acceleration and lower magnetic fields.

5.1.3. BD+43°3654

Benaglia et al. (2010) reported the first detection of non-thermal emission from a runaway star, namely BD+43°3654. Their model describing the emission followed the one of del Valle & Romero (2012) and predicted high-energy emission from this bow shock. The search for non-thermal X-ray emission from this object by Terada et al. (2012) revealed no significant emission. Fig. 5.3 shows the upper limits obtained in this work together with the non-thermal radio detection and the X-ray upper limit and the model SED by Benaglia et al. (2010). The upper limits calculated in this work do not constrain the model predictions, but lie in the same range.
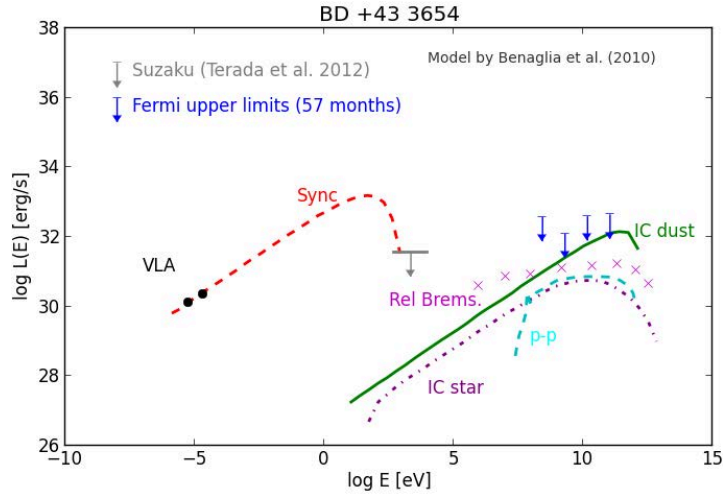
Figure 5.3.: Upper limits of BD+43°3654 compared to model predictions. The Suzaku upper limit is from Terada et al. (2012), the VLA detection and the modelling from Benaglia et al. (2010).

BD+43°3654 is not visible from the southern hemisphere, thus no H.E.S.S. observations are possible. The upcoming CTA will be able to detect the source if the emission in the VHE regime is at a level as predicted by the model.

5.1.4. AE Aurigae (HIP 24575)

Non-thermal X-ray emission from HIP 24575 was discovered by López-Santiago et al. (2012). Their detection of X-ray emission lead to the presented model, where the peak of the inverse Compton emission is in the X-ray regime. In this case the expected level of gamma radiation is much lower and not in reach for current instruments. Fig, 5.4 shows the X-ray detection and the corresponding model by López-Santiago et al. (2012) together with the obtained *Fermi*-LAT upper limits.
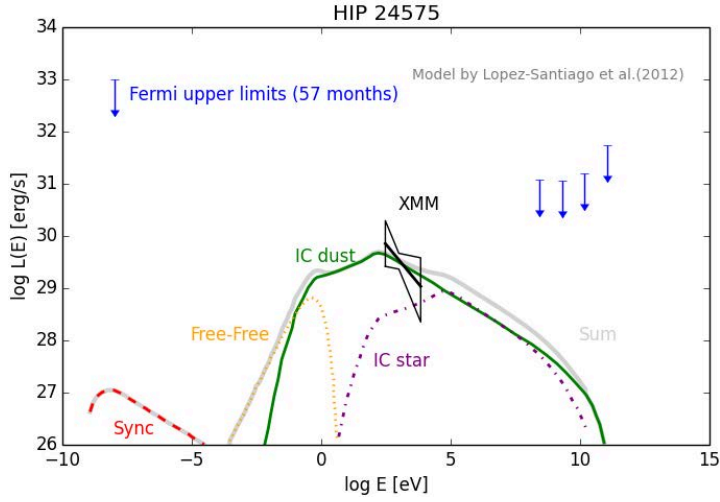
Figure 5.4.: Upper limits of HIP 24575 compared to model predictions from López-Santiago et al. (2012), who also published the X-ray detection shown here.

5.2. Comparison of the Upper Limits of the Bow Shock Sample

To get an overall picture of the gamma-ray emission of bow shocks of runaway stars the model predictions on the individual sources are in this section compared to the upper limits of the bow shock sample for which both H.E.S.S. and *Fermi*-LAT observations exist. The spectral energy density distributions calculated following the model by del Valle & Romero (2012) on the non-thermal emission of bow shocks mainly depend on the parameters for particle acceleration, the magnetic field and the dust emission. The dominating component in the HE and VHE energy regime is the inverse Compton scattering on the dust.

The three model curves depict the predicted inverse Compton emission from dust of three bow shocks for comparison, namely ζ Ophiuchi, BD+43°3654, and HIP 101186. The upper limits in the VHE regime are shown for the seven bow shocks where it was possible to obtain H.E.S.S. limits. In the interest of greater clarity, only the corresponding *Fermi*-LAT upper limits are shown. The remaining flux upper limits lie between the displayed values, as can be seen in Tab. 4.2. The only exception being the third energy bin, where the upper limit for BD+43°3654 is higher than the displayed limits. The models show that the predicted emission is in reach for current instruments, the predicted emission for BD+43°3654 reaches up to TeV energies. The highest model predictions are for HIP 101186, where the model was adjusted to match the *Fermi* flux level of a source, mistakenly assumed to be the bow shock. All *Fermi*-LAT upper limits lie below these predictions.

Flux upper limits are essential to compare the level of emission that we are able to observe from Earth, but the flux depends on the distance to the source. To understand the nature of these objects the more important quantity is the intrinsic luminosity of the objects. In Fig. 5.6 the gamma-ray luminosity predicted by the models are compared to the luminosity upper limits from the analyses. The most constraining limits are obtained for the closest sources, in this sample HIP 72510 and HIP 92865.
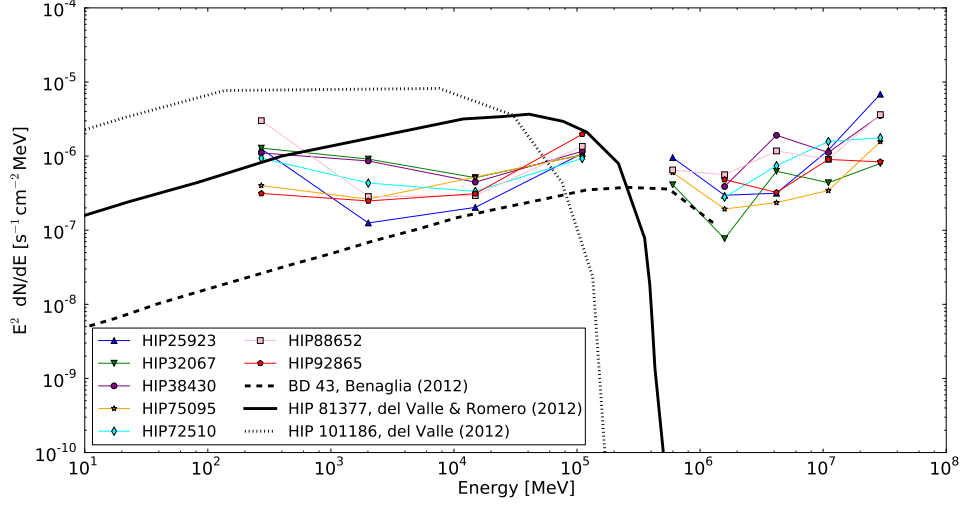
Figure 5.5.: Upper limits for seven of the bow shocks, *Fermi*-LAT and H.E.S.S. combined, together with predicted emission levels for three bow shocks.
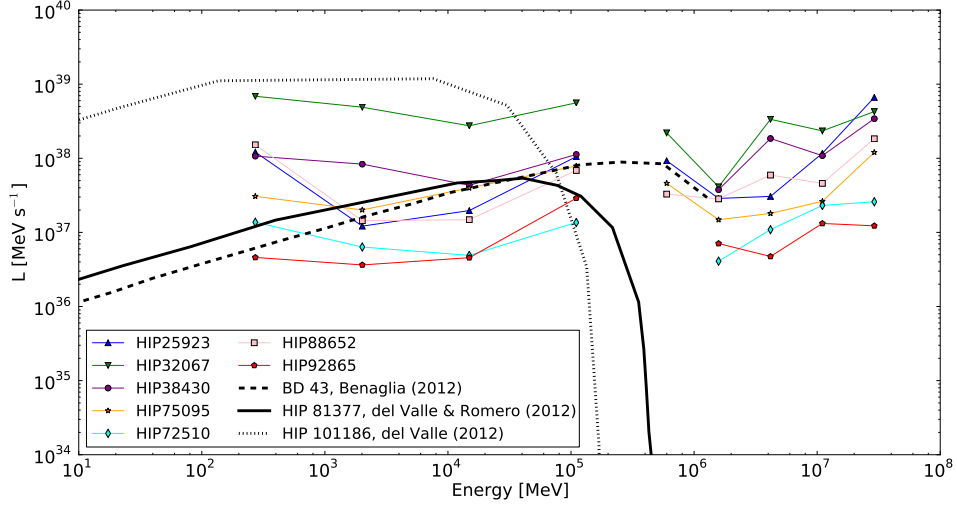
Figure 5.6.: Luminosity upper limits for seven of the bow shocks, *Fermi*-LAT and H.E.S.S. combined. The model predictions for three candidates are also shown.

6. Conclusion and Outlook

The detailed understanding of shock acceleration is one of the milestones in solving the hundred year old puzzle of the origin of cosmic rays. The environments of known sources of cosmic rays are complex and require a detailed modelling to interpret measured emission of gamma rays. The possibility to study shock acceleration in a less complex environment is of great interest. Bow shocks of runaway stars offer this possibility since the systems include only the star, its wind and the interstellar medium. Two circumstances motivated the study performed in the course of this work: The promising detections of non-thermal emission from two of these objects and the modelling of the emission processes which predicted high- and very-high energy gamma ray emission from bow shocks of runaway stars in reach of current instruments.

This thesis presents the analysis of 28 bow shock candidates using data from *Fermi*-LAT. In the very-high energy regime seven of these bow shock candidates are studied with H.E.S.S. No significant emission that could be related to an astrophysical object was found. Neither the *Fermi*-LAT nor the H.E.S.S. analysis revealed a significant signal of gamma rays from any of the bow shock positions. This is the first systematic search for gamma-ray emission from bow shocks of runaway stars. All regions of known bow shocks of runaway stars are analysed in the high-energy regime. This is the first study on bow shocks of runaway stars in the TeV energy regime. The presented analyses constrain the level of gamma-ray emission from bow shocks of runaway stars over six orders of magnitude, from $100\,\mathrm{MeV}$ to $100\,\mathrm{TeV}$.

The calculated upper limits constrain the predictions from models of the non-thermal emission in some of the cases, namely ζ Ophiuchi and HIP 101186. In these cases the assumptions in the model calculation have to be revised. The non-detection implies that either the particle acceleration process is not efficient enough to produce HE gamma-rays or that the magnetic fields are lower.

During the *Fermi*-LAT analysis high-energy emission spatially coincident with a Supernova Remnant, SNR G206.9+2.3, was discovered serendipitously. The center of emission is coincident with the radio SNR and the spectrum is compatible with the expectations for an SNR with that age and size.
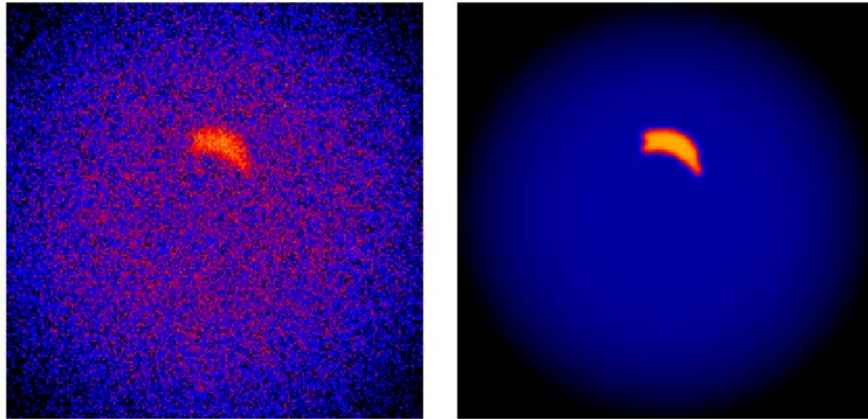
Figure 6.1.: Simulation results for a bow shock observation with CTA performed with *GammaLib/ctools*. The map on the left-hand side shows a count map and on the right-hand side a model map, the side length is $5°$ in both cases. The colour scale is displayed logarithmically to enhance visibility.

Fig. 5.5 and Fig. 5.6 show that current instruments are capable of detecting high- and very-high energy gamma ray emission at the level predicted by the current models describing the non-thermal emission of bow shocks from runaway stars. The luminosity upper limits for several of the bow shocks are lower than the predictions, in the HE and VHE regime.

All known bow shocks of runaway stars have been investigated. A further conceivable step is the search for variable emission. Variable emission from bow shocks of runaway stars due to density variations in the interstellar medium, as suggested recently by del Valle & Romero (2014), extends the possible parameter space to search for high-energy emission from these objects even further. The time scales for the flux variation depend on the size of the density inhomogeneities in the interacting molecular clouds and the speed of the star. The authors come to the conclusion that bow shocks of runaway stars might form a class of variable gamma-ray sources with typical variability time scales of years.

The E-BOSS catalogue as published in 2012 is based on the first data release by WISE, covering 57 % of the sky. The remaining data was published and an updated version of the E-BOSS catalogue is in preparation (Benaglia et al. 2013). The search for emission from the candidates in the second version of the E-BOSS catalogue could lead to the first discovery of HE or VHE emission from a bow shock of a runaway star.

Both instruments presented here will allow for more detailed studies in the future: *Fermi* will continue to scan the entire sky and will therefore be able to detect fainter sources

with increasing time. The *Fermi*-LAT collaboration has worked on improving the event reconstruction and analysis (details are outlined in Atwood et al. 2013). The so-called "Pass 8" data include better reconstruction methods, new event classification, improved background rejection and improved Monte Carlo simulations. This leads to a much larger effective area and better source localisation, which might help to reveal emission from on of the bow shocks of runaway stars. H.E.S.S. has the possibility to perform dedicated deep exposures of interesting regions. Due to the larger collection area of the H.E.S.S. II telescope, the energy threshold has been decreased to several tens of GeV, closing the energy gap between *Fermi* and H.E.S.S.

The forthcoming Cherenkov Telescope Array (CTA) will increase the sensitivity to detect sources in the very-high energy regime by a factor of ~10 compared to H.E.S.S., as shown in Fig. 3.19. The improved angular resolution will allow for a better discrimination between sources and enable possible morphological studies. An improved analysis framework, as described in Appendix A, will further enhance the sensitivity. A simulation of a bow shock observation with CTA, performed with the *GammaLib/ctools* outlined in the Appendix, is shown in Fig. 6.1. The bow shock is modelled with the infrared template and a power law shape, with a prefactor of $5 \cdot 10^{-18}\,\mathrm{cm}^{-2}\mathrm{s}^{-1}$ at 1 TeV and an index of -2.48. The background is modelled with a two dimensional Gaussian with a width of 3°. This example shows that the high-level analysis tools of CTA are already in good shape to offer a unique possibility to study VHE emission from these objects.

A. A Common Analysis Framework for Gamma-Ray Astronomy

The combination of high-energy and very-high-energy data allows to study the energy spectrum of astrophysical sources over more than six orders of magnitude. The energy regimes of *Fermi*-LAT and H.E.S.S. I are overlapping. The energy threshold for H.E.S.S. was lowered with the commissioning of an additional telescope (H.E.S.S. II) with a larger collection area. The combined analysis of data from different instruments in a single likelihood fit allows for a determination of the spectral parameters over a large energy range. The assessment of physical parameters and the corresponding errors are beneficial, especially if physically meaningful models are fitted. An additional advantage of a unified analysis framework is the cross-calibration of instruments.

Especially with the upcoming CTA, new analysis techniques will be of great interest. The approach of *Fermi*-LAT is to analyse a region of interest of several degrees and model all emission present in this area. The IACT approach focusses on one source at a time, only a small ON region is analysed and the background is determined from OFF regions. The analyses of diffuse sources and regions with several sources close to each other are therefore challenging. These challenges can be overcome by adapting the likelihood approach to model the emission for a larger region and optimising the parameters of several sources in a combined fit.

Although the reconstruction and calibration can be diverse, the high-level analysis steps are the same when using event lists and instrument response functions as input. To reconstruct the spectrum of a source the amount of photons originating from the source has to be determined. The amount of detected photons per area and time has to be folded with the instrument response functions to calculate the flux of photons arriving at Earth.

Analyses of gamma-ray data are usually performed using custom-made analysis frameworks developed in the collaborations which operate the telescopes. The *Fermi*-LAT collaboration, including the instrument team and the Fermi Science Support Centre (FSSC), has developed analysis tools for public use to analyse *Fermi*-LAT data, the

so-called *Fermi Science Tools*. The software is maintained by the FSSC. *Fermi* is run as an observatory, meaning that all data is promptly disseminated and available via a data server[1]. The *Fermi Science Tools* are designed following the *FTOOLS* philosophy, which is outlined in Pence et al. (1993). The *FTOOLS* (available via `http://heasarc.nasa.gov/lheasoft/ftools`) are widespread in the astronomical community. Mission-specific subpackages allow for custom calibration and analysis functions for different instruments, e.g. ASCA, Einstein, NuStar, Integral, and Swift. The *Fermi Science Tools* ensure cross-mission compatibility as far as possible by following the same methodology. An additional advantage is the higher user-friendliness. The use of common concepts allows users from one instrument a smoother transition when analysing data from another instrument.

In the VHE regime this is handled differently: Every collaboration operating IACT instruments has developed its own software, mostly independently from each other. The software is subject to proprietary rights in the same manner as is the data. This practise will change with the upcoming CTA, which will also be operated as an open observatory. The software developed to analyse the data will be public. This implies that the data formats and tools should be compliant with existing tools and standards, to increase the user-friendliness. *GammaLib/ctools* is an analysis framework developed in the CTA collaboration which follows the methodology of *FTOOLS* and *Fermi Science Tools*.

The analyses presented in Chap. 4 were performed with the custom-made and well established frameworks. The analysis results of known sources have to be cross-checked with the current software frameworks, before potentially new sources can be reliably investigated with the new framework. Cross-checks are presented in this chapter for W49B, a well-studied supernova remnant clearly detected in both energy regimes. The cross-checks include the validation of the data formats for the event lists and instrument response functions for the different instruments. The reflected region background method was implemented in *GammaLib/ctools* to be able to verify the analysis results and perform first combined fits.

The chapter starts with a description of *GammaLib/ctools*, an open source framework for the analysis of astronomical gamma-ray data. In the second part cross-checks with existing software are presented for *Fermi*-LAT and H.E.S.S. separately. The chapter concludes with a joint fit of *Fermi*-LAT and H.E.S.S. data.

---

[1]`http://fermi.gsfc.nasa.gov/ssc/data/access/`

A.1. GammaLib/ctools

The advantages of a combined analysis framework for gamma-ray astronomy, together with the need for a software designed to analyse CTA data, lead to the development of *GammaLib/ctools*. *GammaLib* is a framework developed with the goal to unify the analysis of gamma-ray data. First developments of the *GammaLib* library were presented in Knödlseder (2012). For the scientific analysis of data, a set of executables is developed, the so-called *ctools*. Recent developments in the *GammaLib/ctools* framework in the context of CTA were presented in Knödlseder et al. (2013).

A.1.1. Data Format Definitions

The usage of a common analysis framework implies the agreement on a common data format. Since the IACT collaborations have custom-made frameworks, they also have custom-made data formats.

The input for *GammaLib/ctools* are event lists including the reconstructed photon properties like energy, direction and arrival time, and instrument response functions. For these files a common format has to be defined. In the *GammaLib/ctools* framework the FITS format is used.

FITS stand for Flexible Image Transport System (Pence et al. 2010) and is the standard format used by NASA and the international astronomical union (IAU). A FITS file consists of one or more header and data units (HDUs). The data can be multi dimensional, which offers a great flexibility to the user. The header consists of header keywords, which specify the size and format of the data. The header keywords have to follow the FITS standards[2]. FITS was developed in the 1970's as a format to store and interchange data. It is a powerful format and is in widespread use since then. The usage of FITS files is facilitated by the available tools, widely used throughout the astronomical community. The *FTOOLS* allow to create, analyse, and modify FITS files; ds9[3] visualises FITS images for astronomical applications.

Fermi-LAT Data Format

The *Fermi Science Tools* follow the concept of the *FTOOLS* and the data is therefore stored in the FITS format. The data products, including event lists, later analysis products, and IRFs, are stored in the FITS format and can thus be instantly used in the *GammaLib/ctools* framework.

---

[2]http://archive.stsci.edu/fits/fits_standard/
[3]http://ds9.si.edu/

CTA Data Format

The CTA consortium has agreed on a preliminary FITS data format for the event lists and the instrument response functions. The detailed structure of the files is still subject to changes. The development of a software implies the thorough investigation of different possible data formats. The advantages of the FITS format with its great flexibility and interchangeability are outlined above. From Monte Carlo simulations IRFs are calculated, which can be used to simulate CTA data within the *GammaLib/ctools* framework. An example for a simulation of CTA observation is shown in Fig. 6.1.

H.E.S.S. Data Format

For the analysis of IACT data *GammaLib/ctools* needs the following input files in FITS format: event lists and IRFs for each observation. In definition of an observation is a time span for which the provided IRFs are valid. In the case of H.E.S.S., one run is treated as one observation.

The H.E.S.S. collaboration uses the object serialisation of the ROOT[4] format to store its high-level data products. The data has to be exported to the FITS format to be able to analyse it with *GammaLib/ctools*. The export of the event lists is done after the calibration, reconstruction, and the application of cuts, as outlined in Sect. 3.2.3. The event lists are exported into one FITS file per run. The most important properties stored in the event list for each photon are: event arrival time; energy; direction in sky coordinates (RA, Dec in J2000), detector coordinates (x, y) and the horizon system (zenith and azimuth).

The IRFs of H.E.S.S. are stored in multidimensional lookup tables created from extensive Monte Carlo simulations. To allow an easy usage in *GammaLib/ctools*, the corresponding IRFs for each run, i.e. the effective area (A_{eff}), the point spread function (PSF), and the energy dispersion (D), are exported into FITS files, with the specifications of the CTA FITS format. Further details of exporting the H.E.S.S. data into a *GammaLib* compatible FITS format are outlined in Mayer (2014).

A.1.2. GammaLib

GammaLib is an open source C++ library which creates a framework for an instrument independent analysis of gamma-ray data. The framework is almost self-contained, meaning that is does not depend on any third-party software, the only exception being the cfitsio library (Pence 1999) for the reading and writing of FITS files. *GammaLib*

---

[4]`http://root.cern.ch/`
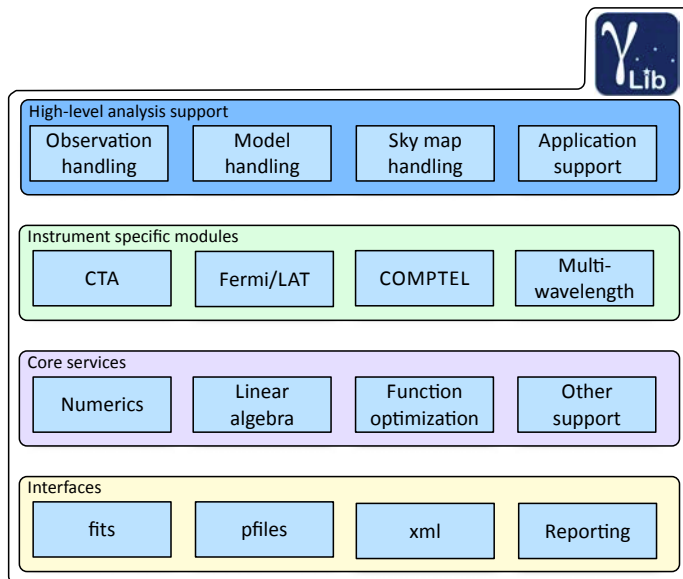
Figure A.1.: Schematic overview of the structure of the *GammaLib* library with its four layers. Image from: Knödlseder et al. (2013).

classes are wrapped into Python modules, with the use of SWIG[5]. This allows to call them interactively or to script them.

The source code of *GammaLib* is freely available under the GNU General Public license at `http://sourceforge.net/projects/gammalib/`. A bug-tracking system is set up at: `https://cta-redmine.irap.omp.eu/projects/gammalib`.

GammaLib is developed in a multi-platform manner, meaning that is designed to compile on POSIX conform platforms. A continuous automated build-system is set up to ensure the compilation on different systems.

A schematic of the framework's structure is shown in Fig. A.1. There are four layers of software: the high-level analysis support, instrument specific modules, core services and interfaces.

The interfaces allow for different formats: the FITS format as mentioned above and the Extensible Markup Language (XML[6]) format, pfiles, and reporting files. The XML format is a markup language defining rules to encode documents, allowing for easy readability by humans and machines. In *GammaLib* it is used to specify observations and

---

[5]`http://www.swig.org/`
[6]`http://www.w3.org/TR/REC-xml`

models. One observation is defined by a data set with corresponding instrument response functions. The IRAF parameter format is used to define the pfiles. The reporting files are simple logfiles.

The core services implement general methods used by many modules including numerics, linear algebra calculations, and function minimisation.

Instrument specific modules are implemented for: COMPTEL, *Fermi*-LAT, and CTA (which includes the support of data from other IACTs). COMPTEL[7] (short form of Imaging Compton Telescope) was operating from 1991 until 2000 on board the Compton satellite. It was sensitive to photons with energies between 1 and 30 MeV. The generic multi-wavelength module allows to add flux points from any instrument to spectral fits. This functionality allows for fits of spectral energy distributions over a broad energy range.

The high-level analysis support is divided into observation, model, and sky map handling. One observation describes a time period for which an event list and corresponding IRFs are given. The observation contains information like the event data, the pointing position, the observation time, ...). The model includes spatial and spectral information about all sources in the analysed region. For each component it is specified to which instrument or instruments it belongs.

A.1.3. ctools

ctools are a set of executables developed for the high-level analysis of gamma-ray data. The development follows the *FTOOLS* philosophy of having a modular stucture as outlined in Pence et al. (1993), which also influenced the development of the *Fermi* Science Tools. The modularity allows a user-specific analysis. The tools are developed in the CTA consortium and available at `http://cta.irap.omp.eu/ctools`. The analysis workflow is schematically shown in Fig. A.2. Two analysis approaches can be pursued, a binned and an unbinned workflow, analogous to the *Fermi Science Tools*.

Each tool performs a single specific analysis step which is also reflected in the name of the tool. Users of the *Fermi Science Tools* will easily adapt to *ctools*: the names of the tools are the same, except for the first letter, the likelihood fit in *Fermi Science Tools* is performed with `gtlike` in *ctools* it is named `ctlike`. The currently available *ctools* are:

- `ctobssim`: to simulate observations.
- `ctselect`: to select events which fulfil certain criteria like e.g. energy range, time range or distance to a source.

---

[7]detailed information at `http://heasarc.gsfc.nasa.gov/docs/cgro/cgro/comptel.html`
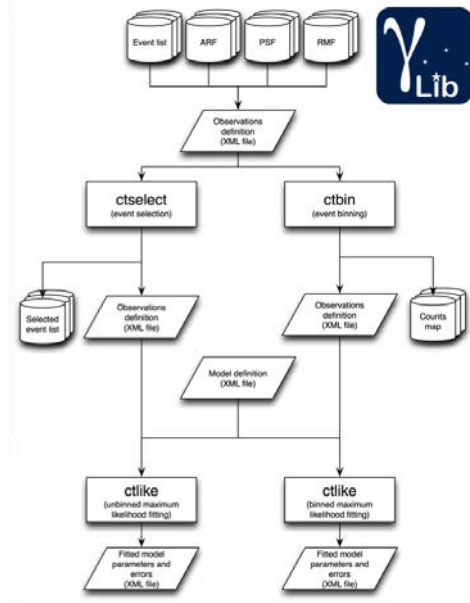
Figure A.2.: Schematic overview of the workflow in of *ctools*. The left-hand side shows the unbinned workflow, the right-hand side the binned one. Image credit: J.Knödlseder.

- `ctbin`: to create three dimensional count cubes, consisting of two spatial dimensions and one energy dimension.
- `ctlike`: to perform the maximum likelihood fit of the model to the data.
- `ctmodel`: to calculate count cubes for a given model and observation set.

All *ctools* can be called from the command line with the use of IRAF paramter files, scripted with shell scripts or called directly from Python. An advantage of Python is the in memory passing of intermediate results, they don't need to be stored in this case. A third option is to script them via shell scripts. For the validation of the *Fermi*-LAT analysis presented in the next section only `ctlike` is needed, all other steps are done in the *Fermi Science Tools*.

A.2. Validation of the Fermi-LAT Analysis

The cross check between *Fermi Science Tools* and *ctools* is performed on a 5 year data set of a known SNR. W49B (G043.4-00.2) is an SNR which is interacting with a molecular cloud. Its age is between 4000–6000 yr. The source was detected in the first catalogues

by the *Fermi*-LAT collaboration and was studied in detail by Abdo et al. (2010).

The analysis steps for the *Fermi*-LAT analysis using *Fermi Science Tools* are described in Sect. 3.1.3. The *Fermi Science Tools* 09-32-05 are used for this analysis. The high-level *Fermi*-LAT analysis is very similar to the approach used in *ctools*. Only the likelihood fit is performed with *ctools*. All other steps, including the exposure calculation and the folding with the PSF are only done in the *Fermi Science Tools*. The input for the likelihood fit are the source map, the model describing the emission, and the instrument response functions. The response functions for *Fermi*-LAT are stored in the FITS format, which can be directly read in by *GammaLib*.

The input model is composed of the source, the diffuse components and the known sources in the region of interest. W49B is modelled with a logParabola as described in Eqn. 3.2. The parameters are the prefactor N_0, the index α and the curvature β. The galactic diffuse component is provided with a three dimensional FITS file, two spatial and one energy dimension. The spectral shape used to model the galactic diffuse emission is a power law. The power law as defined in Eqn. 3.1, is described with the prefactor N_0, a reference energy (E_0, fixed during the fit) and index γ. During the fit the spectrum is allowed to vary, the prefactor and index of the power law give an indication for the goodness of the fit. The template is created that N_0 is expected to be one and γ zero. The spectral shape of the isotropic component is provided as an input file and the normalisation is free during the fit. The input model for the known sources is the 2FGL. The parameters for sources closer than $3°$ to the source W49B are left free during the fit.

The test on the capability of *ctools* to fit *Fermi*-LAT data is performed on two different data sets of W49B. The standard format used by the *Fermi*-LAT collaboration until 2013 is the "Pass 7" format. An undated data set, after a better understanding of the IRFs the data were reprocessed, creating the "Pass 7 reprocessed" data set.

Caveats

The development of *GammaLib/ctools* is progressing quickly, but not all functionality is fully implemented and tested. In the case of the *Fermi*-LAT validation this leads to the following consequences: The *ctools* are not (yet) capable of convolving the averaged IRFs with the diffuse models, therefore the source maps have to be calculated by the *Fermi Science Tools*.

The fitting procedure in *ctools* is not yet fully capable to handle the error calculation in the case of correlated parameters. One investigated reason is the calculation of the curvature matrix used for error estimation, in which the second derivative of the parameters are dropped. Further studies are under way to solve this problem. The break energy and scale values, defined in Eqn. 3.1 and Eq. 3.2 are therefore fixed during the *ctools* fit.

Source	Parameter	gtlike	ctlike
W49B	N_0 at $0.3\,\mathrm{GeV}$ $[10^{-10}]$	2.483 ± 0.001	2.43 ± 0.04
	α	1.905 ± 0.002	1.90 ± 0.13
	β	0.0819 ± 0.0009	0.08 ± 0.02
Galactic diffuse	N_0 at $1\,\mathrm{MeV}$	1.1625 ± 0.0002	1.156 ± 0.005
	γ	$-(0.03834 \pm 0.00008)$	$-(0.043 \pm 0.001)$
Isotropic diffuse	N_0	0.598 ± 0.005	0.59 ± 0.04

Table A.1.: Cross-check between *Fermi Science Tools* and *ctools*, using 5 years of Pass 7 *Fermi*-LAT data of W49B. The units of N_0 are: $\mathrm{cm}^{-2}\,\mathrm{s}^{-1}\,\mathrm{MeV}^{-1}$. The third and forth column show the fit results for the two different analysis frameworks.

Pass 7 data

The cross-check of the fit result for Pass 7 data is shown in Tab. A.1. The fit results are shown for W49B and the Galactic and isotropic component. The fitted values for the *Fermi Science Tools* tool `gtlike` are displayed in the third column, the results for the *ctools* tool `ctlike` in the forth column. The `ctlike` values for all three components, W49B, Galactic and isotropic diffuse, lie within the statistical errors of the `gtlike` fitted values. Noticeable is that the errors in the *ctools* fit are larger. The improvement of the error calculation in *GammaLib/ctools* is under study.

This shows that *GammaLib/ctools* is capable to analyse *Fermi*-LAT Pass 7 data with the corresponding instrument response functions. The fit results for `ctlike` agree with the ones from `gtlike`.

Pass 7 Reprocessed data

The *Fermi*-LAT collaboration has reprocessed the Pass 7 data set with updated instrument response functions. This data is referred to as P7REP, details are outlined in Bregeon et al. (2013). The model input for this analysis is the same as for the Pass 7 data with the exception of the diffuse models, which were updated. The model inputs for the `gtlike` and `ctlike` are the same. The cross-check of the fit result is shown in Tab. A.2 and illustrated in Fig.A.3. The good agreement of `gtlike` and `ctlike` is clearly visible in the figure.

The fitted logParabola curves for W49B agree very well over the entire energy range. The fit of the spectral shape is performed in an energy range from $500\,\mathrm{MeV}$–$300\,\mathrm{GeV}$. Spectral points are calculated by refitting in separate bins, as described in Sect. 3.1.3. The energy range is limited to a certain bin and a subsequent fit is performed to calculate the spectral

Source	Parameter	`gtlike`	`ctlike`
W49B	N_0 at $0.3\,\text{GeV}$ $[10^{-10}]$	2.87 ± 0.02	2.85 ± 0.04
	α	1.98 ± 0.03	1.98 ± 0.13
	β	0.069 ± 0.008	0.067 ± 0.003
Galactic diffuse	N_0 at $1\,\text{MeV}$	1.102 ± 0.003	1.097 ± 0.005
	γ	$-(0.0172 \pm 0.0008)$	$-(0.022 \pm 0.001)$
Isotropic diffuse	N_0	0.37 ± 0.03	0.36 ± 0.04

Table A.2.: Cross-check between *Fermi Science Tools* and *ctools*, using 5 years of *Fermi*-LAT data (P7REP) of W49B. The units of N_0 are: $\text{cm}^{-2}\ \text{s}^{-1}\ \text{MeV}^{-1}$. The third and forth column show the fit results for the two different analysis frameworks.
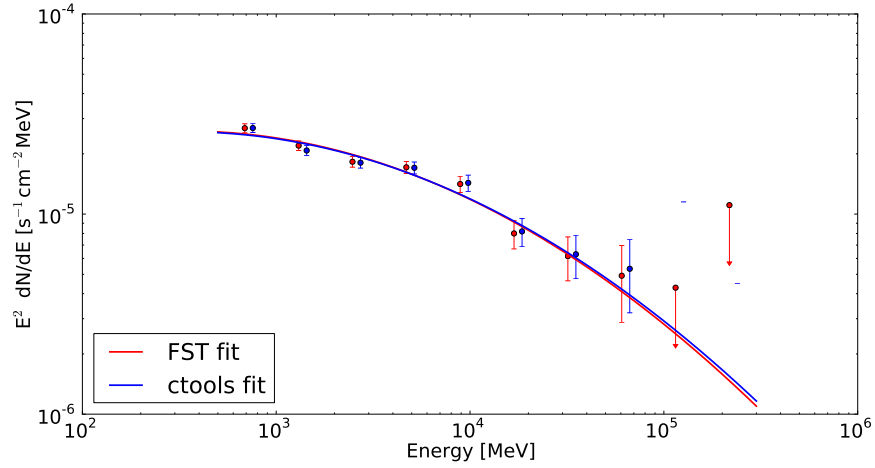
Figure A.3.: Comparison of the spectral fit results of W49B, the red curve and points depict the *Fermi Science Tools* results, the blue ones *ctools* results. The spectral points for *ctools* are shifted in energy to enhance the visibility. The two highest energy bins are missing in the *ctools* since upper limit calculation is not yet implemented.

point in this bin. During this fit the parameters of all sources except W49B and the normalisations of the diffuse components are fixed. The spectral points correspond to the normalisation of the source, W49B. If the source cannot be detected significantly in an energy bin, an upper limit on the flux is calculated. The spectral points shown in Fig. A.3 confirm the good agreement between the *Fermi Science Tools* and *ctools* analysis. To enhance visibility, the spectral points for the *ctools* results are shifted by $10\,\%$ to higher energies. The upper limit calculation is not yet implemented in *ctools*, resulting in two empty bins for the highest energies.

This shows that the implementation of the *Fermi*-LAT analysis in *GammaLib/ctools* is working, the results are consistent with the *Fermi Science Tools*.

A.3. Implementation and Validation of IACT Analyses

The analysis of VHE gamma ray data is different from the approach of *Fermi* and *ctools* which create a model including the background. In IACTs analyses the background level is estimated from dedicated OFF regions, chosen to best mimic the ON region. The ON region is rather small and usually one source at a time is analysed. Details of the H.E.S.S. analysis are outlined in Sect.3.2.3, a schematic view of the background method shown in Fig. 3.18.

The cross-checks in this energy range include therefore the background determination. The presented cross-checks of analysis results also imply the cross-checks of different data formats, since the data has to be exported to the FITS format.

Background modelling

The results for two different background techniques are presented here, the reflected region method and the Gaussian shape method. The reflected region background method is used in the H.E.S.S. analysis and outlined in Sect. 3.2.3. The background in the ON region is determined from several OFF regions, selected with the same distance to the camera centre and with the same size.

The Gaussian background models the background over the entire ROI with the assumption of a Gaussian shape centred on the camera center. The background counts (B) depend on their angular distance (θ) to the camera center.The model has the form:

$$B(\theta) \propto \exp\left(\frac{1}{2}\frac{\theta^4}{\sigma^2}\right) \tag{A.1}$$

σ describes the width of the distribution and is a free parameter in the fit.

An alternative background modelling approach which uses data from other observations to construct the background is presented in Mayer (2014).

The Gaussian background method follow the approach to model the emission over a large region. The region of interest in this approach is typically of the order of several degrees. This is not true for the reflected regions approach, where only events from the source region (typically $0.1°$) and from the OFF regions are selected.

Likelihood calculation

The likelihood function in the case of the Gaussian approach is the same as presented in Eq. 3.4. There is only one term for the analysed region.

In the reflected region approach, the likelihood function contains one term for the ON region and one term for the OFF regions. The fit is performed simultaneously in the ON and OFF regions, with the background being present in both. This adds cross-terms in the calculation of the derivatives of the likelihood, which have to be taken into account.

Validation with H.E.S.S. data

The supernova remnant W49B is clearly detected in the H.E.S.S. energy range in the standard H.E.S.S. analysis. The spectral shape in this energy regime follows a power law. To validate the two presented background modelling techniques the H.E.S.S. data are analysed with the two approaches in the *GammaLib/ctools* framework. The fitted results for W49B are shown in Fig. A.4. The results of the H.E.S.S. Model analysis are shown with a black line and grey confidence band. The results for the two background methods, Gaussian and reflected region, implemented in the *ctools* framework are depicted with green and blue lines, respectively.
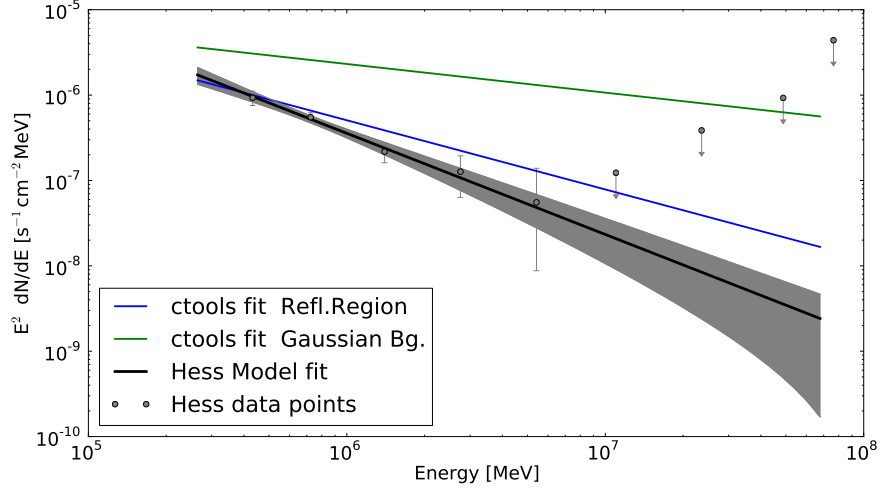
Figure A.4.: Comparison of the spectral fit results of W49B, the grey curve and points depict the H.E.S.S. model analysis results, the blue and green ones *ctools* results.

The discrepancy of the different results, especially for the Gaussian method is clearly visible. The normalisation of W49B is far too high. The results for the reflected region method look better, the normalisation lies within statistical errors of the H.E.S.S. result, but the index is not compatible with the H.E.S.S. results.

The results of this study show, that the *GammaLib/ctools* framework is on a good way, but further in-depth studies are needed to confirm the capabilities to perform analyses of VHE data. One study of this kind is presented in the next paragraph.

Validation with simulated CTA data

To check the functionality of the analysis method, simulations of CTA observations were performed and analysed. Two observations with pointings $\pm 0.5°$ offset to the source position with a duration of $18000\,$s (5 hours) each were simulated assuming a Gaussian background. The simulated and fitted parameter are shown in Tab. A.3 and visualised in Fig. A.5. The width (σ) of the Gaussian cannot be fitted in the reflected reg. method and is therefore fixed to the simulated value. The fit results for the reflected region background method are compatible with the simulations in the case of the background fits, the normalisation and index of W49B are statistically not compatible.

The analysis of simulated CTA data shows, that it is principally possible to analyse IACT data in the *GammaLib/ctools* framework and that in-depth studies are needed to understand the discrepancies as shown in Fig. A.4.

Source	Parameter	Simulation	Reflected Reg. Bg.	Gaussian Bg.
W49B	N_0 at $1\,$TeV $[10^{-19}]$	3.50	3.04 ± 0.08	3.23 ± 0.38
	γ	3.18	2.81 ± 0.04	3.24 ± 0.07
Background	N_0 at $1\,$MeV $[10^{-5}]$	2.00	1.64 ± 0.21	2.05 ± 0.03
1. observation	γ	2.00	2.16 ± 0.08	1.984 ± 0.007
	σ	5	5	4.98 ± 0.03
Background	N_0 at $1\,$MeV $[10^{-5}]$	2.00	2.15 ± 0.20	1.99 ± 0.03
2. observation	γ	2.00	1.94 ± 0.06	2.008 ± 0.007
	σ	5	5	4.98 ± 0.03

Table A.3.: Cross-check between simulated and fitted parameters for simulated CTA data. The units of N_0 are: $\text{cm}^{-2}\,\text{s}^{-1}\,\text{MeV}^{-1}$. The third column lists the input parameters of the simulation and the forth and fifth columns the fit results for the reflected region and Gaussian background, respectively.
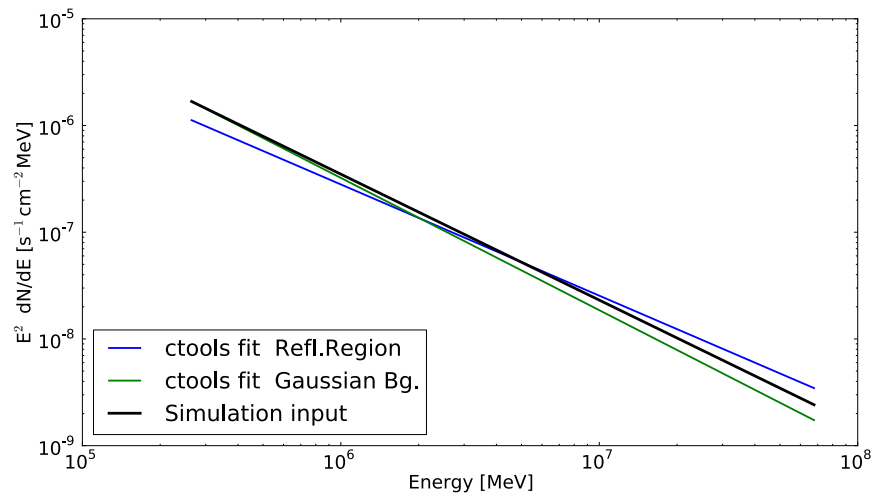
Figure A.5.: Comparison of the spectra of a simulated CTA observations, the black curve depicts the simulation input, the blue and green ones *ctools* fit results. Two observations with 5 h each were simulated and analysed with the reflected region and Gaussian background methods.

A.4. Combined Fit of Fermi-LAT and H.E.S.S. Data: W49B

The combination of the data from several instruments in a single fit is an important step in the development of the *GammaLib/ctools* framework. W49B is a good example, since it is clearly detected in both energy regimes. The combined fit spans over both energy regimes, about six orders of magnitude. The event lists are assigned to an instrument with a corresponding IRF. To combine the fit, the models of both observations are joined. For each source in the model it is clearly stated whether it belongs to the *Fermi*-LAT and/or H.E.S.S.. Only the model for W49B is assigned to both instruments.

The combined fit shown in Fig. A.6 is proof, that the first steps towards a common framework are mastered. The *GammaLib/ctools* framework offers great possibilities for the analysis of gamma-ray data and is well on track to become the standard analysis software for CTA.
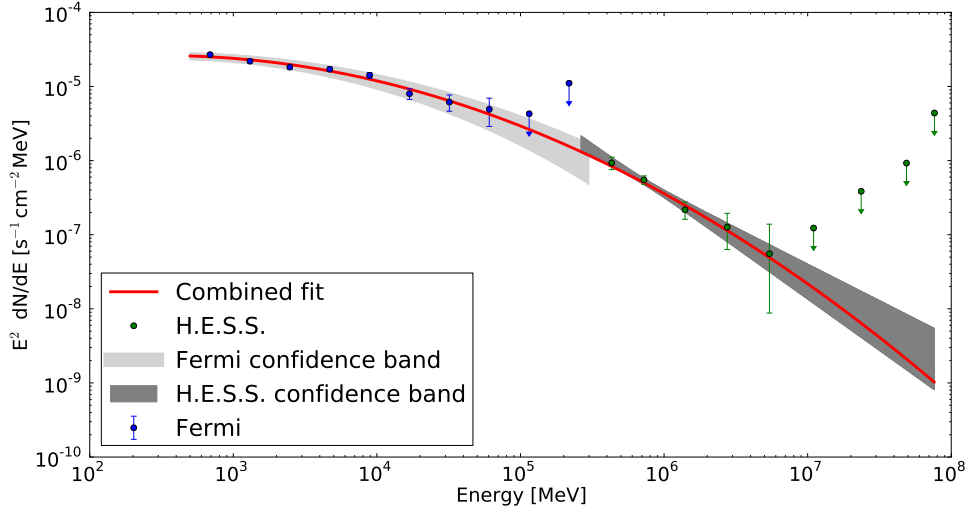
Figure A.6.: The combined fit of *Fermi*-LAT and H.E.S.S. data from the SNR W49B obtained with *GammaLib/ctools* is depicted with the red line. The grey shaded band depict the confidence bands for the fits in the dedicated software frameworks, light grey the *Fermi Science Tools* result and dark grey the H.E.S.S. result.

B. Additional information

Template preparation

Two examples of the templates for the *Fermi*-LAT analysis are shown in Figs. 4.2 and 4.3. The ones for ζ Ophiuchi and HIP 97796 are shown here:
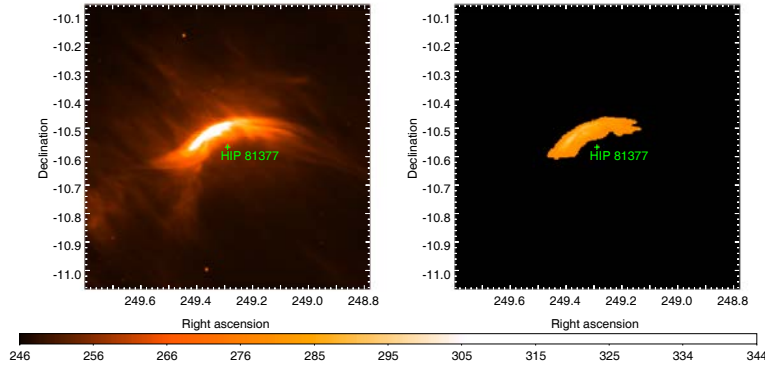
(a) HIP 81377 WISE count map.
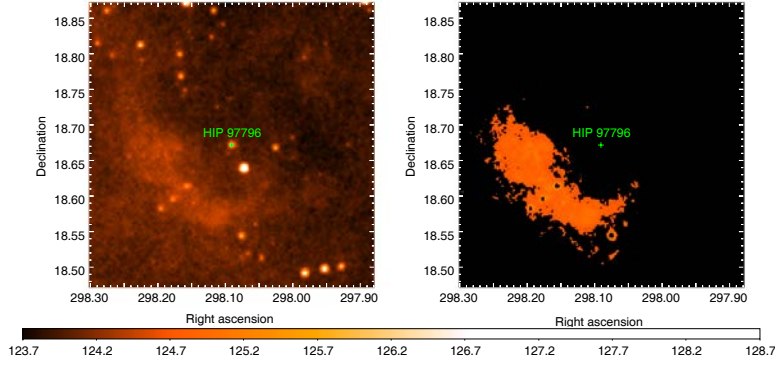
(b) HIP 97796 WISE count map.

Figure B.1.: WISE count map for HIP 81377 (top panel) and HIP 97796 (bottom panel) in $22\,\mu$m. The images on the left-hand side show the publicly available data, the ones on the right-hand side the processed ones for the template analysis.

Table B.1.: Overview about 2FGL sources released during subsequent fits although further away than 3° and additional sources included in the model.

Star	l [°]	b [°]	2FGL sources freed	additional source(s) (RA, DEC) (J2000) [°]
HIP 2036	120.9137	+09.0357	2FGL J0109.9+6132	-
HIP 2599	120.8361	+00.1351	2FGL J0109.9+6132 2FGL J0102.7+5827	-
HIP 11891	134.7692	+01.0144	2FGL J0109.9+6132	-
HIP 16518	156.3159	−16.7535	2FGL J0319.8+4130 2FGL J0316.6+4119	-
HIP 17358	150.2834	−05.7684	2FGL J0319.8+4130	-
HIP 22783	144.0656	+14.0424	-	-
HIP 24575	172.0813	−02.2592	-	-
HIP 25923	210.4356	−20.9830	2FGL J0501.2-0155	-
HIP 26397	174.0618	+01.5808	2FGL J0622.9+3326	-
HIP 28881	164.9727	+12.8935	-	-
HIP 29276	263.3029	−27.6837	2FGL J0526.1-4829	-
HIP 31766	210.0349	−02.1105	2FGL J0631.7+0428	-
HIP 32067	206.2096	+00.7982	-	(102.01,6.83) (100.74,5.35)
HIP 34536	224.1685	−00.7784	2FGL J0730.2-1141	-
HIP 38430	243.1553	+00.3630	-	(118.52, −26.83)
HIP 62322	302.4492	−05.2412	2FGL J1330.1-7002 2FGL J1422.3-6841	-
HIP 72510	318.7681	+02.7685	-	-
HIP 75095	322.6802	+00.9060	2FGL J1603.8-4904	-
HIP 77391	330.4212	+04.5928	2FGL J1603.8-4904 2FGL J1604.5-4442 2FGL J1630.1-4615 2FGL J1650.1-5044	-
HIP 78401	350.0969	+22.4904	Fermi J1532-1319	(233.16,−13.35)
HIP 81377	006.2812	+23.5877	-	(249.85,−10.072)
HIP 82171	329.9790	−08.4736	-	-
HIP 88652	015.1187	+03.3349	2FGL J1833.6-2104 2FGL J1819.3-1523	-
HIP 92865	041.7070	+03.3784	2FGL J1857.2+0055	-
HIP 97796	056.4824	−04.3314	-	-
HIP 101186	082.3557	2.9571	-	(307.51, 43.71)
BD+43°3654	082.4100	+02.3254	2FGL J2001+4352	-
HIP 114990	112.8862	+03.0998	-	-

List of Figures

List of Tables

Bibliography

Abdo, A. A., Ackermann, M., Ajello, M., et al. 2010, ApJ, 722, 1303

Abdo, A. A., Ajello, M., Allafort, A., et al. 2013, ApJS, 208, 17

Ackermann, M., Ajello, M., Albert, A., et al. 2013a, ApJ, 771, 57

Ackermann, M., Ajello, M., Albert, A., et al. 2012, ApJS, 203, 4

Ackermann, M., Ajello, M., Allafort, A., et al. 2013b, Science, 339, 807

Aharonian, F., Akhperjanian, A. G., Aye, K.-M., et al. 2005, Science, 307, 1938

Aharonian, F., Akhperjanian, A. G., Bazer-Bachi, A. R., et al. 2006, ApJ, 636, 777

Aharonian, F., Buckley, J., Kifune, T., & Sinnis, G. 2008, Reports on Progress in Physics, 71, 096901

Aharonian, F. A., Akhperjanian, A. G., Aye, K.-M., et al. 2004, Nature, 432, 75

Antonelli, L. A., Blasi, P., Bonanno, G., et al. 2009, ArXiv:0906.4114

Atwood, W., Albert, A., Baldini, L., et al. 2013, ArXiv e-prints

Atwood, W. B., Abdo, A. A., Ackermann, M., et al. 2009, ApJ, 697, 1071

Baldini, L. 2014, ArXiv e-prints

Baranov, V. B., Krasnobaev, K. V., & Kulikovskii, A. G. 1971, Soviet Physics Doklady, 15, 791

Bell, A. R. 1978, MNRAS, 182, 147

Benaglia, P., Romero, G. E., Martí, J., Peri, C. S., & Araudo, A. T. 2010, A&A, 517, L10

Benaglia, P., Stevens, I. R., & Peri, C. S. 2013, ArXiv e-prints

Berge, D., Funk, S., & Hinton, J. 2007, A&A, 466, 1219

Beringer, J., Arguin, J.-F., Barnett, R. M., et al. 2012, Phys. Rev. D, 86, 010001

Bernlöhr, K. 2000, Astroparticle Physics, 12, 255

Blaauw, A. 1956, PASP, 68, 495

Blaauw, A. 1961, Bull. Astron. Inst. Netherlands, 15, 265

Blumenthal, G. R. & Gould, R. J. 1970, Reviews of Modern Physics, 42, 237

Bregeon, J., Charles, E., & M. Wood for the Fermi-LAT collaboration. 2013, ArXiv e-prints

Brown, D. & Bomans, D. J. 2005, A&A, 439, 183

Cheung, C. C., Hays, E., Venters, T., Donato, D., & Corbet, R. H. D. 2012a, The Astronomer's Telegram, 4224, 1

Cheung, C. C., Shore, S. N., De Gennaro Aquino, I., et al. 2012b, The Astronomer's Telegram, 4310, 1

Comerón, F. & Pasquali, A. 2007, A&A, 467, L23

Condon, J. J., Cotton, W. D., Greisen, E. W., et al. 1998, AJ, 115, 1693

Davies, R. D. & Meaburn, J. 1978, A&A, 69, 443

de Naurois, M. 2012, Habilitation, Laboratoire Leprince-Ringuet, Ecole polytechnique, Palaiseau Cedex, France

de Naurois, M. & Rolland, L. 2009, Astroparticle Physics, 32, 231

del Valle, M. V. & Romero, G. E. 2012, A&A, 543

del Valle, M. V. & Romero, G. E. 2014, A&A, 563, A96

del Valle, M. V., Romero, G. E., & Becker, M. D. 2012, A&A, 550

Draine, B. T. & Lee, H. M. 1984, ApJ, 285, 89

Drury, L. O. 1983, Reports on Progress in Physics, 46, 973

Feldman, G. J. & Cousins, R. D. 1998, Phys. Rev. D, 57, 3873

Fermi, E. 1949, Physical Review, 75, 1169

Funk, S. 2005, Dissertation, Ruprecht-Karls-Universität, Heidelberg, Germany

Funk, S., Hinton, J. A., & for the CTA Consortium. 2013, Astroparticle Physics, 43, 348

Gao, X. Y., Reich, W., Han, J. L., et al. 2010, A&A, 515, A64

Gies, D. R. & Bolton, C. T. 1986, ApJS, 61, 419

Graham, D. A., Haslam, C. G. T., Salter, C. J., & Wilson, W. E. 1982, A&A, 109, 145

Green, D. A. 2009, Bulletin of the Astronomical Society of India, 37, 45

Hasinger, G., Altieri, B., Arnaud, M., et al. 2001, A&A, 365, L45

Heitler, W. 1954, Quantum theory of radiation

Helene, O. 1983, Nuclear Instruments and Methods in Physics Research, 212, 319

H.E.S.S. collaboration, T. in prep., The H.E.S.S. Galactic Plane Survey

Hillas, A. M. 1985, International Cosmic Ray Conference, 3, 445

Hillas, A. M. 2006, ArXiv Astrophysics e-prints

Hinton, J. 2009, New Journal of Physics, 11, 055005

Hofmann, W. 2006, ArXiv Astrophysics e-prints

Hoogerwerf, R., de Bruijne, J. H. J., & de Zeeuw, P. T. 2000, ApJ, 544, L133

IceCube Collaboration. 2013, Science, 342

Jelley, J. V. & Porter, N. A. 1963, QJRAS, 4, 275

Klein, O. & Nishina, T. 1929, Zeitschrift fur Physik, 52, 853

Knödlseder, J. 2012, in Astronomical Society of the Pacific Conference Series, Vol. 461, Astronomical Data Analysis Software and Systems XXI, ed. P. Ballester, D. Egret, & N. P. F. Lorente, 65

Knödlseder, J., Mayer, M., Deil, C., et al. 2013, ArXiv e-prints

Kraushaar, W. L., Clark, G. W., Garmire, G. P., et al. 1972, ApJ, 177, 341

Leahy, D. A. 1986, A&A, 156, 191

Li, T.-P. & Ma, Y.-Q. 1983, ApJ, 272, 317

López-Santiago, J., Miceli, M., del Valle, M. V., et al. 2012, The Astrophysical Journal Letters, 757, L6

Mattox, J. R., Bertsch, D. L., Chiang, J., et al. 1996, ApJ, 461, 396

Mayer, M. 2014, Dissertation, Universität Potsdam, Germany

McComas, D. J., Alexashov, D., Bzowski, M., et al. 2012, Science, 336, 1291

Meegan, C., Lichti, G., Bhat, P. N., et al. 2009, ApJ, 702, 791

Nolan, P. L., Abdo, A. A., Ackermann, M., et al. 2012, ApJS, 199, 31

Noriega-Crespo, A., van Buren, D., & Dgani, R. 1997, AJ, 113, 780

Pence, W. 1999, in Astronomical Society of the Pacific Conference Series, Vol. 172, Astronomical Data Analysis Software and Systems VIII, ed. D. M. Mehringer, R. L. Plante, & D. A. Roberts, 487

Pence, W., Blackburn, J. K., & Greene, E. 1993, in Astronomical Society of the Pacific Conference Series, Vol. 52, Astronomical Data Analysis Software and Systems II, ed. R. J. Hanisch, R. J. V. Brissenden, & J. Barnes, 541

Pence, W. D., Chiappetti, L., Page, C. G., Shaw, R. A., & Stobie, E. 2010, A&A, 524, A42

Peri, C. S., Benaglia, P., Brookes, D. P., Stevens, I. R., & Isequilla, N. 2012, A&A, 538

Pletsch, H. J., Guillemot, L., Allen, B., et al. 2012, ApJ, 744, 105

Poveda, A., Ruiz, J., & Allen, C. 1967, Boletin de los Observatorios Tonantzintla y Tacubaya, 4, 86

Röver, C., Messenger, C., & Prix, R. 2011, ArXiv e-prints

Sahakian, V., Aharonian, F., & Akhperjanian, A. 2006, Astroparticle Physics, 25, 233

Schulz, A., Ackermann, M., Buehler, R., Mayer, M., & Klepser, S. 2014, A&A, 565, A95

Stone, R. C. 1979, ApJ, 232, 520

Terada, Y., Tashiro, M. S., Bamba, A., et al. 2012, PASJ, 64, 138

Tetzlaff, N., Neuhäuser, R., & Hohle, M. M. 2011, MNRAS, 410, 190

Uchiyama, Y., Takahashi, T., & Aharonian, F. A. 2002, PASJ, 54, L73

van Buren, D. & McCray, R. 1988, ApJ, 329, L93

van Buren, D., Noriega-Crespo, A., & Dgani, R. 1995, AJ, 110, 2914

van Leeuwen, F. 2007, A&A, 474, 653

Weekes, T. C. 2008, in American Institute of Physics Conference Series, Vol. 1085, American Institute of Physics Conference Series, ed. F. A. Aharonian, W. Hofmann, & F. Rieger, 3–17

Weekes, T. C., Cawley, M. F., Fegan, D. J., et al. 1989, ApJ, 342, 379

Weekes, T. C. & Turver, K. E. 1977, in ESA Special Publication, Vol. 124, Recent Advances in Gamma-Ray Astronomy, ed. R. D. Wills & B. Battrick, 279–286

Wilks, S. S. 1938, Annals of Mathematical Statistics, 9, 60

Zwicky, F. 1957, Morphological astronomy

Acknowledgements / Danksagung